Thesis

The Impact of Aerosols on Space-Based Retrievals of Carbon Dioxide

Submitted by

Robert R. Nelson

Department of Atmospheric Science

In partial fulfillment of the requirements

For the Degree of Master of Science

Colorado State University

Fort Collins, Colorado

Spring 2015

Master's Committee:

Advisor: Christopher W. O'Dell

A. Scott Denning
Christian D. Kummerow
Michael A. Lefsky

Abstract

The Impact of Aerosols on Space-Based Retrievals of Carbon Dioxide

This work describes an investigation into the impact of aerosols on space-based retrievals of the column-averaged dry-air mole fraction of carbon dioxide (X_{CO_2}). It was initially hypothesized that a simplified non-scattering, or "clear sky", retrieval, which neglects scattering and absorption by clouds and aerosols, could potentially avoid errors and biases brought about by attempting to measure properties of clouds and aerosols when there are none present. Clear sky retrievals have the benefit of being orders of magnitude faster and potentially as accurate as "full physics" retrievals that attempt to gain information about clouds and aerosols. Real data from the Greenhouse Gases Observing Satellite (GOSAT) and simulated data from the Orbiting Carbon Observatory-2 (OCO-2) were analyzed to find conditions under which a clear sky retrieval might perform as well as a full physics retrieval.

It was found that for real GOSAT data the clear sky retrieval performed relatively well over land but not as well over ocean. The opposite conclusion was found for simulated OCO-2 data: it performed well over ocean but poorly over land. For both real GOSAT data and simulated OCO-2 data, high levels of filtering were needed for the clear sky retrieval to be able to perform nearly as well as or better than the full physics retrieval for both land and ocean surfaces. Spectral residuals were then examined to determine if the clear sky algorithm's performance was tied to errors in the spectral fitting. It was found that the clear sky retrievals had larger residuals than the full physics retrievals but that reducing the clear sky residuals by allowing them to fit for a customized residual pattern did little to reduce the X_{CO_2} errors. It was also shown that even very clear scenes may result in small but detectable clear sky residual patterns.

A comparison of cloud and aerosol properties measured by the X_{CO_2} retrieval algorithm to aerosol optical depths from the AErosol RObotic NETwork (AERONET) revealed that the algorithm is generally unable to accurately retrieve information about the amount of clouds and aerosols present. Using OCO-2 simulations, it was shown that the algorithm is also only somewhat able to retrieve the heights of the aerosol layers. Information retrieved about individual aerosol types was shown to be even less accurate.

Finally, early work in this study prompted investigation into how sensitive the X_{CO_2} retrieval algorithm is to the first guess of aerosol properties. χ^2 space was explored by varying the first guess of various aerosol parameters. It was revealed that the retrieved aerosol information and X_{CO_2} values can be highly sensitive to the first guess of the state vector, indicating significant nonlinearity in the retrieval's forward model.

Two main conclusions were derived from this work. The first is an analysis of real GOSAT clear sky X_{CO_2} retrievals and simulated OCO-2 clear sky X_{CO_2} retrievals which revealed that the clear sky algorithm is generally inferior to the full physics algorithm, except for when high levels of filtering are applied. The second conclusion is that the current aerosol parameterization leads to unacceptable levels of nonlinearity in the X_{CO_2} retrieval. These results motivate further study to improve the retrieval algorithm's aerosol parameterization, either directly or by including additional information, which may result in an improvement of the retrieval algorithm's ability to accurately measure X_{CO_2}.

Acknowledgements

I would initially like to thank Christopher W. O'Dell for his mentorship and guidance on this project. As his first student, the past two and a half years have been a learning experience for both of us but I feel we've now developed a productive, professional relationship, which I look forward to continuing in the future.

Thanks to Tommy Taylor along with other members of our research group for their support and fruitful discussions regarding this work. Thank you to Dave Flory of Iowa State University who believed in me and who encouraged me to reach my full potential. Thanks to my friends and family, who bring humor and sanity to my life. I am also thankful for my committee members, Scott Denning, Chris Kummerow, and Michael Lefsky, for their insights and helpful comments.

Finally, I would like to thank my mother, Rebecca Nelson, for being incredibly supportive and encouraging over all these years. There are no words to describe how much courage and dedication it took you to continue raising my sister and I. Thank you to my father, Charles Nelson, who, along with my mother, taught me to value knowledge and education early on in life.

Funding sources for this research include Susan Kulawik of the Bay Area Environmental Institute (BAER, Ames Research Center Cooperative for Research in Earth Science and Technology Cooperative Agreement #NNX12AD05A) as well as the Jet Propulsion Laboratory (NASA JPL OCO-2 Subcontract #1439002). I was also primarily supported by the American Meteorological Society (AMS) Graduate Fellowship Program for the first year of my master's studies. I am grateful to have the support of such extraordinary organizations and people.

Table of Contents

List of Tables

List of Figures

CHAPTER 1

Introduction

1.1. The Importance of Carbon Dioxide Measurements

Recently, space-based instruments such as the Greenhouse Gases Observing Satellite (GOSAT, Yokota et al. (2009)) and the Orbiting Carbon Observatory-2 (OCO-2, Crisp et al. (2004)) have been launched with the potential to provide global measurements of greenhouse gas concentrations, including carbon dioxide (CO_2). This global coverage should improve the accuracy of carbon flux models, which are heavily dependent on CO_2 measurements, and help to answer lingering questions about the Earth's sources and sinks of carbon and their interaction with the atmosphere (Rayner and O'Brien, 2001, Baker et al., 2010, Chevallier et al., 2007, 2009). It is know that only about half of the CO_2 emitted by humans stays in the atmosphere (Le Quéré et al., 2009). The rest is absorbed by the land and ocean, but little is known about how and where this absorption occurs, especially over land. These carbon flux models that had previously been limited by a sparse number of ground-based measurements of CO_2 will now have vastly more data at their disposal to improve the accuracy of their conclusions, but only if the space-based measurements are of high enough accuracy themselves. Specifically, it has been shown that an accuracy of better than about 0.5% ($\sim$2 ppm for CO_2) for space-based measurements is needed to gain more information about the carbon cycle compared to only having access to ground-based measurements (Miller et al., 2007). In terms of a bias between the measured CO_2 and how much CO_2 is actual present, even a few tenths of a ppm can be detrimental to carbon flux models (Chevallier et al., 2007, Basu et al., 2013). It is thus critically important to minimize errors in satellite measurements of CO_2 in order to be able to provide new answers to pertinent carbon cycle questions.

1.2. Retrieving Carbon Dioxide from Satellites

A popular way to measure, or "retrieve", CO_2 concentrations from space involves detecting sunlight reflected off the surface of the Earth with hyper-spectral resolution and determining how many CO_2 molecules are in the column of air seen, or the "light-path", by measuring how much sunlight is absorbed by the molecules. This method is conceptually shown in figure 1.1.

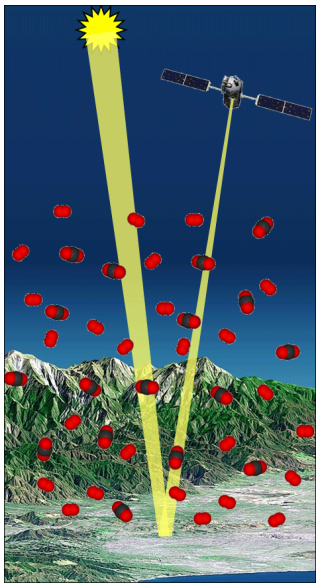

Figure 1.1. The light path is conceptually shown as the yellow beam emitting from the sun, getting reflected off the surface of the Earth, and being detected by the satellite.

Satellites such as GOSAT and OCO-2 make use of this method. Typically a relatively weak CO_2 absorption band located in the near-infrared around 1.6 μm and stronger CO_2 absorption band in the near-infrared at 2.0 μm are used in conjunction to deduce the average amount of CO_2 in the column of air seen by the instrument's sensors. The instrument on GOSAT containing these bands is the Thermal And Near infrared Sensor for carbon Observations-Fourier Transform Spectrometer (TANSO-FTS). The single value of CO_2 in

the column of air is specifically the column-averaged dry-air mole fraction of carbon dioxide, or X_{CO_2}:

$$X_{\mathrm{CO_2}} = \frac{\int_0^\infty N_{\mathrm{CO_2}}(z)dz}{\int_0^\infty N_{\mathrm{air}}(z)dz} \tag{1.1}$$

where $N_{CO_2}(z)$ is the molecular number density of CO_2 with respect to dry air at altitude z and $N_d(z)$ is the molecular number density of dry air at altitude z. Because the fraction of oxygen in air is well known (0.20935) and near uniform globally, equation 1.1 can be simplified to:

$$X_{\mathrm{CO_2}} = 0.20935\frac{\int_0^\infty N_{\mathrm{CO_2}}(z)dz}{\int_0^\infty N_{\mathrm{O_2}}(z)dz} \tag{1.2}$$

where the number density of O_2 and CO_2 can be estimated using measurements of reflected sunlight in the weak CO_2 band, strong CO_2 band, and O_2 A-band. An example of the measured spectra of all three near-infrared bands from GOSAT is shown in figure 1.2.

The properties of the three near-infrared bands for GOSAT and OCO-2 are given in table 1.1.

TABLE 1.1. Properties of the three near-infrared bands used by GOSAT and OCO-2 to retrieve X_{CO_2}.

Band	TANSO-FTS Spectral Range [cm^{-1}]	Channels	OCO-2 Spectral Range [cm^{-1}]	Channels
O_2 A	12900-13200	1203	12950-13190	1016
Strong CO_2	5800-6400	601	6166-6286	1016
Weak CO_2	4800-5200	436	4810-4897	1016

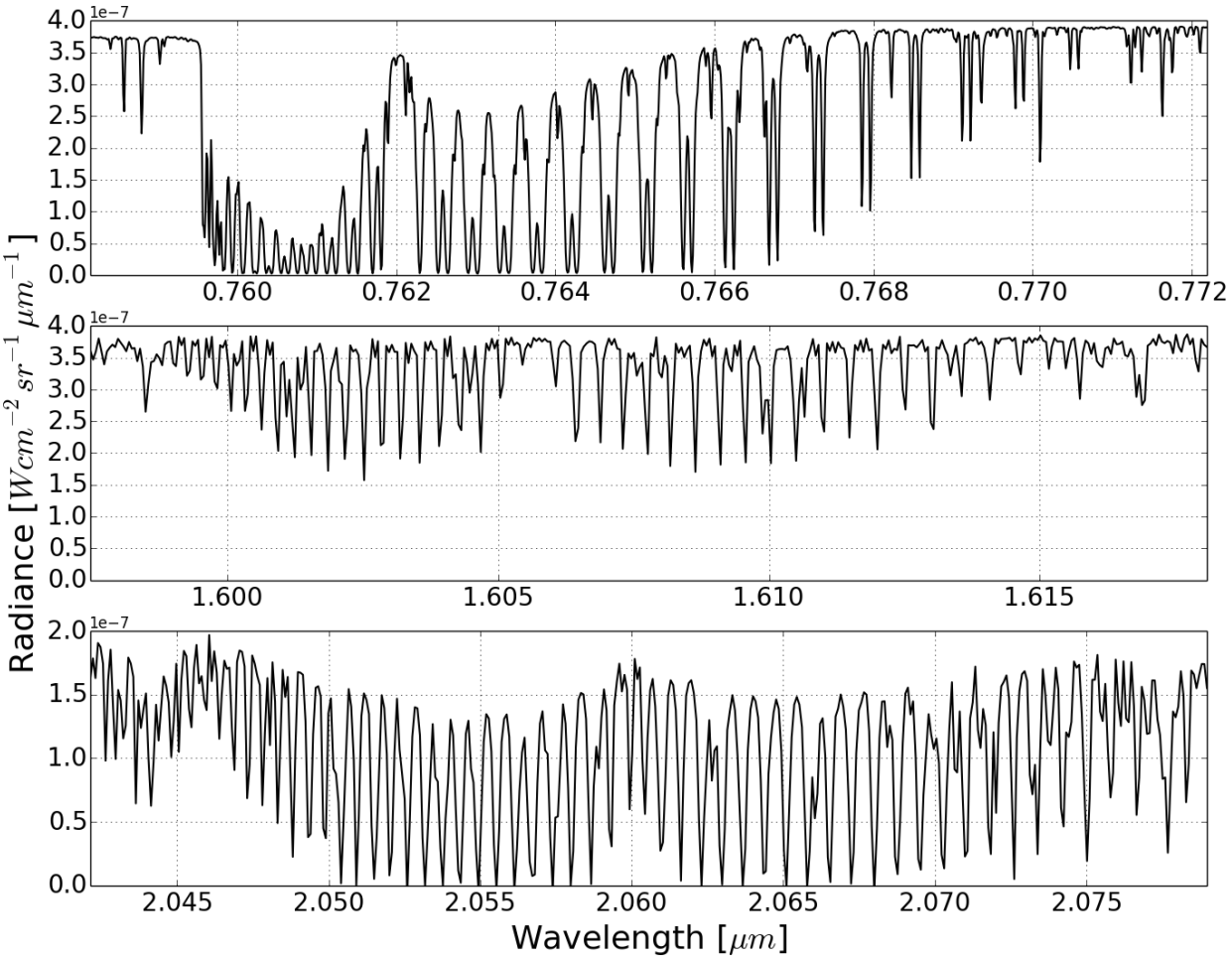

FIGURE 1.2. An example of measured radiances from GOSAT in the O_2 A-band (top), weak CO_2 band (middle), and strong CO_2 band (bottom).

Real data from GOSAT and simulated data from OCO-2 were used in this study. The X_{CO_2} retrieval algorithm used in this study, unless stated otherwise, was the NASA Atmospheric CO_2 Observations from Space (ACOS) algorithm (see O'Dell et al. (2012), Crisp et al. (2010) for details).

1.2.1. OPTIMAL ESTIMATION. The ACOS retrieval algorithm employs optimal estimation to try and accurately measure X_{CO_2} (Rodgers, 2000). Complete details of the algorithm can be found in the ACOS retrieval Algorithm Theoretical Basis Document (Crisp et al., 2010). Optimal estimation of X_{CO_2} uses a set of parameters, or a "state vector", to create

a modeled set of spectra, described in section 1.2, that match the spectra measured by the satellite, moderated by prior knowledge of the different state vector elements. This is done by using the state vector elements in the forward model, $\mathbf{F}$:

$$\mathbf{y} = \mathbf{F}(\mathbf{x}, \mathbf{b}) + \boldsymbol{\epsilon} \tag{1.3}$$

where $\mathbf{y}$ is a vector of the simulated radiance, $\mathbf{F}$ is the forward model, $\mathbf{x}$ is the state vector, $\mathbf{b}$ is a set of other fixed input parameters, and $\boldsymbol{\epsilon}$ is instrument and forward model errors.

The state vector elements are listed in table 1.2. The parameters selected for inclusion in the state vector are sensitive to the retrieved spectra and often represent physical quantities. Details on many of the elements can be found in O'Dell et al. (2012). Of note, a CO_2 profile of 20 layers is retrieved by the algorithm and then used to find the total X_{CO_2}. However, other retrieval algorithms use their own unique covariance matrices and CO_2 profile parameterizations.

The simulated radiances $\mathbf{y}$ are then used in an inverse model to try and minimize the χ^2 cost function given by:

$$\chi^2 = (\mathbf{F}(\mathbf{x}) - \mathbf{y})^T \mathbf{S}_{\boldsymbol{\epsilon}}^{-1} (\mathbf{F}(\mathbf{x}) - \mathbf{y}) + (\mathbf{x} - \mathbf{x_a})^T \mathbf{S}_{\mathbf{a}}^{-1} (\mathbf{x} - \mathbf{x_a}) \tag{1.4}$$

where $\mathbf{S}_{\boldsymbol{\epsilon}}$ is the observation error covariance matrix, $\mathbf{x_a}$ is the *a priori* state vector, and $\mathbf{S_a}$ is the *a priori* error covariance matrix. The *a priori* state vector and its corresponding error covariance matrix are derived from several sources including the European Centre for

TABLE 1.2. State vector elements of the ACOS X_{CO_2} retrieval algorithm, adapted from O'Dell et al. (2012).

Name	Quantities	*A Priori* Value	*A Priori* 1σ Error	Notes
CO_2	20[1]	Model Climatology	Fixed matrix	Mole Fraction wrt. dry air
Surface Pressure	1	ECMWF	1 hPa	
Temperature Offset	1	0 K	5 K	Offset to prior temperature profile
W.V. Scale Factor	1	1.0	0.5	Multiplier to prior specific humidity profile
Aerosol Amounts	4	Varies	Varies	ln(optical depth)[2]
Aerosol Heights[3]	4	Varies	Varies	
Albedo	3	From spectra[4]	1.0	Albedo at band center
Albedo Slope	3	0.0	0.0005 per cm^{-1}	
Wind Speed	1	7.0 m/s	3.3 m/s	Over-water only
Dispersion Offset	3	From spectra[4]	0.5 cm^{-1}	
Fluorescence[5]	1	0.0 $Wcm^{-2}sr^{-1}\tilde{\nu}^{-1}$	0.0004 $Wcm^{-2}sr^{-1}\tilde{\nu}^{-1}$	
Fluorescence Slope[5]	1	0.0018 $Wcm^{-2}sr^{-1}\tilde{\nu}^{-1}$	4.9×10^{-7} $Wcm^{-2}sr^{-1}\tilde{\nu}^{-1}$	
EOF Scale Factor	3	0.0	100.0	

[1] Profile quantities contain 20 or fewer elements, depending on the surface pressure.
[2] Optical Depth at 0.76 μm.
[3] Peak heights of the Gaussian distributions.
[4] Estimated directly from observed spectrum; see text for details.
[5] See Frankenberg et al. (2013).

Medium-Range Weather Forecasts (ECMWF) for the meteorological variables and zonally averaged seasonal cycles coupled with a typical atmospheric growth rate (for CO_2). The equation is solved for the value of $\mathbf{x}$ that minimizes χ^2. The new $\mathbf{x}$, found by the Levenberg-Marquardt algorithm in ACOS, is then re-run through the forward model and the result is used to try and again find the minimum χ^2. This iterative process is contented until certain thresholds are reached that indicate the algorithm has converged to a state vector containing optimal values that minimize the cost function.

1.3. Cloud and Aerosol Errors in X_{CO_2} Retrievals

One of the most significant issues that arises when measuring X_{CO_2} is the presence of clouds and aerosols. The main reason clouds and aerosols can ruin a retrieval is due to light-path modification. In order to precisely measure the light path, as described in section 1.2, the amount of molecules in the column must be established. If clouds and aerosols are present they can scatter the reflected sunlight in different directions which can drastically alter the length of the light-path seen by the sensor and result in significant errors when calculating X_{CO_2}. It has been shown that neglecting scattering and absorption by these aerosols and clouds can lead to significant errors in retrievals of X_{CO_2}. These errors often exceed 1% ($\sim$4 ppm) and can be tens of ppm for high optical depth scenes (O'Brien and Rayner, 2002, Aben et al., 2007, Butz et al., 2009).

1.4. Managing Cloud and Aerosol Errors

One method to avoid significant X_{CO_2} errors is to include a simple parameterization of clouds and aerosols in the X_{CO_2} retrieval algorithm. Most algorithms that have been developed contain some kind of method to gain information about clouds and aerosols (a brief description of some of these algorithms' aerosol schemes is given in section 1.4.1). This often includes adding one or more particle "types" to the algorithm along with parameters describing the particles. These variables are intended to represent typical clouds and aerosols found in the atmosphere. However, the addition of cloud and aerosol parameters to the algorithm can result in issues such as creating an under-constrained problem or inducing nonlinearity in the forward model. Worse yet, it has been shown that these "full physics" retrievals, which include cloud and aerosol parameterizations, may actually incur biases from trying to account for clouds and aerosols when none are present (O'Dell et al., 2012). For

ideal, very clear scenes this becomes an issue, because the addition of cloud and aerosol parameters may be doing more harm than good. Figure 1.3 shows a result from O'Dell et al. (2012) that demonstrates a bias in the full physics retrieval when applied to simulated scenes containing no clouds or aerosols.

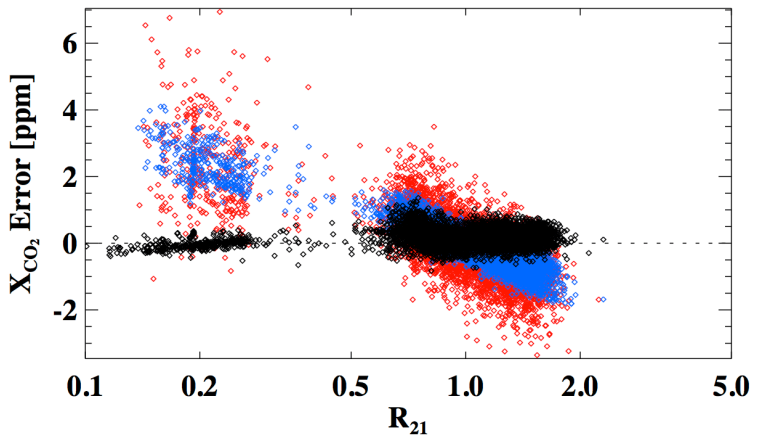

FIGURE 1.3. X_{CO_2} error in OCO simulations containing no clouds or aerosols compared to the ratio of the continuum signal level in the weak CO_2 band relative to the O_2 A-band (R_{21}). Black points are noiseless retrievals that contain no cloud or aerosol parameterization, blue points are noiseless full physics retrievals, and red points are full physics retrievals with noise added. Taken from O'Dell et al. (2012).

1.4.1. AEROSOL PARAMETERIZATION. There are many ways of parameterizing aerosols in X_{CO_2} retrieval algorithms. ACOS does so by including four unique aerosol types. The aerosols are assumed to have a Gaussian distribution in the vertical. The algorithm is allowed to fit for the height of the Gaussian as well as the magnitude. It has been shown that instruments like GOSAT and OCO-2 should be able to gain information about an aerosol layer's optical depth and height (Frankenberg et al., 2012). The width, however, is tightly constrained, as GOSAT and OCO-2 spectra are not very sensitive to the width of the aerosol layers. Other algorithms contain unique aerosol parameterizations. RemoTeC, the Karlsruhe Institute of Technology (KIT) X_{CO_2} retrieval algorithm, retrieves several properties of a single

generic mie type including the size distribution, height, scattering phase matrix, etc. (Butz et al., 2009). The Japanese National Institute for Environmental Studies (NIES) algorithm takes aerosols from a model and only retrieves the optical depths. The research group at the University of Leicester uses a retrieval similar to ACOS but one that only contains three types of aerosols.

Most of this study's analysis was done on ACOS build 3.4 and build 3.5 (see section 2.1 for details). The primary difference between these two versions is the aerosol parameterization. Both versions attempt to retrieve height and quantity information about four unique types of aerosols using an *a priori* peak height, width, and amount. Both versions fit for the same generic water cloud and ice cloud types. Besides those two types, ACOS B3.4 fits for two generic "Kahn" aerosol types (Kahn et al., 2001) while B3.5 uses a Modern-Era Retrospective Analysis for Research and Applications (MERRA) monthly climatology to choose the two most likely aerosol types for a given retrieval's location along with a corresponding climatological optical depth for use as the prior. The two most likely aerosol types for B3.5 can be any two of the five MERRA types: sulfate, dust, sea salt, organic carbon, and black carbon (Colarco et al., 2010). Select optical properties of the various aerosol types used in ACOS B3.4 and B3.5 are listed in table 1.3.

The Kahn 2b aerosol type is a mixture of coarse and fine-mode dust while the Kahn 3b aerosol type is a mixture of smaller carbonaceous aerosols. Both 2b and 3b also contain sulfate and sea salt components. For the MERRA types, dust and sea salt are the largest particle mixtures. Additional information on the MERRA aerosol types and their properties can be found in Chin et al. (2002).

The algorithm is allowed to change the profile's height and total integrated amount (optical depth) in order to minimize the cost function (see section 1.2.1). The *a priori*

TABLE 1.3. Optical properties of cloud and aerosol types in the ACOS B3.4 and B3.5 state vectors, adapted from O'Dell et al. (2012).

Aerosol Type	k_{ext} or Q_{ext}			Single Scattering Albedo		
	0.76 μm	1.61 μm	2.06 μm	0.76 μm	1.61 μm	2.06 μm
Kahn Type 2b[1]	0.934	0.842	0.580	0.933	0.980	0.972
Kahn Type 3b[1]	0.773	0.318	0.213	0.881	0.876	0.856
Sulfate	6715.2	964.5	422.8	1.000	0.997	0.961
Dust	719.6	715.6	702.6	0.924	0.940	0.935
Sea salt	1635.3	1619.7	1675.2	1.000	0.995	0.976
Organic carbon	3060.5	431.3	150.1	0.968	0.788	0.788
Black carbon	5922.8	2434.0	1871.6	0.145	0.037	0.019
Water cloud;[2] R_e=8 μm	2.131	2.224	2.268	1.000	0.991	0.950
Ice cloud;[3] R_e=70 μm	1.537	1.610	1.678	1.000	0.882	0.794

[1] Kahn et al. (2001)

[2] Gamma distribution (Hansen and Travis, 1974)

[3] Non-spherical particles according to Baum et al. (2005a,b)

Gaussian aerosol profiles for ACOS B3.4 and B3.5 are shown in figure 1.4. Due to current implementation constraints, the total amount is retrieved as the natural logarithm of the total optical depth at 0.76 μm for each type.

1.4.2. NON-SCATTERING X_{CO_2} RETRIEVALS. This study investigates the use of non-scattering "clear sky" retrievals that assume no aerosol or cloud effects and thus may avoid introducing unwanted biases. Clear sky retrievals do not include scattering and absorption by clouds and aerosols but they do include Rayleigh scattering by air molecules when necessary (of primary importance in the O_2 A-band). An analysis of retrieved aerosol optical depths compared to true aerosol optical depths (chapter 3) revealed that the aerosol information retrieved by various full physics algorithms was not very well correlated with the true aerosol information for a particular scene. This motivated me to investigate how the ACOS full physics retrieval's ability to estimate aerosols impacts its X_{CO_2} accuracy and to check if simply not trying to retrieve information about aerosols would lead to a comparably accurate

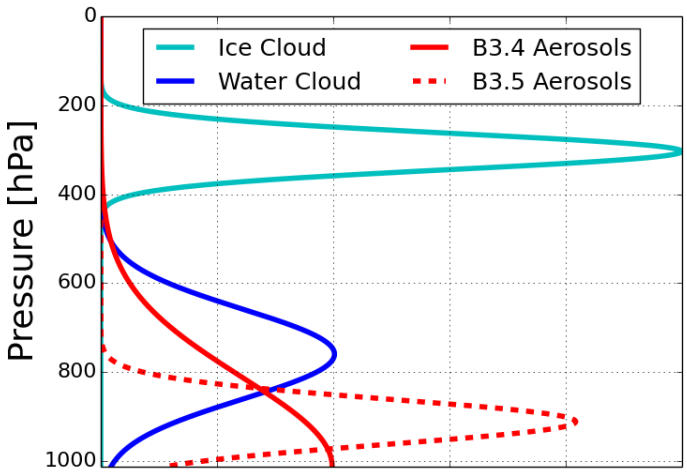

FIGURE 1.4. The *a priori* aerosol profiles for ACOS B3.4 and B3.5, assuming a surface pressure of 1013.0 hPa. The ice cloud is shown in cyan, the water cloud in blue, and the two Kahn aerosol types used in B3.4 in red. The ACOS B3.5 aerosol priors for both MERRA types is shown by the dashed red line (assuming a prior optical depth of 0.0125)

X_{CO_2} measurement for scenes uncontaminated by significant levels of clouds or aerosols. Previous work (Butz et al., 2013) has shown that a clear sky retrieval results in acceptable errors over ocean for very clear scenes. Clear sky retrievals are also desirable because of their high computational efficiency relative to full physics retrievals. This is because accurately calculating scattering from clouds and aerosols is computationally expensive: the current operational ACOS retrieval algorithm takes roughly 10 minutes per sounding while OCO-2 collects about 10^6 measurements per day. This greatly restricts the number of measurements able to be fully processed.

1.5. ORGANIZATION

A comparison of clear sky X_{CO_2} retrievals to full physics X_{CO_2} retrievals is given in chapter 2. The datasets and products used in the analysis are discussed. The genetic algorithm and bias corrections are then described and their effectiveness on reducing errors

is assessed. Clear sky X_{CO_2} retrievals are compared to full physics X_{CO_2} retrievals, both statistically and spatially for GOSAT and OCO-2 data. Clear sky spectral residuals are compared to full physics spectral residuals for GOSAT and OCO-2 data in order to see if a meaningful correlation exists between improvements in fitting the measured spectra and the retrieved X_{CO_2} errors. The creation of a custom clear sky mean residual pattern is performed, along with an investigation into how aerosols and clouds affect the magnitude of the residuals.

An analysis of how accurately aerosols are retrieved in GOSAT and OCO-2 measurements is described in chapter 3. GOSAT aerosol optical depths are compared to AErosol RObotic NETwork (AERONET) measurements and OCO-2 simulated aerosol optical depths are compared to the true scene values. A spatial analysis is done on both GOSAT and OCO-2 aerosol types. Finally, retrieved OCO-2 aerosol heights are compared to the true scene heights as well as the retrieved X_{CO_2} values.

X_{CO_2} retrieval nonlinearity due to clouds and aerosols is examined in chapter 4. Specifically, exploring how X_{CO_2} is affected by modifying the first guess of several aerosol parameters. Finally, χ^2 space is explored for a case where only two parameters were perturbed.

Chapter 5 summarizes the study's results, draws logical conclusions about the utility of clear sky X_{CO_2} retrievals, and proposes further analyses.

CHAPTER 2

Clear Sky X_{CO_2} Retrievals

This chapter tests the hypothesis that clear sky X_{CO_2} retrievals can perform as well as or better than full physics X_{CO_2} retrievals because they may not incur biases from trying to retrieve clouds and aerosols when there are none present. In the first section the GOSAT and OCO-2 datasets are described. Post-filtering via the genetic algorithm is examined followed by a discussion on the effectiveness of bias corrections. After applying the genetic algorithm and bias corrections to various datasets, a comparison of clear sky retrievals to full physics retrievals is done. Next, the two retrieval types are spatially compared to check for regions where clear sky retrievals may perform relatively better. Finally, residual patterns from both the clear sky and full physics retrievals are examined. The impact of fitting for a custom clear sky residual pattern on retrieved X_{CO_2} values is evaluated along with the impact of aerosols on the residual patterns.

2.1. X_{CO_2} Measurements and Simulations

2.1.1. Pre-filtering. The pre-filtering applied to most of the GOSAT and OCO-2 datasets consisted of removing measurements contaminated by high levels of clouds or aerosols using the O_2 A-band cloud screener (Taylor et al., 2012, O'Dell et al., 2012). The cloud screener works by comparing the surface pressure measured by the O_2 A-band to the surface pressure retrieved by the L2 algorithm. If the difference is on the order of several hPa, it is likely that there is a thick cloud or aerosol layer in the light path seen by the instrument. The algorithm was run on all measurements because it is extremely fast and not computationally expensive. Unfortunately, some measurements, especially those containing low clouds, are often not removed and thus impact the results of the study. In addition

to the O_2 A-band cloud screener, most of the GOSAT datasets were pre-filtered using the IMAP-DOAS preprocessor, which estimates X_{CO_2} independently from both the strong and weak CO_2 bands using a non-scattering algorithm (Frankenberg et al., 2005). The ratio of these measurements is then used, along with similar ratios of H_2O, to try and identify cloudy scenes. Similar parameters to those used in the IMAP-DOAS preprocessor were included in the genetic algorithm (see section 2.3), so the OCO-2 and unfiltered GOSAT datasets benefited from these filtering techniques as well. The combination of the O_2 A-band cloud screener and IMAP-DOAS results in an effective removal of many scenes contaminated by clouds and aerosols.

2.1.2. GOSAT Datasets. The GOSAT dataset contained retrievals on real GOSAT data from April 2009 to December 2012. The GOSAT dataset contains ocean and land scenes that attempt to represent the majority of surface types across the globe without being regionally biased. The unprocessed measurements, or "level 1B" data, contain radiances, pointing data, and geometric data. These level 1B data, along with meteorological data used as *a priori* information, were pre-filtered to remove low quality measurements. These low quality measurements are those that have an unacceptably low signal to noise ratio or contain easily detectable levels of clouds or aerosols. The remaining measurements are then run through the retrieval algorithm which outputs many fields, including X_{CO_2}, as "level 2" (L2) data. Retrievals that failed to converge to a solution were not used in this study. The retrieval algorithm used in this study was primarily the NASA ACOS algorithm. As the algorithm is currently in development, many different versions or "builds" were used in this study including builds 2.10, 3.4, 3.5, and 4.0. Basic details of each GOSAT dataset are given in table 2.1.

TABLE 2.1. Description of the various GOSAT X_{CO_2} datasets used in this study.

Name	# Retrievals	Pre-filtered?
ACOS B2.10	220,000	Yes
ACOS B3.4	25,000	Yes
ACOS B3.4 Unfiltered	25,000	No
ACOS B3.5	25,000	Yes
ACOS B4.0	74,000	Yes

The B2.10 data consists of retrievals run on real GOSAT data and spans from April 2009 to January 2011. This dataset was available early on in the project and primarily used for aerosol validation work (section 3.1). Two datasets exist for ACOS B3.4. A 25,000 retrieval pre-filtered GOSAT ACOS B3.4 dataset was used for much of this study's analysis. A corresponding unfiltered GOSAT ACOS B3.4 dataset was also used when testing the genetic algorithm filtering (section 2.3), containing approximately 25,000 retrievals. ACOS B3.5 was included in this study when it became available because it contains a different aerosol scheme than B3.4, which is first described in section 1.4.1. The GOSAT ACOS B3.5 dataset contained approximately the same 25,000 GOSAT retrievals as the pre-filtered GOSAT ACOS B3.4 dataset. ACOS B4.0 was used primarily because additional retrievals were desired and the algorithm had progressed to B4.0 by that point in the study. The GOSAT ACOS B4.0 dataset contains approximately 74,000 retrievals from June 2009 to December 2012. Only minor changes were made in the algorithm from B3.5 to B4.0.

2.1.3. OCO-2 DATASETS. The OCO-2 dataset contained 43,644 simulated OCO-2 retrievals (see O'Brien et al. (2009) for simulator details) from 58 orbits during 17-18 June 2012 and 19-20 December 2012. These 43,644 retrievals were selected for analysis because, of the total four days worth of measurements (156,128), they passed the O_2 A-band pre-filter described in section 2.1.1. This means approximately 30% of all measurements are kept to be run through the L2 code while 70% are discarded due to either contamination by clouds and

aerosols or a number of other obvious problems such as having an unusably low signal level. In reality, OCO-2 will make roughly 1,000,000 measurements per day. These simulations, however, were set up with a lower density of data.

Of the 43,644 measurements kept, roughly 25,000 to 40,000 make it through the L2 code and converge to a solution. This means that approximately 15-25% of the initial OCO-2 simulated measurements end up being used for this study. Operationally, computational limitations on running the L2 code will likely reduce that number further. Because not all measurements are able to be processed, it has been proposed that a genetic algorithm (described in section 2.3) be used to determine which measurements should be run through the L2 code.

Several different versions of the simulations were performed to account for noise, *a priori* meteorological knowledge, and scattering via clouds and aerosols. Details of each dataset used are given in table 2.2. All versions, unless stated otherwise, were run using the ACOS B3.4 retrieval algorithm.

TABLE 2.2. Description of the various OCO-2 X_{CO_2} datasets used in this study.

Name	Meteorology	Noise	Clouds and Aerosols
ACOS B3.4 02b	ECMWF	No	No
ACOS B3.4 02b NCEP	NCEP	No	No
ACOS B3.4 02c NCEP	NCEP	No	Yes
ACOS B3.4 02d	ECMWF	Yes	No
ACOS B3.4 02e NCEP	NCEP	Yes	Yes

OCO-2 "02b" simulations are noiseless and cloud- and aerosol-free. "02c" simulations are noiseless but contain clouds and aerosols. "02d" simulations are cloud and aerosol-free but contain synthetic instrument noise. The noise added was Gaussian and consistent with the measured instrument noise (O'Dell, 2010). Finally, "02e" simulations contain clouds and aerosols as well as noise. All versions of the simulations can either use perfect or imperfect

meteorology. Perfect meteorology means the *a priori* meteorology information is identical to the "true" meteorological conditions used in the simulation. Imperfect meteorology means a different dataset was used to obtain the *a priori* meteorology information. In this analysis, National Centers for Environmental Prediction (NCEP) reanalysis data was used which is typically slightly different than the "true" meteorological conditions used to set up the simulation. The idea behind using imperfect meteorology is that real retrievals will also likely have slightly erroneous *a priori* meteorological information compared to the true scene conditions. This analysis focused primarily on 02e NCEP OCO-2 simulations, which are the most realistic of those previously described: noisy, containing clouds and aerosols, and using imperfect *a priori* meteorological knowledge derived from the NCEP reanalysis.

The vertical profiles of clouds and aerosols used in the OCO-2 simulations were derived from Cloud-Aerosol Lidar with Orthogonal Polarization (CALIOP) data. CALIOP is a lidar onboard Cloud-Aerosol Lidar and Infrared Pathfinder Satellite Observations (CALIPSO), a joint NASA and Centre National d'Etudes Spatiales (CNES) satellite. It was launched in April of 2006 and flies in roughly the same orbit as OCO-2 and several other environmental satellites. The aerosol and cloud data ingested into the OCO-2 simulations is separated into 128 vertical levels containing an ice cloud type, water cloud type, and six aerosol types (O'Brien et al., 2009).

2.1.4. Retrieval Types. Full physics and clear sky X_{CO_2} retrievals were performed on both datasets over land and ocean surfaces. Clear sky retrievals ignore all scattering and absorption by cloud and aerosol and only include Rayleigh scattering by air molecules. The clear sky retrievals only utilize the CO_2 short-wave bands at 1.6 and 2.0 μm while the full physics retrievals also utilize the O_2 A-band at 0.76 μm. Because Rayleigh scattering is primarily important in the O_2 A-band, which the clear sky retrieval doesn't use, a different

version of the clear sky retrieval could theoretically be run that doesn't calculate Rayleigh scattering in any of the bands. The full physics algorithm uses additional information from the O_2 A-band because small cloud and aerosol particles typically have a larger impact on shorter wavelengths and thus it tries to account for these effects by fitting for the aerosol parameters in the state vector.

Both retrieval types use the O_2 A-band for pre-filtering out scenes contaminated by significant amounts of clouds and aerosols (described in section 2.1.1). The generated X_{CO_2} values were then compared to "true" X_{CO_2} measurements (described in section 2.2) in order to gauge the retrievals' performances. The retrieved OCO-2 X_{CO_2} used in comparisons was the averaging kernel-corrected X_{CO_2}. That is, a value of X_{CO_2} that is a weighted mix of the retrieved X_{CO_2} and the *a priori* X_{CO_2} which represents what the instrument would actually measure (Connor et al., 2008):

$$u_{ak} = Au_{true} + (I - A)u_a \tag{2.1}$$

where u_{ak} is the CO_2 adjusted by the averaging kernel, A is the averaging kernel matrix, u_{true} is the measured CO_2 profile, I is the identity matrix, and u_a is the *a priori* CO_2 profile. The averaging kernel matrix represents the relationship between the values measured by the instrument and the true values. In a perfect retrieval the averaging kernel matrix would be equivalent to the identity matrix. That is, each value of the CO_2 profile would only be sensitive to the atmospheric conditions at that exact level. In real retrievals, however, the averaging kernel matrix describes how the retrieved information is smoothed out. For the CO_2 profile, each row of the averaging kernel matrix is a function that peaks at the corresponding pressure level. The width of the function describes the spatial resolution of

the observing system (Rodgers, 2000). The averaging kernel can also be thought of as a description of the vertical resolution of the measurements.

Post-filtering was accomplished via a genetic algorithm, described in section 2.3. This step is necessary because the problem of retrieving CO_2 is under-constrained (Connor et al., 2008). That is, there can potentially be multiple valid solutions of the forward model for a single set of measurements. Besides being under-constrained, there may be nonlinearity in the forward model that causes the retrieval to fail in finding the true χ^2 minima but rather to settle in a local minima or broad valley of low χ^2 values that does not represent the optimal estimate of the state vector. Thus, simple threshold filters can be applied post-retrieval to try and remove these spurious retrievals. The most common variables selected by the genetic algorithm for filtering simulated OCO-2 data were examined in order to evaluate the possibility of their use in pre-filtering data.

2.2. Model Validation

In order to evaluate the accuracy of the X_{CO_2} retrievals, a "true" X_{CO_2} was needed. For GOSAT data the true X_{CO_2} was either a co-located Total Carbon Column Observing Network (TCCON) (Wunch et al., 2011a) measurement or a consensus of model-estimated X_{CO_2}. TCCON is a network of ground-based Fourier transform spectrometers with a accuracy and precision of better than 0.25% for X_{CO_2}. The model-estimated X_{CO_2} was an average of seven CO_2 models which were required to all agree to within 1.0 ppm of X_{CO_2} in order to be used for comparison. These models include two from the University of Edinborough, one from Le Laboratoire des Sciences du Climat et de l'Environnement, two from NIES, one CarbonTracker model, and one from David Baker of NOAA. Obviously these methods have accuracy limitations but they are needed in order to robustly evaluate X_{CO_2} retrievals over a

variety of surface types. Both the scatter and bias of the datasets are evaluated to determine the retrievals' performance.

2.3. Genetic Algorithm

A genetic algorithm, described by Mandrake et al. (2013), was used to find the optimal post-filters for both real GOSAT data and simulated OCO-2 data. Genetic algorithms are optimization tools that mimic natural selection to explore high dimensional parameter spaces (Periaux and Galan, 1995). In this case, the genetic algorithm tried to find filtering variables that minimized the standard deviation of error in X_{CO_2} for any given level of throughput. Throughput represents the amount of data kept: a throughput of 30% indicates that 70% of the data was filtered out. The standard deviation of the error was chosen to be minimized because it is a simple parameter that effectively represents how consistently the retrieval is able to perform. The genetic algorithm also allows for more than one "rule" to be used. That is, one rule selects the single most effective variable in reducing error for a given throughput while two rules selects the best combination of two rules in reducing error. For this study five rules were typically used to ensure optimal filtering of the data. However, in many situations fewer rules are necessary to maximize the reduction in error (see Mandrake et al. (2013)). The "most effective" filter is that which appears most frequently and contributes the most to reducing the standard deviation of the X_{CO_2} error. The variables chosen by the genetic algorithm were carefully selected to not "cheat" and give the algorithm more information than it should have. E.g. the true X_{CO_2} was not allowed to be chosen as a filtering parameter.

The genetic algorithm was run multiple times for different versions of the retrieval algorithm and both surface types (land and ocean), since it was hypothesized that they might

yield different optimal filtering parameters. Common optimal filters were found which and then used to select sets of retrievals that had low X_{CO_2} errors.

As previously mentioned, the genetic algorithm finds optimal solutions for as many rules as desired. That is, if only a single filtering variable is of interest, the algorithm will seek out the single most effective filtering parameter at each throughput level. If one wants the best combination of five filters, the algorithm will search for the best combination of five parameters to reduce the standard deviation of the error. Typically, only 2-5 rules are needed to effectively minimize the error at most throughput levels. This is shown in figure 2.1: after 3 rules there is only a minimal reduction in the error. The benefit of adding additional filtering rules is thus negligible. While figure 2.1 shows an example for OCO-2 simulations over land, even fewer rules are typically necessary for filter optimization over ocean surfaces.

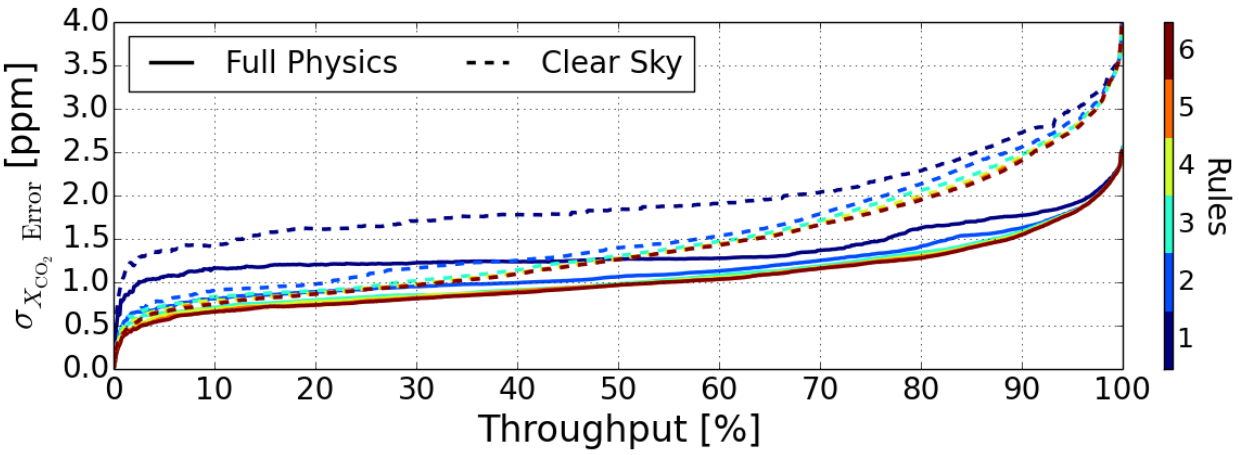

FIGURE 2.1. Genetic algorithm filtering rules applied to OCO-2 ACOS B3.4 simulations over land for full physics (solid) and clear sky (dashed) retrievals. The y-axis is the standard deviation of the difference between the retrieved X_{CO_2} and the true X_{CO_2}. The throughput represents the percentage of data that remains after applying the filter.

Table 2.3 shows the most common one, two, and three rule parameters selected by the genetic algorithm for full physics retrievals over ocean. The numerical value represents the percentage of the retrievals filtered out at all throughput levels for a given number of

rules. For one and two rules, the CO_2 ratio is typically selected as the most important filter. The CO_2 ratio is the amount of signal received in the weak CO_2 band divided by the signal received in the strong CO_2 band. As the number of rules increases, the combination of parameters becomes more complex and other variables contribute more to the filtering. This is seen in the "3 Rules" column, where the CO_2 ratio explains a small majority of the filtering while dP_{ABO_2} (the difference between the O_2 A-band retrieved pressure and L2 retrieved pressure) explains over 45%.

TABLE 2.3. Most frequently selected parameters for one, two, and three genetic algorithm rules and the percentage of all retrievals that they filter out (%) for full physics OCO-2 ACOS B3.4 simulations over ocean.

1 Rule	%	2 Rules	%	3 Rules	%
CO_2 Ratio	78.5%	CO_2 Ratio	87.9%	CO_2 Ratio	66.9%
Strong CO_2 RMS	9.5%	dP_{ABO_2}	28.4%	dP_{ABO_2}	45.2%
Strong CO_2 SNR	7.8%	Solar Zenith Angle	15.7%	ΔT	13.0%
Weak CO_2 Noise	3.0%	H_2O Ratio	5.2%	Strong CO_2 Noise	11.9%

The most effective rules for full physics retrievals over land as well as clear sky retrievals over ocean and land were also examined (not shown). The CO_2 ratio is typically employed as the first or second most important rule for all cases. This implies it could be used to further pre-filter data because its value is known before running the data through the L2 code. This may be especially useful for OCO-2 because computational power will be limited and care must be taken in selecting which L1B measurements to fully analyze.

The genetic algorithm was also run on the unfiltered GOSAT dataset. Over ocean, it was found that the root mean square (RMS) error of the strong CO_2 band was by far the most frequently selected filter. Over land, dP_{ABO_2} (defined above) was chosen most frequently along with the signal of the strong CO_2 band.

In this section I have demonstrated the effectiveness of the genetic algorithm at removing additional contaminated scenes not removed by pre-filtering. For all genetic algorithm results examined in this study, the final standard deviation of the X_{CO_2} error is the minimum value the algorithm could find with a given number of rules and is always lower than or roughly equal to the value found by manually filtering the data (not shown). This indicates that the genetic algorithm is effective at finding the best possible way to filter the data for a desired throughput level.

2.4. Bias Correction

Because the ACOS retrieval algorithm doesn't perfectly represent real-world physics and may not include all sources of instrument noise, biases can occur between the retrieved X_{CO_2} and other measured or retrieved parameters. X_{CO_2} biases can also be caused by deficiencies in the implementation of the spectroscopic line shape of the O_2 A-band and the strong CO_2 bands (Wunch et al., 2011b). A bias correction can be useful in dramatically reducing the overall X_{CO_2} errors. A single variable was selected for bias correction for the GOSAT dataset, unique to the retrieval type and surface type. The parameter chosen was determined by how well it was correlated with the error between the retrieved X_{CO_2} and "true" X_{CO_2} (section 2.2). A linear fit was made with the independent variable being the selected parameter and the dependent variable being the error in X_{CO_2}. The deviation of each X_{CO_2} error from this line was then subtracted from the retrieved X_{CO_2}. Bias corrections for OCO-2 simulations were briefly examined, but were found to be less effective compared to real GOSAT retrievals. This is likely because OCO-2 simulations do not contain real-world noise and other factors such as spectroscopy errors that can contribute to unwanted biases.

The bias corrections chosen for the pre-filtered GOSAT ACOS B3.4 dataset are listed in table 2.4. They were selected by examining the correlation coefficients of many variables compared to the error in X_{CO_2}. The most highly correlated variable was selected in order to maximize the reduction in the standard deviation of the X_{CO_2} error. Multivariate bias corrections were also explored but were found to only minimally further reduce the X_{CO_2} error.

TABLE 2.4. Bias correction parameter chosen to minimize the standard deviation of the X_{CO_2} error for GOSAT ACOS B3.4 data. The correlation coefficient (R), standard deviation before bias correction (σ), and standard deviation after bias correction (σ_{bc}) are also listed for each retrieval type.

Retrieval Type	Surface	Bias Correction Parameter	R	σ	σ_{bc}
Full Physics	Ocean	Band 3/2 Signal Ratio	0.290	1.36	1.30
Clear Sky	Ocean	dP_{ABO_2}	0.413	1.88	1.71
Full Physics	Land	Weak CO_2 Albedo	0.293	1.99	1.90
Clear Sky	Land	dP_{ABO_2}	0.392	2.13	1.96

Figure 2.2 shows the variables with the highest correlation with the X_{CO_2} error for full physics ocean retrievals (left) and clear sky ocean retrievals (right). The correlation between the strong CO_2 band to weak CO_2 band signal ratio and the X_{CO_2} error for full physics ocean retrievals was 0.29, which indicates the bias correction would reduce the variance of the dataset by 8.4%. The clear sky X_{CO_2} errors correlated highly with dP_{ABO_2}, which is the difference in the O_2 A-band pressure and the L2 pressure. For the same ocean retrievals run in clear sky mode, a bias correction on dP_{ABO_2} reduces the variance by approximately 17%.

Similar correlations were found over land. Figure 2.3 shows the correlation between the weak CO_2 albedo and X_{CO_2} error for full physics retrievals over land (left). For the full physics land retrievals analyzed, the trend in weak CO_2 albedo was able to explain approximately 8.6% of the variance in X_{CO_2} error and was thus chosen as a bias correction parameter. For clear sky retrievals over land, the correlation between dP_{ABO_2} and X_{CO_2} error was able to

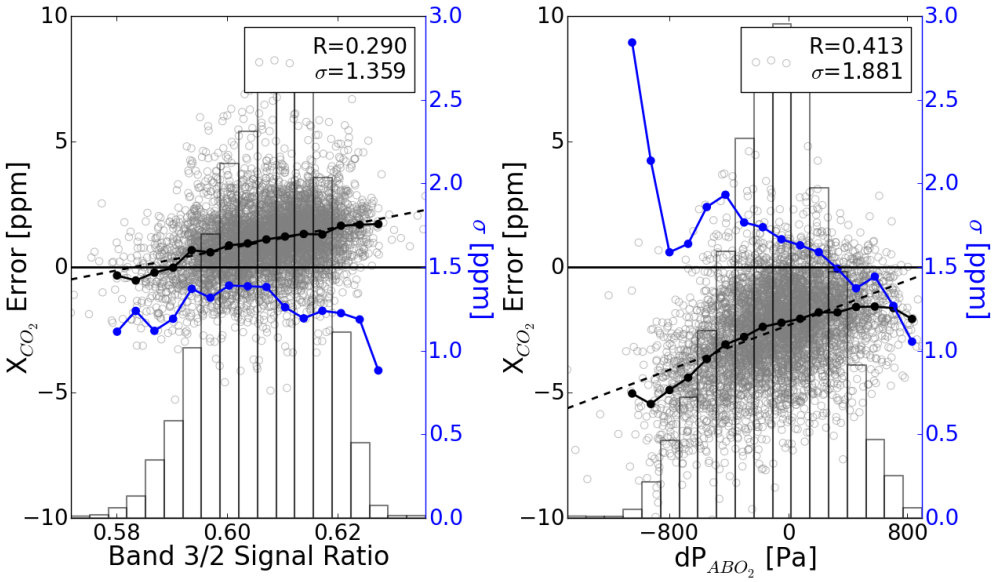

FIGURE 2.2. The left panel shows the GOSAT ACOS B3.4 full physics ocean X_{CO_2} errors compared to the strong CO_2 signal to weak CO_2 signal ratio. The right panel shows the GOSAT ACOS B3.4 clear sky ocean X_{CO_2} errors vs. the difference in the O_2 A-band pressure and the L2 pressure. The grey circles are the retrieved values, the black dotted line is a binned average of the retrieved values, and the dashed black line is a linear fit to the data points. The blue, dotted line is a binned average of the standard deviation of the X_{CO_2} errors. The vertical histogram bars represent the relative amount of data in each bin.

explain approximately 15.4% of the variance in X_{CO_2} error and was thus chosen as a bias correction parameter. Of note, dP_{ABO_2} was the most correlated parameter for both ocean and land clear sky retrievals. Over both surfaces, negative values of dP_{ABO_2} are associated with negative X_{CO_2} biases while positive values of dP_{ABO_2} are associated with positive X_{CO_2} biases. This is because lower P_{ABO_2} values due to clouds and aerosols above the surface result from a shorter light path, which also causes an underestimation of X_{CO_2}. The opposite is also true: erroneously long light paths, caused by complex scattering between the surface and clouds or aerosols, result in a larger P_{ABO_2} and larger X_{CO_2}. This clear and persistent bias supports the argument that even a small amount of clouds or aerosols can dramatically change the retrieved X_{CO_2} value.

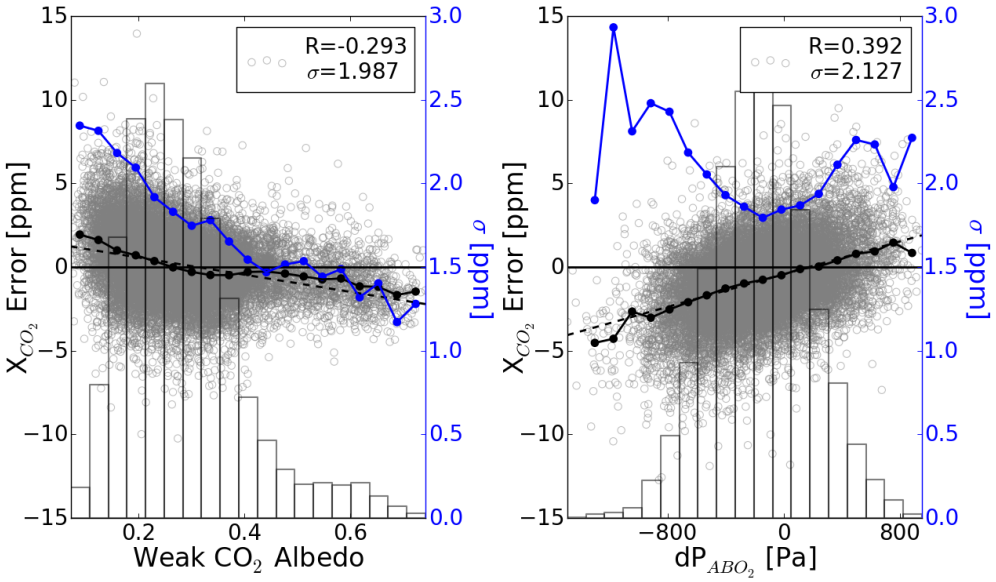

FIGURE 2.3. The left panel shows the GOSAT ACOS B3.4 full physics land X_{CO_2} errors vs. the weak CO_2 albedo. The right panel shows the GOSAT ACOS B3.4 clear sky ocean X_{CO_2} errors vs. the difference in the O_2 A-band pressure and the L2 pressure. The grey circles are the retrieved values, the black dotted line is a binned average of the retrieved values, and the dashed black line is a linear fit to the data points. The blue, dotted line is a binned average of the standard deviation of the X_{CO_2} errors. The vertical histogram bars represent the relative amount of data in each bin.

2.5. X_{CO_2} Retrieval Comparison

In the previous two sections I have established the effectiveness of post-filtering via the genetic algorithm and bias corrections in creating a robust dataset that contains only high quality X_{CO_2} retrievals. I now apply those methods to the GOSAT and OCO-2 datasets and calculate overall statistics in an attempt to fairly compare clear sky and full physics retrievals. This included looking at the standard deviation of the error X_{CO_2}, the root mean square (RMS) error, and the reduced χ^2. Various levels of post-filtering and bias corrections were explored along with separate analyses for land and ocean retrievals. Regional biases were examined for GOSAT data by binning retrievals in Atmospheric Tracer Transport Model Intercomparison Project (TransCom) regions and calculating statistics for each region.

2.5.1. Summary of GOSAT Error Statistics. The effectiveness of the genetic algorithm on unfiltered GOSAT data is shown in figure 2.4. One bias correction was applied to the dataset prior to using the genetic algorithm. Here it can be seen that over ocean surfaces the clear sky retrieval algorithm performs worse than the full physics retrieval algorithm, even at very high filtering levels. Over land, however, the clear sky retrievals become comparable to the full physics retrievals when significantly filtered (throughput of ∼10%).

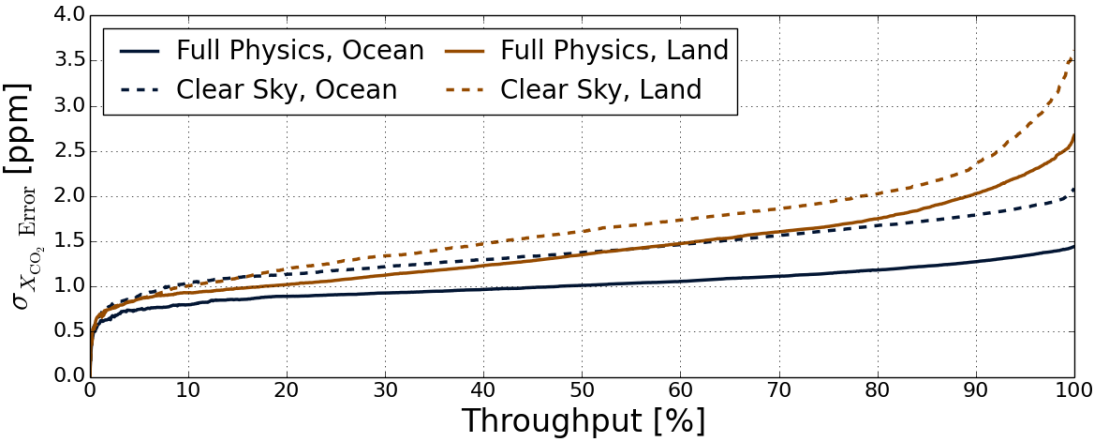

Figure 2.4. Genetic algorithm filtering applied to GOSAT ACOS B3.4 retrievals for land (brown) and ocean (blue) surfaces for both clear sky (dashed) and full physics (solid) retrievals. Four genetic algorithm rules were used. The y-axis is the standard deviation of the difference between the retrieved X_{CO_2} and the true X_{CO_2}. The throughput represents the percentage of data that remains after applying the filter.

Table 2.5 shows the standard deviation of the error in X_{CO_2} for all ocean retrievals (inferred from figure 2.4). With a difference in the standard deviation of X_{CO_2} error generally on the order of ∼0.3-0.5 ppm, this comparison suggests that the clear sky retrieval, when applied to real GOSAT data, is generally inferior to a full physical retrieval over ocean surfaces, regardless of filtering level. This is in contrast to Butz et al. (2013), who hypothesized that clear sky retrievals showed promise over ocean. However, Butz et al. 2013 used a different

technique to identify suitable retrievals and didn't include contamination by low cloud or aerosols in their simulations.

TABLE 2.5. Standard deviation (σ) of the X_{CO_2} error at different throughput levels using four rules for GOSAT ACOS B3.4 retrievals over ocean. One bias correction was applied to each dataset.

	No Filtering	70%	50%	30%	10%	5%
σ (Full Physics) [ppm]	1.46	1.11	1.01	0.93	0.80	0.75
σ (Clear Sky) [ppm]	2.09	1.56	1.38	1.22	1.04	0.90

Table 2.6 shows the same information but for retrievals over land. Both error standard deviations are larger, but the difference in errors now ranges from ∼0.3-0.0, depending on the level of filtering. This provides evidence that GOSAT clear sky retrievals performs more comparably to full physics over land than ocean and that the difference in error can be almost negligible at high filtering levels.

TABLE 2.6. Standard deviation (σ) of the X_{CO_2} error at different throughput levels using four rules for GOSAT ACOS B3.4 retrievals over land. One bias correction was applied to each dataset.

	No Filtering	70%	50%	30%	10%	5%
σ (Full Physics) [ppm]	2.67	1.60	1.35	1.12	0.93	0.86
σ (Clear Sky) [ppm]	3.62	1.86	1.61	1.34	1.00	0.86

In addition to statistics of the whole datasets, spatial errors in the real GOSAT retrievals are examined to see if there was regional variability or regions where the clear sky algorithm performed relatively better. Figures 2.5 and 2.6 show the RMS of the X_{CO_2} error for the GOSAT ACOS B3.4 full physics and clear sky pre-filtered datasets, respectively. These errors were averaged for each of the TransCom regions. One bias correction for each combination of surface type (ocean, land) and retrieval type (full physics, clear sky) was applied (see section 2.4). All of the ocean regions perform noticeably worse for the clear sky retrievals, which is in agreement with table 2.5. The picture for real GOSAT data over land, however,

is less clear. Certain regions do worse while others do better, leading to overall relatively good agreement with the total global errors in the full physics dataset (table 2.6).

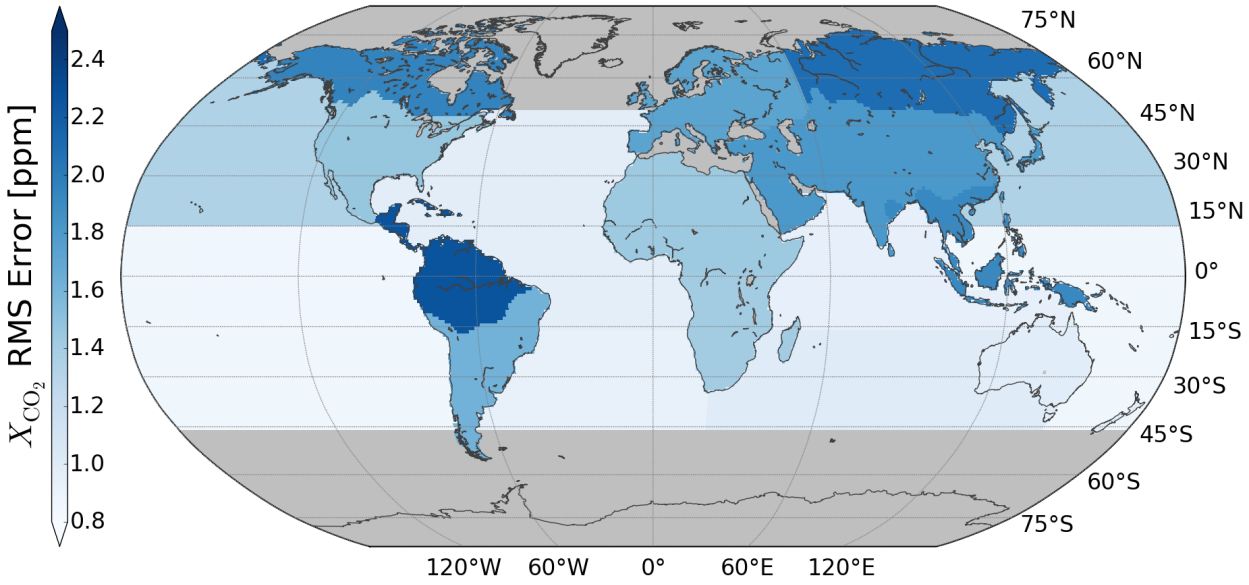

FIGURE 2.5. RMS of the GOSAT ACOS B3.4 full physics X_{CO_2} error for the TransCom regions. Regions containing no data are shown in grey.

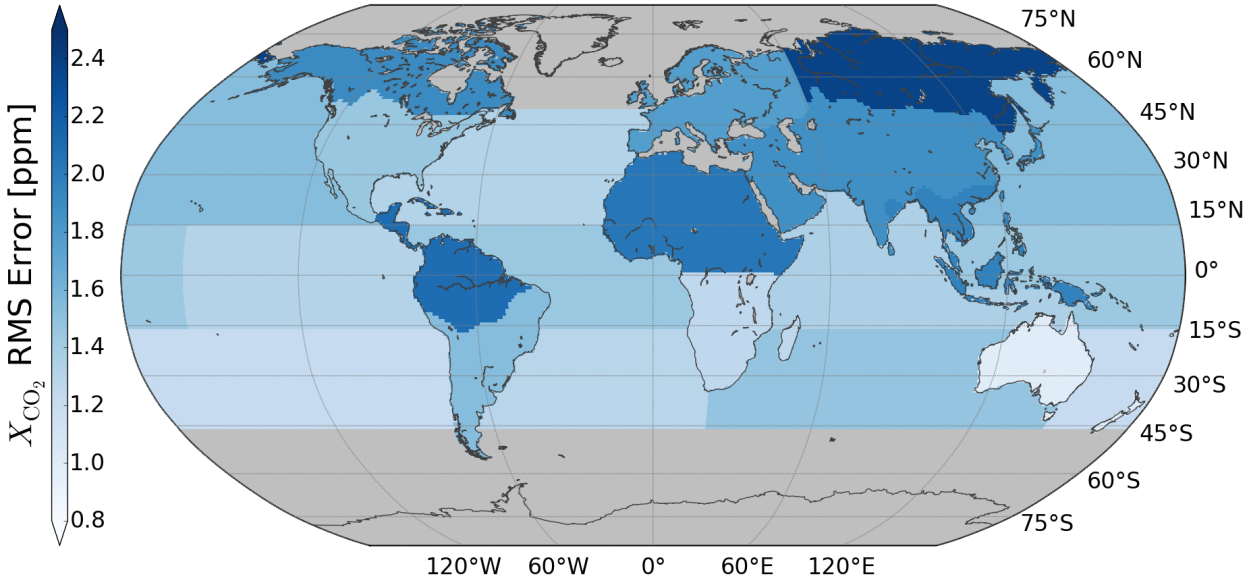

FIGURE 2.6. RMS of the GOSAT ACOS B3.4 clear sky X_{CO_2} error for the TransCom regions. Regions containing no data are shown in grey.

The RMS of the X_{CO_2} error includes both the scatter and bias in the data. Here the bias itself is examined in more detail. Without applying any corrections, the full physics dataset has an overall high bias of roughly 1.0 ppm over ocean and 0.1 ppm over land while the clear sky dataset has a bias of -2.5 ppm over ocean -0.8 ppm over land. This means that, for example, the clear sky retrieval on average retrieves a value of X_{CO_2} 2.5 ppm lower than the true X_{CO_2} amount. These are just the biases for this specific dataset; in general biases can be highly dependent on the retrieval setup. To remove the overall X_{CO_2} bias, a single unique correction was applied to each surface type for both retrieval types (as described in section 2.4). This reduces the overall bias in X_{CO_2} to roughly zero, but obviously regional biases may still exist. The data may also be biased against certain parameters, but spatial biases are the most worrisome because of the potential impact they have on flux inversion models. The bias component of the full physics and clear sky retrievals averaged over the TransCom regions are shown in figures 2.7 and 2.8, respectively. Here the bias is defined as the retrieved X_{CO_2} minus the true X_{CO_2}.

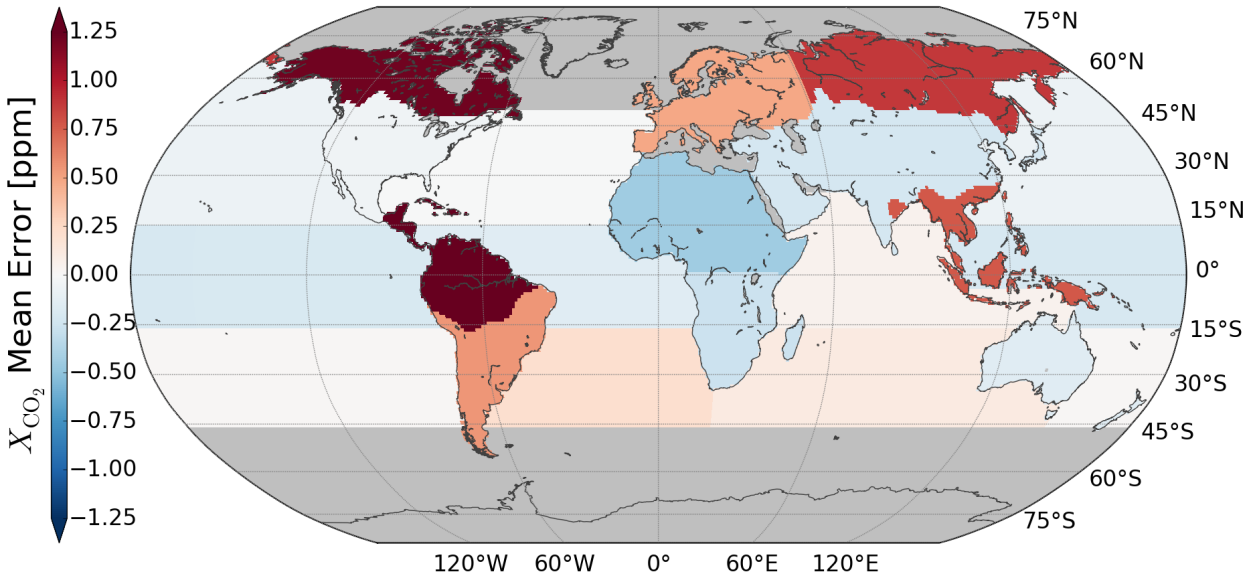

FIGURE 2.7. Bias of the GOSAT ACOS B3.4 full physics X_{CO_2} error for the TransCom regions. Regions containing no data are shown in grey.

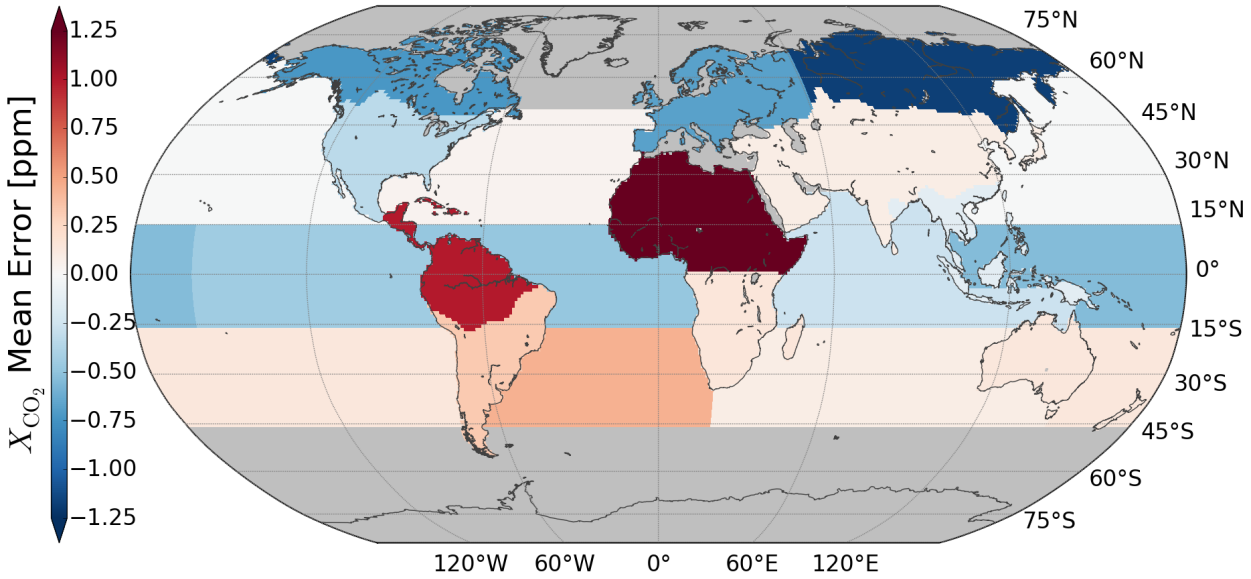

FIGURE 2.8. Bias of the GOSAT ACOS B3.4 clear sky X_{CO_2} error for the TransCom regions. Regions containing no data are shown in grey.

Over land the regional biases are highly variable for both the full physics dataset and the clear sky dataset. For example, a ∼1.0 ppm bias exists over northern Africa for the clear sky dataset while that same region has a roughly -0.5 bias for full physics. Over ocean the sign of the bias is often the same for a given region but the magnitude appears to be larger for the clear sky dataset. In general, the clear sky dataset does not have lower biases than the full physics dataset. This contradicts the hypothesis that the clear sky retrieval would have lower biases because it may avoid biases caused by clouds and aerosols for very clear scenes. It is likely that the complexity of the retrieval algorithm as well as the choice of how to apply the bias corrections themselves leads to the hypothesis being false. These results demonstrate that additional work is needed to maximize the reduction in regional biases.

The difference in the mean X_{CO_2} error is shown in figure 2.9. The values correspond to the absolute value of the full physics X_{CO_2} error minus the absolute value of the clear sky X_{CO_2} error. Thus, negative values indicate that the clear sky retrievals performed worse while red values indicated that they performed better. It's clear that over ocean full physics

GOSAT retrievals are superior to clear sky retrievals. This is in agreement with the RMS TransCom analysis. Clear sky retrievals are able to perform better over South America and southern Africa, but differences over the other land regions are small. The exception is Northern Africa, where it appears that full physics retrievals perform much better than clear sky retrievals. The good performance of clear sky retrievals over northern South America could be due to low number statistics, as only 69 retrievals were valid in that region for this dataset.

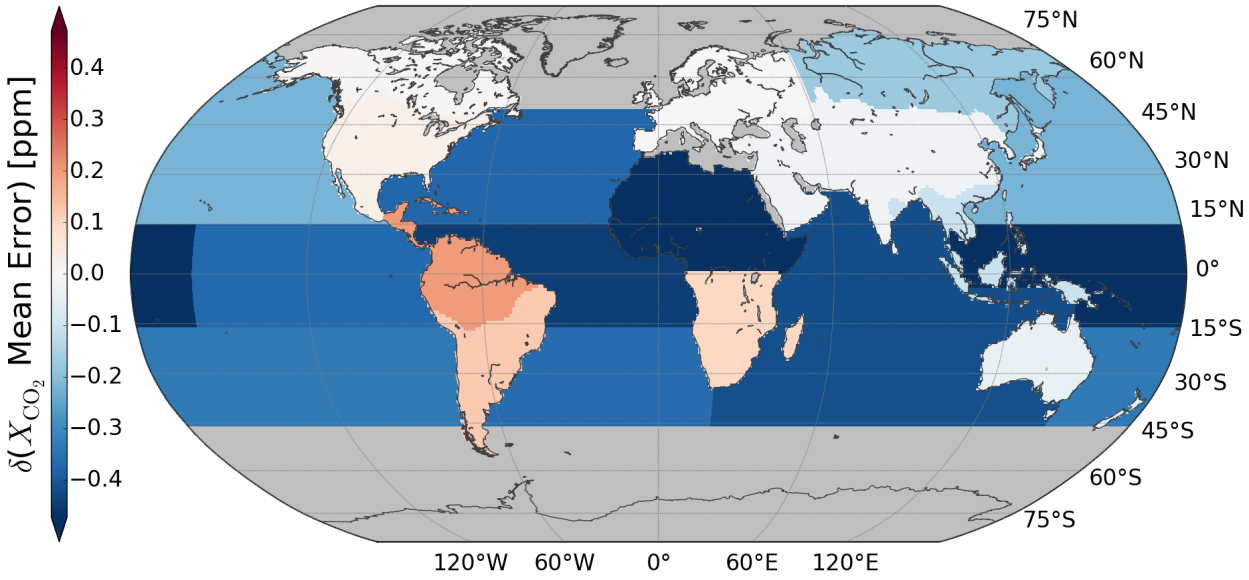

FIGURE 2.9. The difference in the magnitude of the mean X_{CO_2} errors between GOSAT ACOS B3.4 full physics retrievals and GOSAT ACOS B3.4 clear sky retrievals for the TransCom regions. Negative values (blue) indicate full physics performs better while positive values (red) indicate clear sky performs better. Regions containing no data are shown in grey.

In this section I have demonstrated that real GOSAT clear sky retrievals, when filtered and bias corrected, perform nearly as well as full physics retrievals over land surfaces when filtered but never as well as full physics retrievals over oceans.

2.5.2. SUMMARY OF OCO-2 ERROR STATISTICS. Simplified OCO-2 simulations were briefly examined to further test the hypothesis that clear sky retrievals perform as well as

full physics retrievals for perfectly clear scenes (O'Dell et al., 2012). Noiseless simulations without clouds or aerosols and using perfect meteorology (02b OCO-2 simulations) were run. The results showed very small X_{CO_2} errors for both clear sky and full physics retrievals, with the clear sky retrievals having slightly smaller error standard deviations than the full physics retrievals over both land and ocean surfaces. The addition of noise (02d OCO-2 simulations) slightly increased the errors for both retrieval types but did not change the relative performance of the clear sky retrieval compared to the full physics retrieval.

02b NCEP simulations, which are identical to 02b except they use imperfect NCEP meteorology, were also run. The standard deviation of the X_{CO_2} error was approximately 0.35 ppm for the full physics retrievals and 0.66 ppm for the clear sky retrievals. This is likely because the clear sky retrievals were not allowed to use the O_2 A-band to fit for surface pressure and thus the differences between the NCEP meteorology and true meteorology manifested themselves in X_{CO_2} errors. This occurs in the realistic OCO-2 simulations (02e NCEP) as well but the errors are small relative to those caused by other effects such as clouds and aerosols.

For realistic simulated OCO-2 data containing noise, imperfect meteorology, and clouds and aerosols (02e NCEP), values of the standard deviation of the X_{CO_2} error are given in table 2.7 for ocean retrievals. These comparisons did not have to rely on models or TCCON measurements because the true X_{CO_2} value for each retrieval was known. Even with no filtering applied, the clear sky retrievals perform reasonably well compared to the full physics retrievals over ocean surfaces. When roughly 30% of the data is kept, the retrievals are indistinguishable in terms of their error standard deviations. The clear sky algorithm then is able to perform slightly better than the full physics algorithm for throughput levels lower

than ∼30%. At very low throughput levels it is likely that low number statistics prevent any meaningful conclusion.

TABLE 2.7. Standard deviation (σ) of the X_{CO_2} error at different throughput levels using four rules for OCO-2 ACOS B3.4 simulations over ocean.

	No Filtering	70%	50%	30%	10%	5%
σ (Full Physics) [ppm]	3.02	0.96	0.63	0.51	0.39	0.32
σ (Clear Sky) [ppm]	3.27	1.19	0.79	0.51	0.32	0.28

Over land, shown in table 2.8, the clear sky retrievals are unable to match the performance of the full physics retrievals, regardless of filtering amount. However, the clear sky retrieval does perform relatively better as the amount of filtering is increased. This is consistent with my overall hypothesis that clear sky retrievals perform better when scenes contaminated by clouds and aerosols are filtered out.

TABLE 2.8. Standard deviation (σ) of the X_{CO_2} error at different throughput levels using four rules for OCO-2 ACOS B3.4 simulations over land.

	No Filtering	70%	50%	30%	10%	5%
σ (Full Physics) [ppm]	2.54	1.16	0.96	0.81	0.66	0.58
σ (Clear Sky) [ppm]	4.35	1.67	1.26	0.97	0.76	0.66

These statistics are visually represented in figure 2.10. The initial reduction is most dramatic, as the algorithm was able to remove highly contaminated scenes quite easily. All runs tend to level off at throughputs ranging from approximately 50-80%. It is initially obvious that the clear sky retrieval X_{CO_2} error's standard deviation is more comparable to the full physics retrieval over ocean scenes and especially after heavily filtering the data. The initial separation of clear sky land scenes compared to full physics land scenes is large (nearly a 1.5 ppm difference in standard deviations) and only "catches up" to the full physics retrievals at very heavy filtering levels, although this is likely an effect of having too few retrievals to properly analyze.

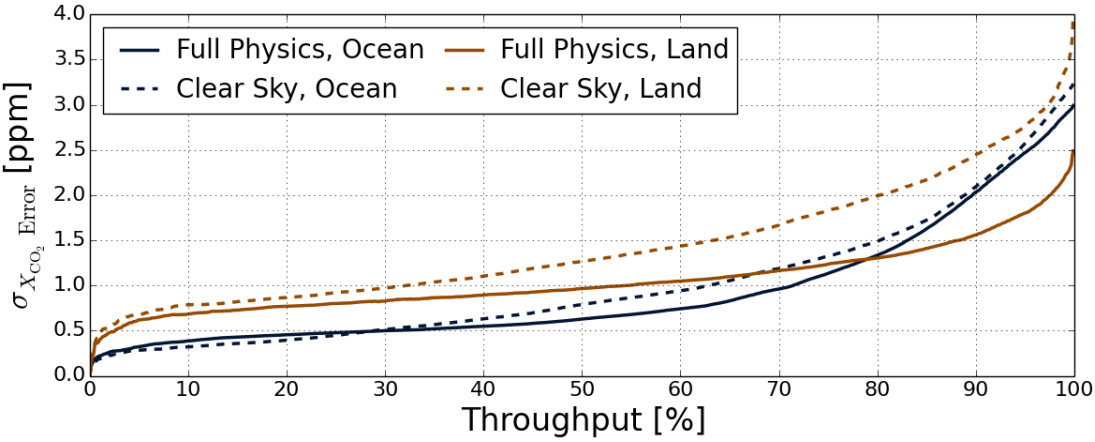

FIGURE 2.10. Genetic algorithm filtering applied to OCO-2 ACOS B3.4 simulations for land (brown) and ocean (blue) surfaces for both clear sky (dashed) and full physics (solid) retrievals. Four genetic algorithm rules were used. The y-axis is the standard deviation of the difference between the retrieved X_{CO_2} and the true X_{CO_2}. The throughput represents the percentage of data that remains after applying the filter.

To determine what type of scenes the genetic algorithm was filtering out, the retrieved X_{CO_2} was compared to the true optical depths used in the simulations without filtering and with 30% throughput. Figure 2.11 demonstrates that the genetic algorithm, when allowed to remove the worst 70% of ocean retrievals, manages to significantly reduce the number of high optical depth scenes. It's seen that the thick, low water clouds are almost entirely filtered out along with many of the thicker ice and aerosol layers. Thus, it can be concluded that the genetic algorithm is highly effective at removing contaminated scenes (true optical depths $>$ 0.3) for OCO-2 retrievals over ocean. The genetic algorithm leaves somewhat contaminated scenes (optical depths of $\sim$0.1-0.3) because its goal is to minimize the standard deviation of the X_{CO_2} error, not to simply remove high optical depth scenes.

For clear sky OCO-2 simulations over land, which have been shown to be less effective than full physics retrievals (table 2.8), figure 2.12 shows that the genetic algorithm is less able to remove scenes contaminated by clouds and aerosols. Specifically, a population of

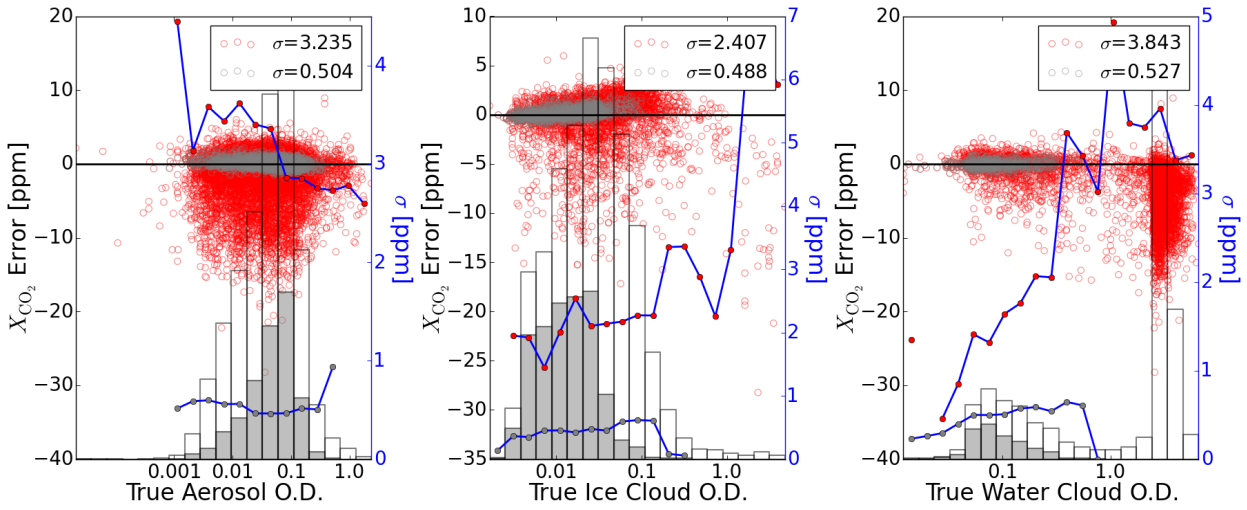

FIGURE 2.11. Clear sky X_{CO_2} retrievals over ocean compared to the true aerosol, ice cloud, and water cloud optical depths for OCO-2 ACOS B3.4 simulations. Grey dots are unfiltered values while red dots are filtered down to a throughput of 30% using the genetic algorithm. The blue dotted lines are binned averages of the standard deviation of the X_{CO_2} errors for unfiltered (red fill) and filtered (grey fill) data. The legends contain σ for the unfiltered and filtered X_{CO_2} values and is different for each subplot because true optical depths of 0.0 are not included. The uncolored bars represent the relative amount of the unfiltered data in each bin while the grey bars are the retrievals that remain after filtering.

the thick water clouds remains. However, the genetic algorithm still effectively reduced the X_{CO_2} errors (blue line with grey fill), even for the thick water clouds. If the filtering is significantly increased, the high optical depth scenes are eventually removed (not shown). Unfortunately this type of analysis cannot be done with GOSAT retrievals because the number of comparisons to AERONET is insufficient.

Noiseless scenes containing clouds and aerosols and imperfect meteorology (02c NCEP) were briefly examined to test the effect of removing noise from the realistic 02e NCEP OCO-2 simulations. It was found that the overall error statistics were slightly better than for the 02e NCEP runs. Typically the standard deviation of the X_{CO_2} error decreased by a few percent for all datasets tested. This again indicates that noise in the OCO-2 simulations plays only a minor role in the final X_{CO_2} error distribution.

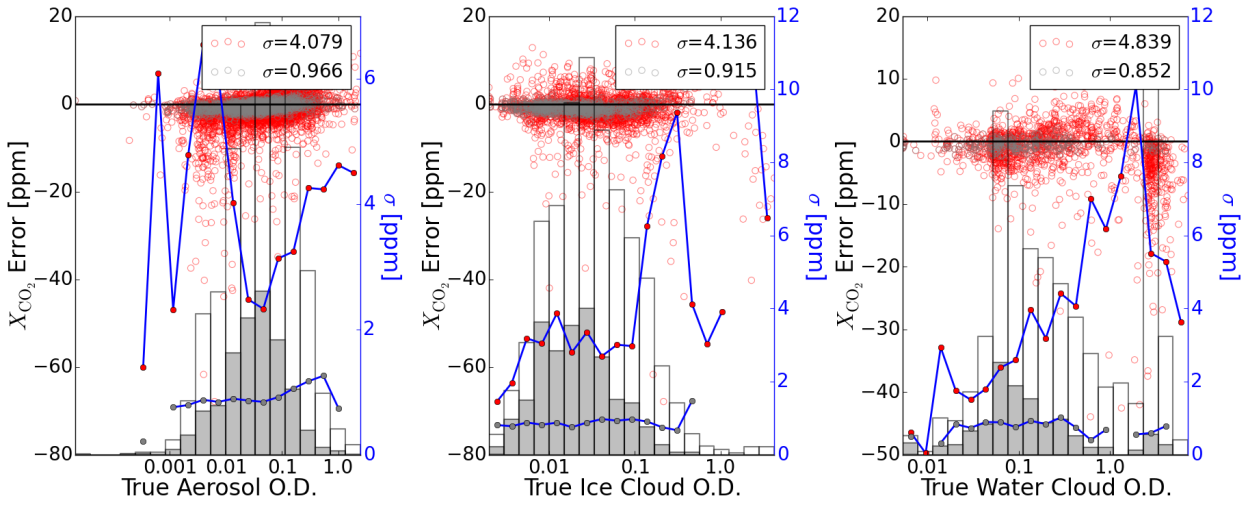

FIGURE 2.12. Clear sky X_{CO_2} retrievals over land compared to the true aerosol, ice cloud, and water cloud optical depths for OCO-2 ACOS B3.4 simulations. Grey dots are unfiltered values while red dots are filtered down to a throughput of 30% using the genetic algorithm. The blue dotted lines are binned averages of the standard deviation of the X_{CO_2} errors for unfiltered (red fill) and filtered (grey fill) data. The legends contain σ for the unfiltered and filtered X_{CO_2} values and is different for each subplot because true optical depths of 0.0 are not included. The uncolored bars represent the relative amount of the unfiltered data in each bin while the grey bars are the retrievals that remain after filtering.

Besides the standard deviation of the X_{CO_2} error, the reduced χ^2 was also used to assess the performance of the retrieval algorithms. Figure 2.13 shows the reduced χ^2 for the weak and strong CO_2 bands over all surface types. The clear sky retrievals (red) perform worse (higher χ^2 values) than the full physics retrievals (black), especially for the strong CO_2 band. Filtering has the ability to remove many of the large χ^2 values found in the clear sky retrieval but it still cannot perform as well as the full physics retrieval.

An analysis of simulated OCO-2 data was also done for regions determined to be over snow or ice. Full physics retrievals are often unable to make accurate X_{CO_2} measurements over snow and ice because those surfaces are very dark in the near-infrared, where the weak and strong CO_2 bands are located (O'Dell et al., 2012). The ground track of polar orbiting satellites, such as GOSAT, provides substantially more data over polar regions than the

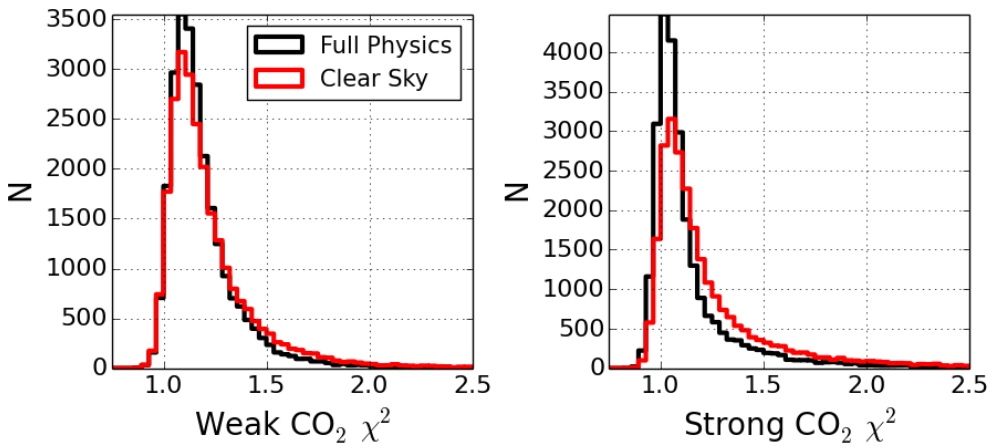

FIGURE 2.13. Distribution of full physics (black) and clear sky (red) χ^2 values from OCO-2 ACOS B3.4 simulated data for the weak CO_2 and strong CO_2 bands.

tropics and it was hypothesized that the amount of data alone could lead to accurate X_{CO_2} estimates by employing averaging techniques to try and reduce the noise. However, the errors for both clear sky and full physics retrievals were too large and thus any data collected over ice or snow currently appears to be of little value.

Here I have shown that OCO-2 simulation clear sky retrievals perform almost as well as full physics retrievals over ocean surfaces, where the genetic algorithm is able to effectively remove scenes contaminated by clouds and aerosols. Over land, however, extremely high levels of filtering are needed to make the clear sky X_{CO_2} errors comparable to the full physics errors. This contrasts the results for GOSAT data, where clear sky retrievals performed well over land when filtered but not as well over ocean. I have also shown that, in general, the retrieval algorithm is less able to fit the spectra for clear sky retrievals, especially in the strong CO_2 band.

2.6. RADIANCE RESIDUAL FITTING

The performance of a retrieval algorithm is tied closely with how well it can fit the measured radiance spectra. Analysis was done on both the GOSAT and OCO-2 datasets

to determine if the clear sky retrievals were fitting the spectra as well as the full physics retrievals. This could potentially provide clues as to why the clear sky retrievals are generally unable to consistently perform as well as the full physics retrievals.

Recent editions of the GOSAT ACOS X_{CO_2} retrieval algorithm (B3.4 and later) contain three empirical orthogonal functions (EOFs), one for each band. EOF analysis works by splitting a matrix into linearly independent parts, each of which explains a certain amount of the dataset's variance. The first EOF pattern explains the maximum amount of variance, the second pattern explains the next largest amount of variance, and so on. To derive the initial value of these parameters, several thousand L1B measurements are run through the L2 retrieval code as a baseline. The first EOF pattern of the spectral residuals is then allowed to be fit by the L2 retrieval algorithm. Here the residual is defined as the radiances modeled by the algorithm minus the true measured radiances. The algorithm is allowed to fit the first EOF using a scale factor to adjust the magnitude of the pattern. All the L1B measurements are then re-run with the most prominent residual pattern in hopes that the algorithm will be able to use the function to more effectively reduce the spectral residuals even further.

An initial comparison between clear sky residuals and full sky residuals was done. It was then hypothesized that the EOF pattern being used in both clear sky and full physics retrievals was not optimal for clear sky retrievals because it was derived from full physics retrievals and would thus not contain patterns induced by unmodeled scattering by clouds and aerosols. The clear sky retrievals were then run with EOF fitting turned off to try and find a customized clear sky residual pattern. It was determined that for this study the mean residual pattern was suitable to be used, rather than the first EOF of the residuals. The clear sky retrievals were then re-run with the new, customized residual pattern. Ocean scenes were primarily examined because that is where the largest differences in X_{CO_2} errors between

clear sky and full physics GOSAT retrievals were found (see section 2.5). The strong CO_2 band was looked at because it showed a larger difference in the χ^2 of the residuals between the two retrieval types (see figure 2.13). A newer ACOS B4.0 dataset was used for the clear sky retrieval tests and they were compared to full physics retrievals run using ACOS B3.4. Because the major changes from ACOS B3.4 to ACOS B4.0 relate only to aerosol parameterization, clear sky retrievals run with ACOS B3.4 are essentially identical to those run with B4.0.

After analyzing GOSAT clear sky residual fitting tests, OCO-2 clear sky simulation residuals were examined to determine if the amount of aerosol in a scene is directly proportional to the magnitude of the spectral residuals. It was hypothesized that filtering out high aerosol scenes would only leave retrievals with small residuals. This would suggest that the clear sky retrievals perform better, at least in terms of spectral residuals, for very clear scenes. Conversely, high aerosol scenes were also examined for clear sky retrievals with the hypothesis that these retrievals would have large residuals. Noiseless simulations free of clouds and aerosols and containing perfect meteorology (02b) were then run to further test the hypothesis that large residuals in the clear sky retrievals are caused by cloud and aerosol contamination.

2.6.1. GOSAT Clear Sky Residual Fitting. For normal retrievals that use a full physics EOF fit, the strong CO_2 residual patterns of 445 full physics ocean retrievals (black) and their corresponding clear sky versions (red) are shown in figure 2.14. It's clear that the full physics algorithm is better able to minimize the residuals. Overall, the residual patterns are similar but the magnitude is greater for the clear sky retrievals. The difference pattern shown in the bottom panel is likely due to scattering and absorption by clouds and aerosols that is not accounted for in the clear sky retrievals. The clouds and aerosols modify the

light path and thus cause an increase or decrease in radiances measured by the satellite at certain wavelengths, which causes the "sawtooth" pattern. This provided motivation to try and reduce the clear sky residuals by fitting for a custom mean residual pattern, as described above.

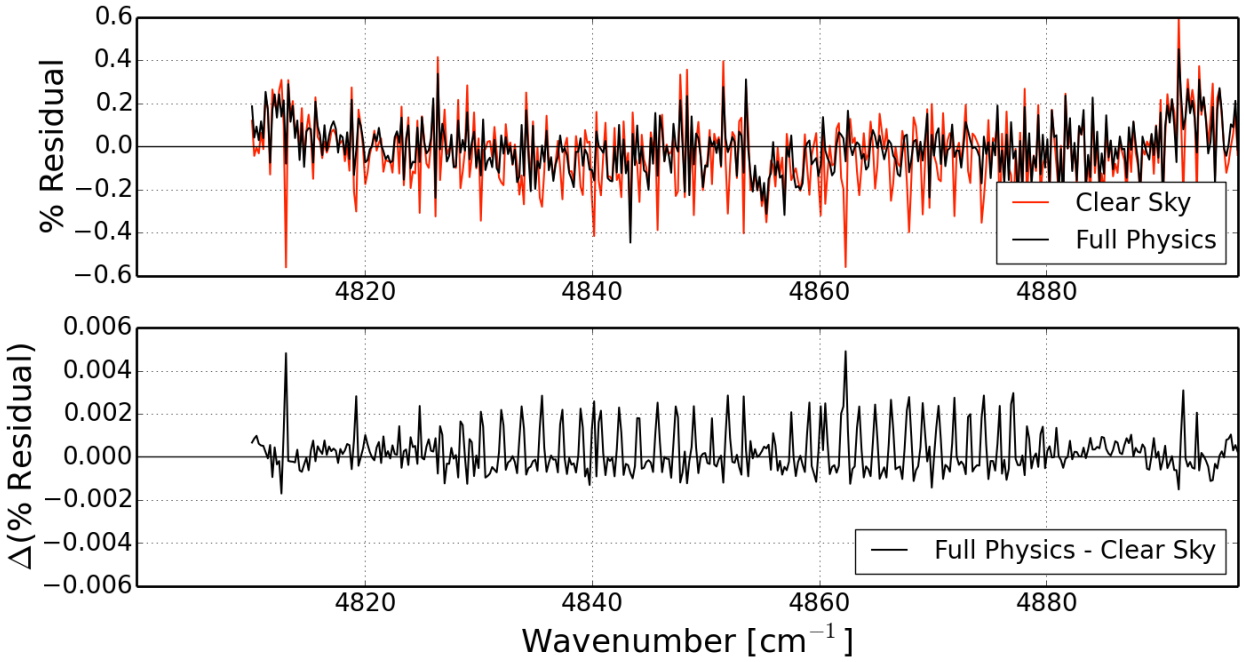

FIGURE 2.14. The top panel shows the strong CO_2 spectral residuals (modeled radiances - measured radiances) percentages over ocean for full physics (black) GOSAT ACOS B3.4 retrievals and clear sky (red) GOSAT ACOS B4.0 retrievals. The bottom panel shows the difference in the residual percentages (full physics - clear sky).

Finding custom residual patterns for the clear sky ocean retrievals was done by turning off fitting for the first EOF in all bands (for the clear sky retrievals only the two CO_2 bands were used). The results are shown in figure 2.15. The normal full physics retrieval with EOF fitting enabled is again shown in black as a comparison. The new clear sky retrievals have much larger spectral residuals than both the full physics retrievals and the baseline clear sky residuals (figure 2.14). There are significant residual spikes at most wave numbers in the band and often times the sign of the residual is opposite that of the full physics residual.

This was rarely the case in the baseline test, where the clear sky residuals were simply larger in magnitude. This suggests that fitting for the residuals has a significant impact in both the sign and magnitude of the final residual pattern. This new clear sky strong CO_2 residual pattern (shown in red), along with the weak CO_2 pattern (not shown), were then saved for use in the customized clear sky retrieval algorithm.

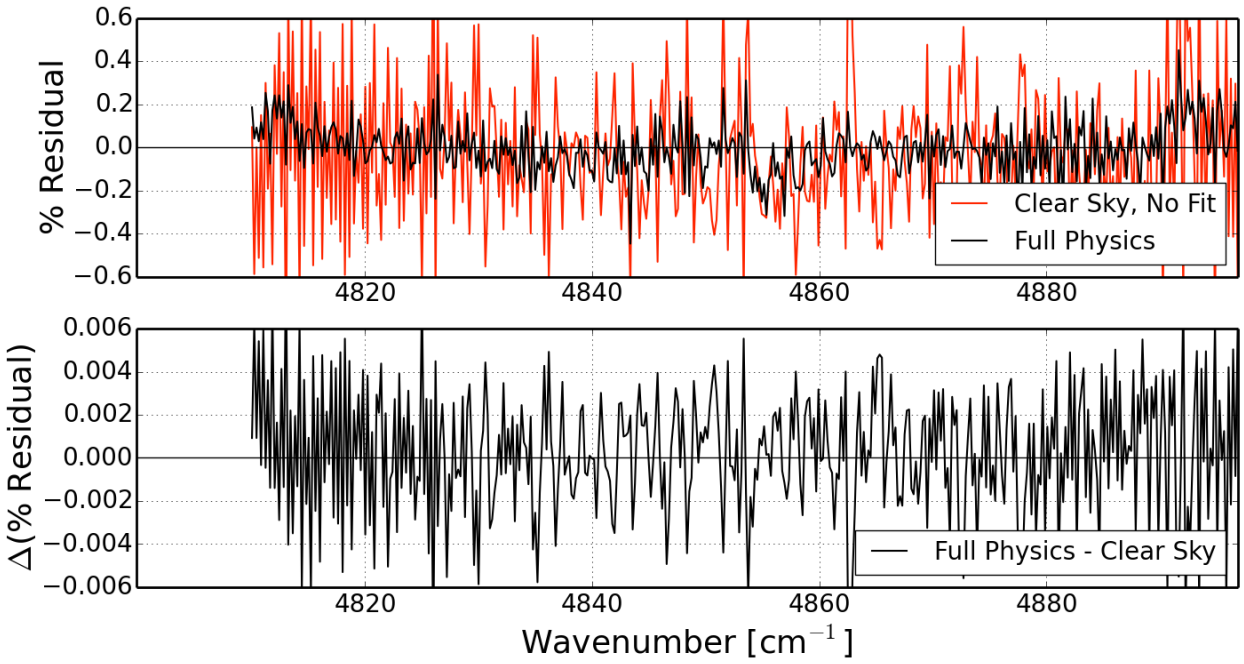

FIGURE 2.15. The top panel shows the strong CO_2 spectral residuals (modeled radiances - measured radiances) percentages over ocean for full physics (black) GOSAT ACOS B3.4 retrievals and clear sky (red) GOSAT ACOS B4.0 retrievals. The bottom panel shows the difference in the residual percentages (full physics - clear sky). Residual EOF fitting was disabled for the clear sky (red) retrievals.

Allowing the retrieval algorithm to fit for the new clear sky residual pattern results in the strong CO_2 residuals in figure 2.16. The normal full physics residuals (black) are again plotted for comparison purposes. The clear sky residuals (red) were successfully reduced to lower magnitudes than the initial residuals seen in figure 2.14. They are also, on average,

smaller in magnitude than the full physics residuals. This shows that, as hypothesized, customizing the residual fitting pattern was successful in reducing the clear sky residuals.

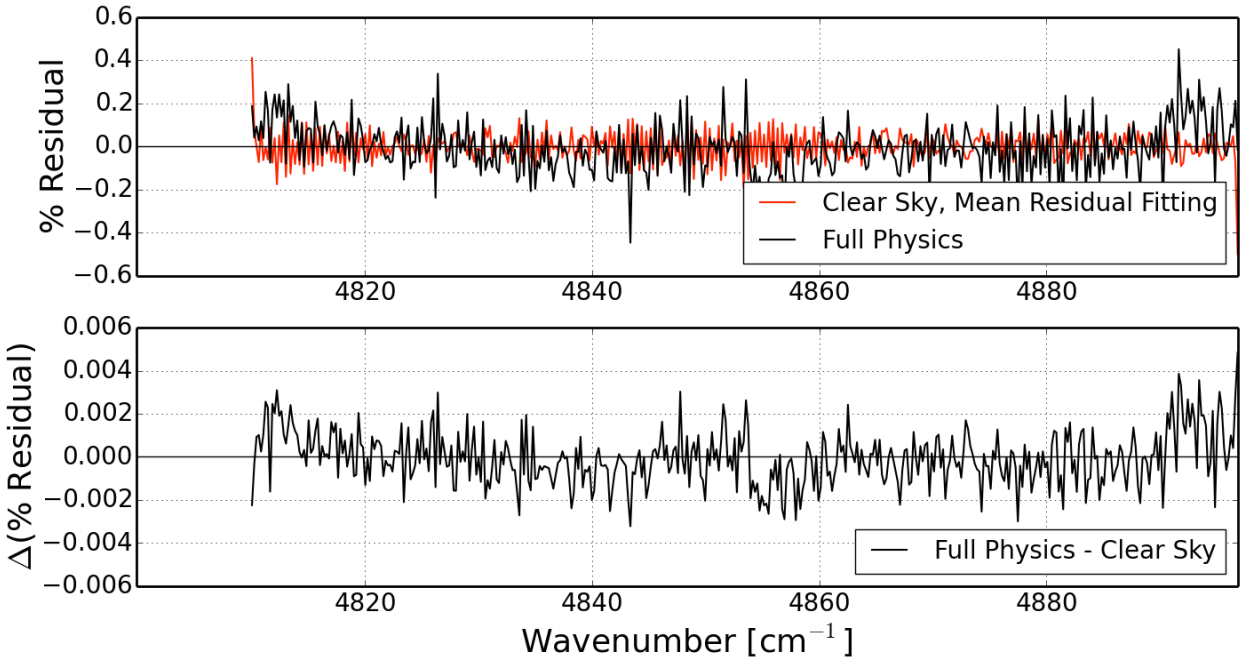

FIGURE 2.16. The top panel shows the strong CO_2 spectral residuals (modeled radiances - measured radiances) percentages over ocean for full physics (black) GOSAT ACOS B3.4 retrievals and clear sky (red) GOSAT ACOS B4.0 retrievals. The bottom panel shows the difference in the residual percentages (full physics - clear sky). The clear sky retrievals were allowed to fit for the mean residual pattern of the clear sky retrievals with EOF fitting disabled (clear sky residual pattern in figure 2.15).

To examine whether or not the reduction of clear sky spectral residuals over ocean was effective in reducing the overall X_{CO_2} errors, the standard deviation of the errors for all cases in this section were calculated and are shown in table 2.9.

TABLE 2.9. Standard deviation of the X_{CO_2} error for GOSAT ACOS B3.4 and B4.0 retrievals over ocean using different residual fitting patterns.

Retrieval Type	ACOS Build	$\sigma_{X_{CO_2}\ \text{error}}$
Full Physics	ACOS B3.4	1.09 ppm
Clear Sky	ACOS B4.0	1.63 ppm
Clear Sky (no fitting)	ACOS B4.0	1.62 ppm
Clear Sky (custom fit)	ACOS B4.0	1.60 ppm

The initial GOSAT clear sky errors are, as shown in section 2.5, significantly worse than the full physics retrieval errors. Interestingly, when residual fitting is turned off for clear sky retrievals the standard deviation of the X_{CO_2} errors stays approximately the same. It was hypothesized that the errors would be larger because, as shown in figure 2.15, the magnitude of the residuals is much greater. This suggests a lack of correlation between residual magnitude and X_{CO_2} errors, at least for clear sky GOSAT retrievals over ocean. This conclusion is supported by looking at the residuals over land, where the clear sky retrievals perform statistically about as well as the full physics retrievals. The same clear sky residual pattern over ocean appears in the retrievals over land (not shown).

When clear sky retrievals were run with a custom residual pattern, the standard deviation of the X_{CO_2} errors is only marginally reduced compared to the baseline clear sky run (-0.03 ppm) and no-fit run (-0.02 ppm). This supports the previous claim in that a significant reduction in residuals doesn't necessarily mean a significant reduction in GOSAT X_{CO_2} errors. An examination of X_{CO_2} errors compared to other measured and retrieved parameters (not shown) revealed all three clear sky versions have similar biases and correlations with most parameters. The most significant changes are, not surprisingly, involve the scaling factor of the residual fits themselves.

Overall, these tests suggest that reducing the clear sky residuals plays only a minor role in minimizing the X_{CO_2} error in real GOSAT retrievals.

2.6.2. OCO-2 Clear Sky Residuals. OCO-2 simulation residuals were then examined because of the potential to filter the data using the true aerosol optical depths. That is, to be able to further test the hypothesis that the clear sky retrieval performs better for very clear scenes. The strong CO_2 band residuals for both full physics and clear sky simulated OCO-2 retrievals over ocean are shown in figure 2.17. Confirming work done in section 2.6.1,

the clear sky residuals (red) are larger in magnitude than the full physics residuals (black). The sawtooth pattern seen in the GOSAT residuals (figure 2.14) is also seen in figure 2.17. This is encouraging because provides evidence that the simulated OCO-2 clear sky retrievals behave like clear sky retrievals run on real GOSAT data, at least in terms of their residual patterns. The sawtooth pattern, as previously mentioned, is because the clear sky algorithm doesn't try and account for light path length modification due to clouds and aerosols. The clear sky residuals are also frequently the opposite sign of the full physics residuals, a feature also seen in clear sky GOSAT retrievals with residual fitting disabled (figure 2.15). This is likely an artifact of the sawtooth effect just described.

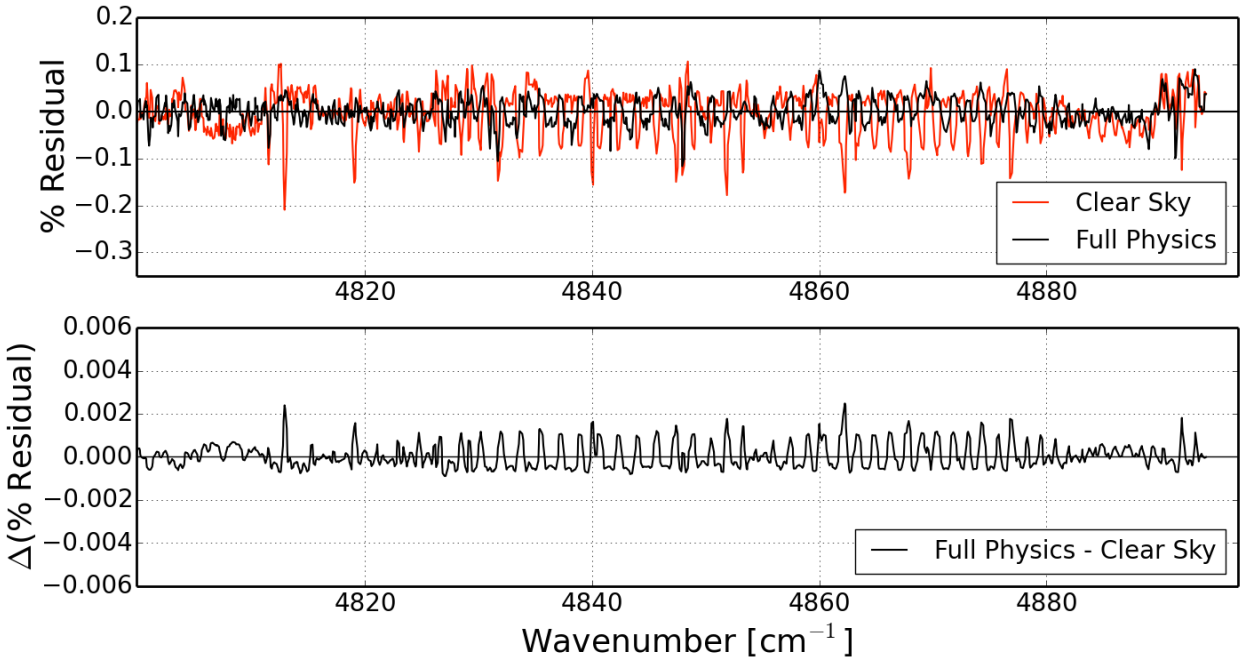

FIGURE 2.17. The top panel shows the strong CO_2 spectral residuals (modeled radiances - measured radiances) percentages over ocean for full physics (black) and clear sky (red) OCO-2 ACOS B3.4 retrievals run on 02e NCEP scenes. The bottom panel shows the difference in the residual percentages (full physics - clear sky).

Filtering out simulated scenes with total true optical depths (water cloud + ice cloud + aerosols) of greater than 0.03 results in the residuals shown in figure 2.18. Compared to

the baseline residuals (figure 2.17), retrievals of scenes with very low optical depths have moderately lower residuals across most of the spectrum. The sawtooth pattern seen in the clear sky residuals of figure 2.17 is no longer present and both the full physics and clear sky retrieval residuals look more random. However, the sawtooth pattern is still seen when differencing the two retrieval types (lower panel) but with a smaller magnitude compared to the baseline runs. This suggests that even a small amount of clouds or aerosols can induce a residual pattern in the clear sky retrievals.

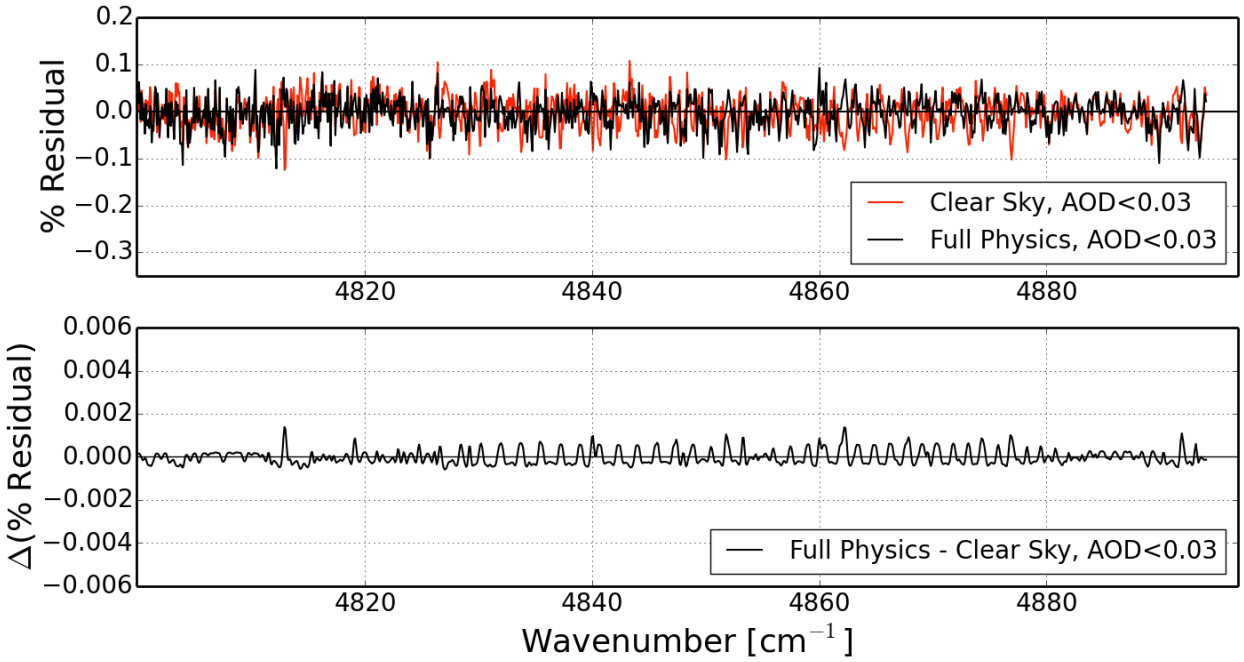

FIGURE 2.18. The top panel shows the strong CO_2 spectral residuals (modeled radiances - measured radiances) percentages over ocean for full physics (black) and clear sky (red) OCO-2 ACOS B3.4 retrievals run on 02e NCEP scenes. The bottom panel shows the difference in the residual percentages (full physics - clear sky). Scenes with optical depths greater than 0.03 were filtered out.

Looking at high optical depth cases should reveal larger residual patterns than the baseline runs. Figure 2.19 shows that this is the case. The sawtooth pattern in the baseline runs is amplified considerably and very pronounced in the differencing (lower panel).

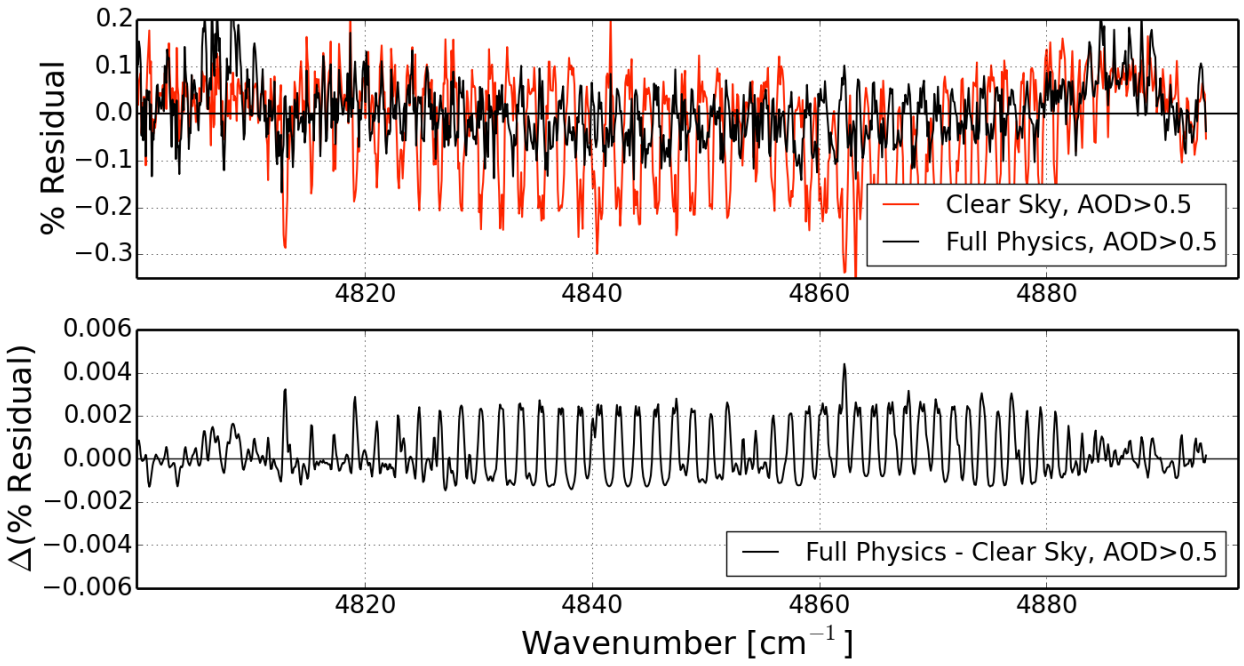

FIGURE 2.19. The top panel shows the strong CO_2 spectral residuals (modeled radiances - measured radiances) percentages over ocean for full physics (black) and clear sky (red) OCO-2 ACOS B3.4 retrievals run on 02e NCEP scenes. The bottom panel shows the difference in the residual percentages (full physics - clear sky). Scenes with optical depths less than 0.5 were filtered out.

As figures 2.18 and 2.19 suggest, the residual patterns in the clear sky ocean retrievals are likely caused by clouds and aerosols. This was confirmed by running 02b ocean simulations which are noiseless, contain no clouds or aerosols, and use perfect meteorology (as opposed to the normally used 02e NCEP OCO-2 simulations, which are more realistic). The residuals for clear sky (red) and full physics (black) retrievals are shown in the top panel of figure 2.20 while the difference is shown in the bottom panel of figure 2.20. Noticeable differences can be seen in the residuals along with an overall low bias for the full physics retrievals and a seemingly better fit for the clear sky retrievals. Overall, as hypothesized, the residuals are smaller than any of the other tests, especially for the clear sky retrievals. This is because the scenes contained no noise, clouds, or aerosols and thus the retrieval algorithm was better able to fit the spectra. The relative differences shown in the bottom panel are quite small.

This confirms the hypothesis that even small amounts of clouds and aerosols can contribute significantly to the clear sky retrieval's inability to properly fit the spectra.

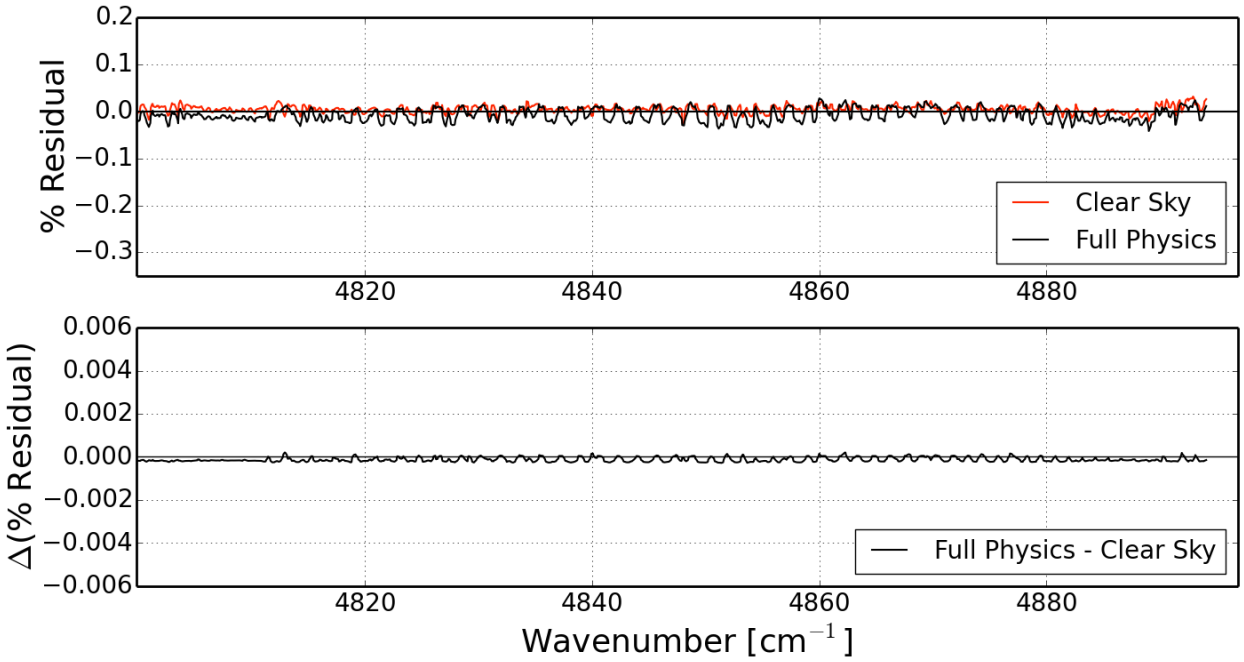

FIGURE 2.20. The top panel shows the strong CO_2 spectral residuals (modeled radiances - measured radiances) percentages over ocean for full physics (black) and clear sky (red) OCO-2 ACOS B3.4 retrievals run on 02b scenes. The bottom panel shows the difference in the residual percentages (full physics - clear sky).

2.7. CLEAR SKY X_{CO_2} SUMMARY

In this chapter I compared clear sky X_{CO_2} retrievals to full physics X_{CO_2} retrievals. The use of the genetic algorithm revealed that it is an effective tool in removing contaminated retrievals not caught by pre-filtering from X_{CO_2} datasets. Typically, only 2-5 rules were needed to maximize the effectiveness of filtering. Some of these rules (e.g. the CO_2 ratio) have the potential to be used as a pre-filter because their value is known before running the L2 code. This is useful because the L2 code is computationally expensive so having the

ability to identify low quality measurements early on will potentially allow for additional measurements to be run through the L2 code.

From applying the genetic algorithm and bias corrections to the retrieval datasets and computing various statistics, it can be concluded that the clear sky algorithm typically does not perform as well as the full physics algorithm. Analysis of real GOSAT data revealed that the clear sky retrieval is generally unable to match the performance of the full physics retrieval. For real data over ocean the clear sky retrieval is generally worse than the full physics retrieval while over land it is somewhat more comparable, but only after significant filtering and a bias correction.

Simplified OCO-2 simulations were run and it was found that, as hypothesized, clear sky retrievals can perform as well as full physics retrievals for scenes free of clouds and aerosols. For realistic simulations, however, clear sky OCO-2 retrievals are comparable to full physics OCO-2 retrievals only when high levels of filtering are applied. This filtering is effective at removing low quality retrievals, which typically include scenes contaminated by clouds and aerosols. Over ocean, keeping 30% of the data results in the two retrieval types being indistinguishable in terms of their X_{CO_2} errors while over land much higher levels of filtering are needed for the clear sky retrievals to be comparable to the full physics retrievals.

Despite generally not performing as well as the full physics algorithm, the clear sky algorithm still typically manages to retrieve X_{CO_2} errors less than 2.0 ppm when modestly filtered. Additionally, the computational efficiency of clear sky retrievals means they may yet be useful for certain applications that require a large number of retrievals but have more relaxed error requirements.

An analysis of residual patterns from clear sky and full physics GOSAT retrievals revealed that the clear sky spectral residuals can be reduced by fitting for a customized mean residual

pattern. However, this improvement in the residuals not directly result in a significant reduction of X_{CO_2} errors. For OCO-2 simulations, it was shown that filtering out all but the clearest scenes results in a significant reduction in the clear sky residuals. However, patterns caused by unmodeled clouds and aerosols are still visible in the clear sky residuals, even for the clearest scenes.

Overall, the clear sky retrievals are generally inferior to full physics retrievals for both simulated OCO-2 data and real GOSAT data, except for when high levels of filtering are applied to remove low quality retrievals.

CHAPTER 3

Aerosol Comparison

In the previous chapter it was shown that simply ignoring clouds and aerosols is generally not effective in reducing X_{CO_2} errors. This means that trying to fit for aerosols is beneficial. However, is the aerosol parameterization in ACOS accurately measuring clouds and aerosols? If not, this would suggest that there is likely room for improvement in the aerosol scheme.

This chapter is dedicated to investigating whether or not the aerosol parameterization in ACOS is able to accurately gain information about clouds and aerosols. If the retrieval algorithm is unable to realistically represent clouds and aerosols it suggests that other methods could be used to try and improve the retrieval. First, the ability of the ACOS X_{CO_2} retrieval algorithm to properly measure aerosol optical depths is assessed both quantitatively and spatially. The spatial distribution of the types of aerosols selected by the algorithm is also investigated to see if regional patterns are present. Finally, the placement of aerosol layers in OCO-2 simulations is studied to see if the algorithm is able to accurately determine the true height and to see if the placement of the aerosol layers is correlated with X_{CO_2} errors. If these analyses demonstrate the inability of ACOS to retrieve information about clouds and aerosols, it suggests other methods are needed to handle the errors caused by them. This study also investigates whether changes made in the aerosol scheme from ACOS B3.4 to B3.5 resulted in an improvement of the retrieved aerosol properties.

3.1. Comparison to AERONET

3.1.1. AERONET Aerosol Optical Depth Measurements. AERONET is a collection of ground-based sun photometers designed to provide globally distributed observations of spectral optical depth, precipitable water, and other variables relating to aerosols

(Holben et al., 1998). They provide a cloud-screened, quality-assured product that spans several years and has data at hundreds of locations around the globe. Figure 3.1 shows the location of all AERONET stations active at some point during 2014.

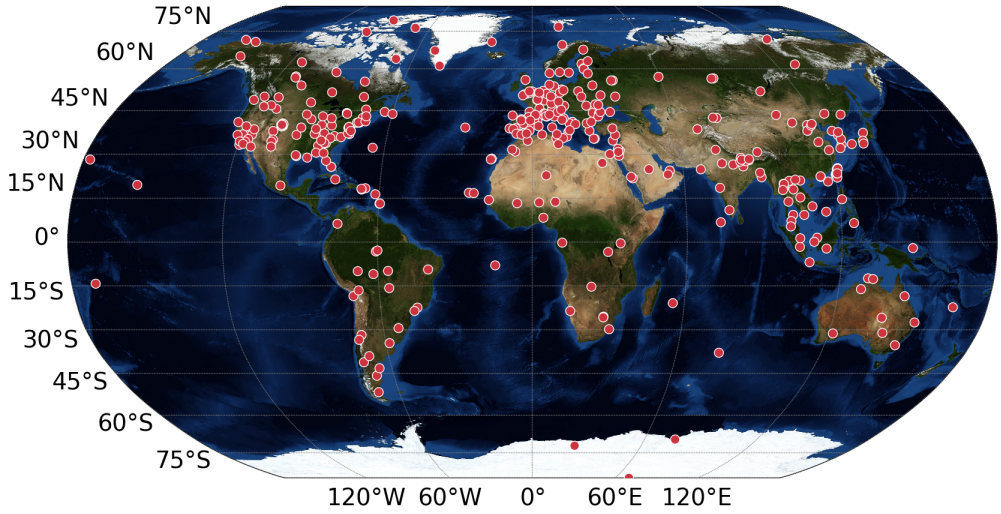

FIGURE 3.1. AERONET stations active in 2014.

This network was used to analyze the X_{CO_2} retrieval's effectiveness at gathering information about the scene's aerosol profile. This is because ground-based sun photometers have the ability to be much more accurate than space-based instruments; the uncertainty for a newly calibrated AERONET sun photometer under cloud-free conditions is typically $< \pm$ 0.01 for wavelengths relevant to this study (Holben et al., 1998). There are many AERONET stations across the globe that overlap in time and space with GOSAT measurements. For this analysis, only AERONET measurements that were co-located with GOSAT measurements to within 0.1 degrees and 30 minutes were used.

3.1.2. COMPARING AERONET AEROSOL OPTICAL DEPTH TO GOSAT. To determine if the aerosol properties measured from the retrieval algorithm were realistic, a comparison against AERONET data was done. Since the true aerosol properties are known for simulated retrievals, this work was only done on real GOSAT data. The initial portion of

this part of the study was completed before the implementation of ACOS B3.4 and thus an older dataset run with B2.10 was used (the aerosol scheme was not changed from ACOS B2.10 to B3.4). Since the aerosol properties of the atmosphere vary highly in both time and space, strict co-location criteria were implemented. For a GOSAT retrieval to be used it was required to be measured within 30 minutes and roughly 11 km (0.1 degrees) of the AERONET measurement. The frequency of measurements made by AERONET is variable and depends on the air mass but is typically no lower than one measurement every 15 minutes (Holben et al., 1998). If multiple AERONET measurement were made within a single 30 minute time segment they were averaged.

AERONET stations only measure at certain wavelengths so in order to compare AERONET measurements to the retrieved aerosol optical depth at 0.755 μm from GOSAT, the AERONET optical depths at 0.675 μm and 0.870 μm were averaged. This technique relies on the assumption that the Ångström exponent is low for this wavelength region. The number of AERONET stations is significant, with hundreds of sites currently in operation. However, they are still regionally biased and only present on land. This essentially removes the possibility to validate a significant number of oceanic GOSAT aerosol measurements. Different co-location thresholds were also tested, but it was felt that these time and space criteria best represented a balance between actually comparing the same column of air and having enough measurements to ensure a robust analysis.

The AERONET dataset was also compared with other retrieval algorithms including RemoTeC (version 2.0) from the Karlsruhe Institute of Technology (KIT) and another from Japan's National Institute for Environmental Studies (NIES) (version v02). This was to analyze other retrieval algorithms' ability to gain information about aerosols.

3.1.3. GOSAT Aerosol Optical Depth Validation Analysis. For ACOS B2.10, figure 3.2 demonstrates the lack of significant correlation (R=0.33) between the AERONET aerosol optical depths and the retrieved GOSAT aerosol optical depths. There is also a high bias present in the data. The analyzed data is from all AERONET measurements that met the previously described co-location criteria, so it may contain regional biases but an investigation of individual sites revealed the lack of correlation is ubiquitous.

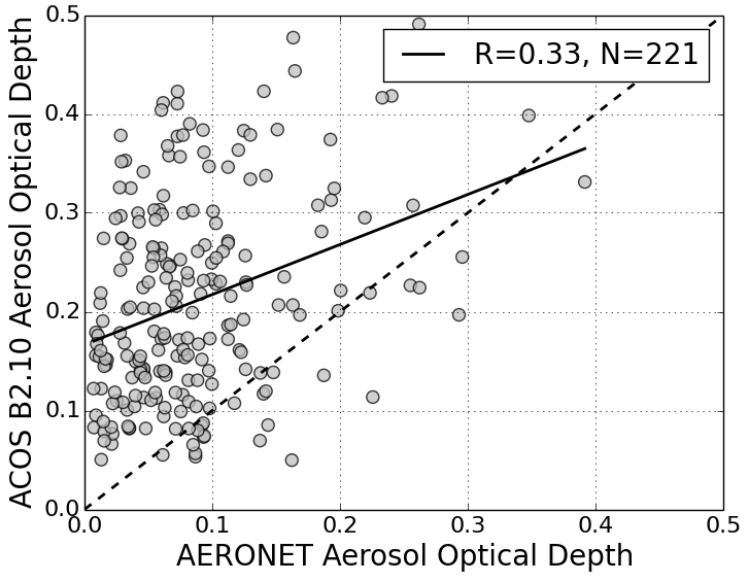

Figure 3.2. AERONET aerosol optical depth compared to the retrieved ACOS B2.10 aerosol optical depth from GOSAT data. A linear fit is shown by the solid black line.

After analysis had begun on the clear sky X_{CO_2} retrievals using an updated version of the retrieval algorithm (ACOS B3.4), this work was revisited and a comparison was done comparing the newer algorithm's aerosol optical depths to AERONET. The results in figure 3.3 show a slightly more promising distribution with a lower bias at small optical depths but still a significant amount of scatter at large aerosol optical depth values. Notice the number of comparisons had increased due to more data having been collected. Interestingly,

the improvements resulted from general improvements to other parts of the algorithms and not changes in the aerosol scheme itself.

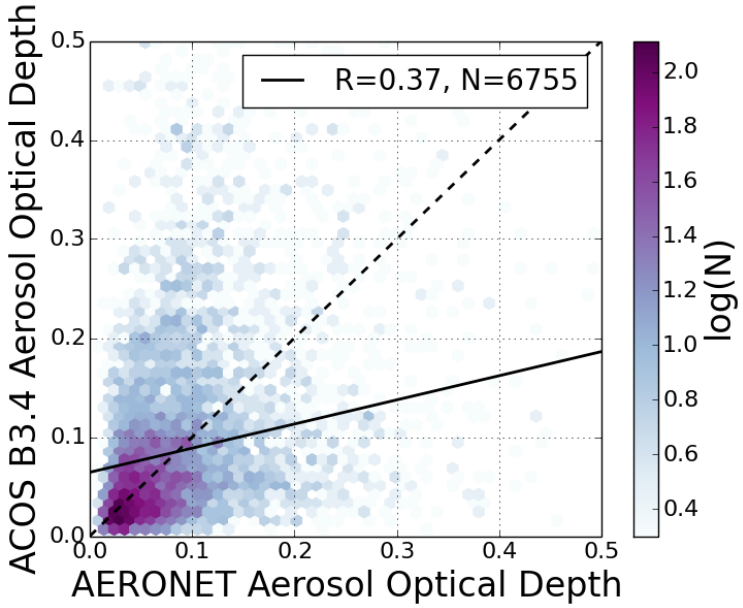

FIGURE 3.3. AERONET aerosol optical depth compared to the retrieved ACOS B3.4 aerosol optical depth from GOSAT data. A linear fit is shown by the solid black line.

Figure 3.4 shows how retrieved aerosol optical depths compare to AERONET for the updated MERRA aerosol scheme in ACOS B3.5. The correlation has improved slightly but overall the changes are minimal, despite significant modifications to the aerosol scheme.

Besides ACOS, RemoTeC and NIES aerosol optical depths were also briefly investigated. It was found that RemoTeC (not shown) retrieved similar aerosol optical depths compared ACOS B3.4, despite having a fundamentally different aerosol scheme, while NIES often greatly underestimated the amount of aerosols in the column. These comparisons show that obtaining accurate information about aerosol content is fundamentally difficult for any retrieval algorithm, including ACOS.

In this section I have shown that the retrieved aerosol optical depths from GOSAT retrievals are not well-correlated with AERONET aerosol optical depths. This suggests that

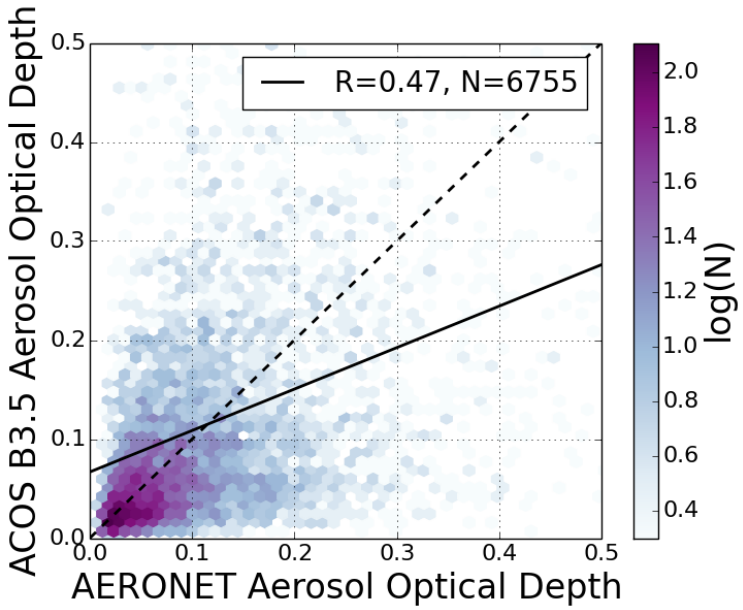

FIGURE 3.4. AERONET aerosol optical depth compared to the retrieved ACOS B3.5 aerosol optical depth from GOSAT data. A linear fit is shown by the solid black line.

X_{CO_2} retrieval algorithms, when applied to real GOSAT data, are unable to accurately gain information about cloud and aerosol amounts.

3.2. OCO-2 Aerosol Optical Depth

Besides comparing real GOSAT data to AERONET, retrieved aerosol optical depths from OCO-2 simulations can be compared to the true optical depths used in the scene. The retrieved optical depths were compared to the true optical depths to evaluate the algorithm's ability to accurately retrieve cloud and aerosol amount information. Analyzing OCO-2 simulations in addition to GOSAT retrievals is useful because, unlike AERONET, the aerosols scenes used in the OCO-2 simulations are exactly represented by the retrievals. No co-location or error assumptions are needed and every aspect of the simulated aerosol scenes can be controlled. Simulated measurements and retrievals are also useful compared to GOSAT measurements because they do not contain unknown instrument errors and biases.

For realistic simulated OCO-2 ACOS B3.4 data (see section 2.1 for simulation details), a comparison of retrieved aerosol optical depths to true aerosol optical depths is shown in figure 3.5. This shows clearly that many scenes with high water cloud optical depths (lower left panel) are not removed by pre-filtering. This is likely because the measured spectra are seen as being consistent with a low optical depth scene. These scenes contain low level water clouds that are undetected by the retrieval algorithm and not caught by any of the pre-filters (see section 2.1). These low water clouds can be somewhat effectively removed by filtering (not shown) but many contaminated measurements still remain. An interesting feature can be seen in the Kahn type comparison (upper right panel): a horizontal cluster of retrieved aerosol optical depths around 0.0125. This turned out to be retrievals that didn't vary much from the prior optical depth. Two faint subpopulations of low true aerosol optical depths can also be seen in the same aerosol panel (upper right). These are primarily located at high latitudes and are an artifact of Cloud-Aerosol Lidar with Orthogonal Polarization (CALIOP) aerosol profiles, described in section 2.1.3.

Besides the water cloud outliers, there is a low bias in the retrieved total optical depths compared to the true total optical depths (lower right panel). The correlation coefficient is $\sim$0.40 between the retrieved and true total optical depths (excluding low water clouds) and thus it can be concluded that the total optical depth can only be somewhat accurately retrieved in realistic OCO-2 simulations. Individual aerosol types are even less constrained in the retrieval and may deviate significantly from their true values. For aerosols, the correlation is a mere $\sim$0.07 while for water cloud it's 0.18. The ice cloud also has a correlation coefficient of 0.03.

ACOS B3.5, which uses the MERRA setup instead of generic Kahn aerosol types, is similar to ACOS B3.4 in most other respects and thus in comparing the two the impact

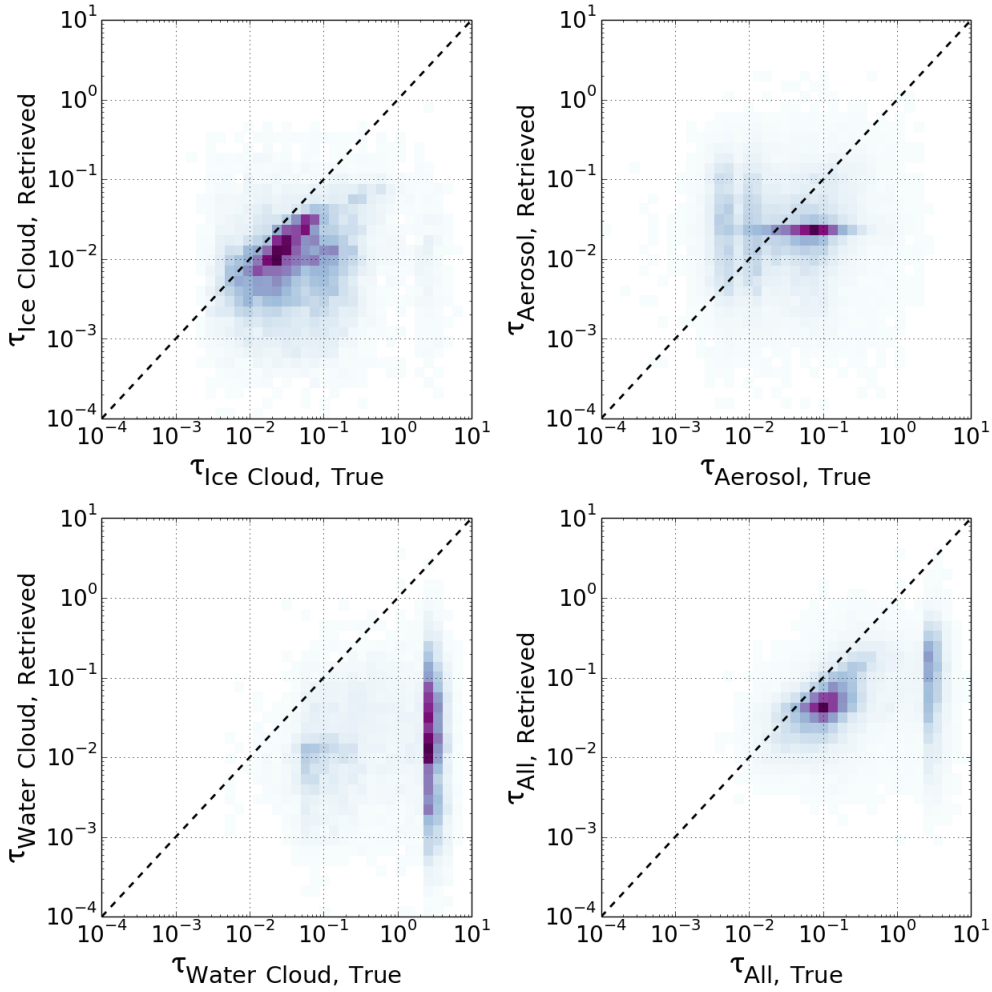

FIGURE 3.5. Heat map of the true optical depths compared to the retrieved ACOS B3.4 optical depths from OCO-2 simulations. Optical depths are compared for the ice cloud, the combined Kahn 2b and Kahn 3b aerosol layer, the water cloud, and the total combined aerosol layer.

of changing the aerosol parameterizations can be assessed. Figure 3.6 shows the retrieved optical depths compared to the true optical depths. The horizontal linear cluster of ACOS B3.4 aerosol retrievals was eliminated in B3.5 because the prior was based on the MERRA climatology and not fixed at one value. This analysis does not eliminate the possibility that many of the retrieved optical depths in ACOS B3.5 are still staying too close to their prior, as in B3.4. The two vertical populations of low aerosol optical depths are also seen in this

plot because the same true optical depths are being used. Besides the change in retrieved aerosols, the ice and water clouds differ minimally compared to B3.4.

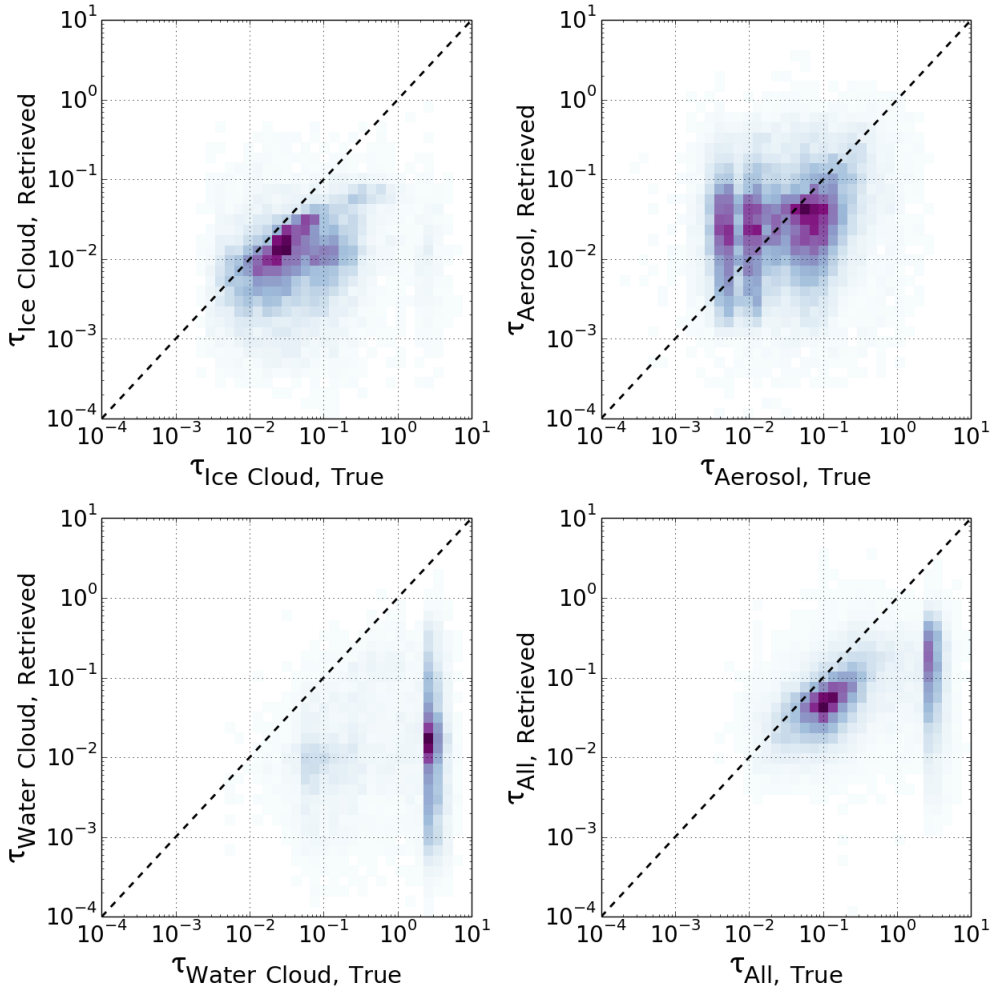

FIGURE 3.6. Heat map of the true optical depths compared to the retrieved ACOS B3.5 optical depths from OCO-2 simulations. Optical depths are compared for the ice cloud, the combined aerosol layer (two MERRA types), the water cloud, and the total combined aerosol layer.

In this section I have shown that the ACOS X_{CO_2} retrieval algorithm is only modestly able to retrieve cloud and aerosol optical depths. Individual retrieved components, such as water clouds, are especially uncorrelated with their true values.

3.3. Spatial Analysis

3.3.1. Dominant Aerosol Type. Besides validating retrieved aerosol optical depths against AERONET for real GOSAT data and true values for OCO-2 simulations, information about the global distribution of different aerosol types was computed to determine if there were regional biases or patterns in the retrievals. The retrievals were divided into a 7.5x7.5 degree grid and the "dominant" aerosol type for each grid cell was computed. The dominant aerosol type is the type which has the largest mean optical depth value for a given grid cell. This analysis was initially done on GOSAT ACOS B3.4 data, which contains four aerosol types: water cloud, ice cloud, Kahn 2b, and Kahn 3b. It was then done on GOSAT and OCO-2 ACOS B3.5 data which retrieves water cloud, ice cloud, and two MERRA aerosol types. Only four days of OCO-2 data were run so complete global coverage was lacking.

3.3.2. GOSAT Dominant Aerosol Type. The dominant retrieved aerosol type of each grid cell for the GOSAT ACOS B3.4 dataset is shown in figure 3.7. The water cloud type is dominant over most of the oceanic regions while the Kahn 3b type is the most dominant type over most of the land. Over the Sahara, however, the algorithm selected ice cloud as the most prominent aerosol type. This is likely because the ice type is similar to a dust particle: both are typically tens of μm in diameter. Interestingly, the Kahn 2b type is rarely selected as the most dominant aerosol. No data is present at higher latitudes in both hemispheres due to the geometric limitations of GOSAT. Gaps in north-central South America, central Africa, and southeast Asia are due to high levels of cloud contamination limiting the number of retrievals that make it past pre-filtering.

Next the dominant aerosol type for GOSAT ACOS B3.5 retrievals was calculated, shown in figure 3.8, to see if the patterns are similar to ACOS B3.4. Overall, the selection of

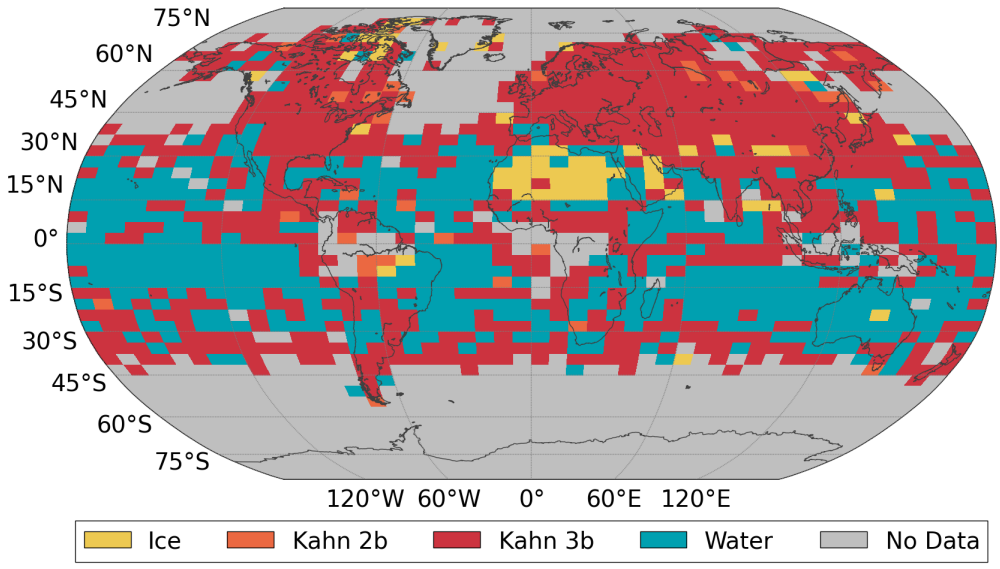

FIGURE 3.7. The dominant aerosol type selected by ACOS B3.4 for GOSAT data. Ice cloud is shown in yellow, Kahn 2b in orange, Kahn 3b in red, and water cloud in blue. Grid cells containing no valid GOSAT retrievals are shown in grey.

MERRA aerosol types seems realistic. The addition of a dust type (DU) has replaced the ice cloud type in ACOS B3.4 over the Sahara and other regions affected by deserts. Organic carbon (OC) seems to dominate over vegetation while sea salt (SS) is the primary type selected over much of the ocean instead of the water cloud type. Organic carbon over vegetative regions is logical because that type should be associated with biomass burning. Sulfate (SO) seems to have replaced the Kahn 3b type over land. Interestingly, black carbon (BC) is never the most dominant aerosol in a grid box.

Besides examining the overall dominant aerosol type, the secondary dominant ACOS B3.5 aerosol types were investigated. This refers to the second largest mean retrieved optical depth for each grid box. Figure 3.9 shows the second most dominant aerosol type. Interestingly, ice cloud is still frequently selected as a secondary aerosol over desert regions even though the retrieval is already typically fitting for a dominant dust type. Sea salt is either the dominant or second most dominant aerosol type selection over nearly all of the ocean while

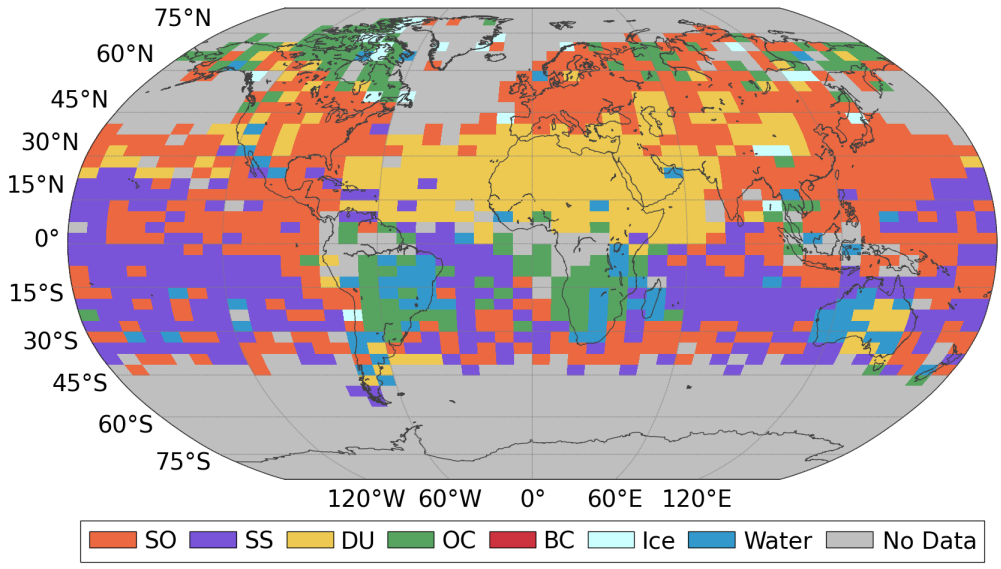

FIGURE 3.8. The dominant aerosol type selected by ACOS B3.5 for GOSAT data. Sulfate (SO) is shown in orange, sea salt (SS) in purple, dust (DU) in yellow, organic carbon (OC) in green, black carbon (BC) in red, ice cloud (Ice) in light blue, and water cloud (Water) in blue. Grid cells containing no valid GOSAT retrievals are shown in grey.

dust and sulfate combine to represent much of the land aerosols over North America, Asia, and Europe.

The dominant aerosol types looked quite realistic so the *a priori* aerosols were plotted (figure 3.10). The water cloud and ice cloud prior optical depth values are identical (0.0125) so they are plotted as one type (blue). This revealed that the ACOS B3.5 retrieval algorithm isn't changing much from the prior MERRA climatological aerosol information. E.g. dust dominating over the Sahara, sea salt over the oceans. Noticeable differences in the *a priori* plot and dominant plot include the retrieval trying to increase the amount of water cloud over vegetative regions and increase the amount of sulfate over oceans. This suggests that perhaps the constraints on optical depth could be loosened to allow the retrieval to deviate further from the prior information.

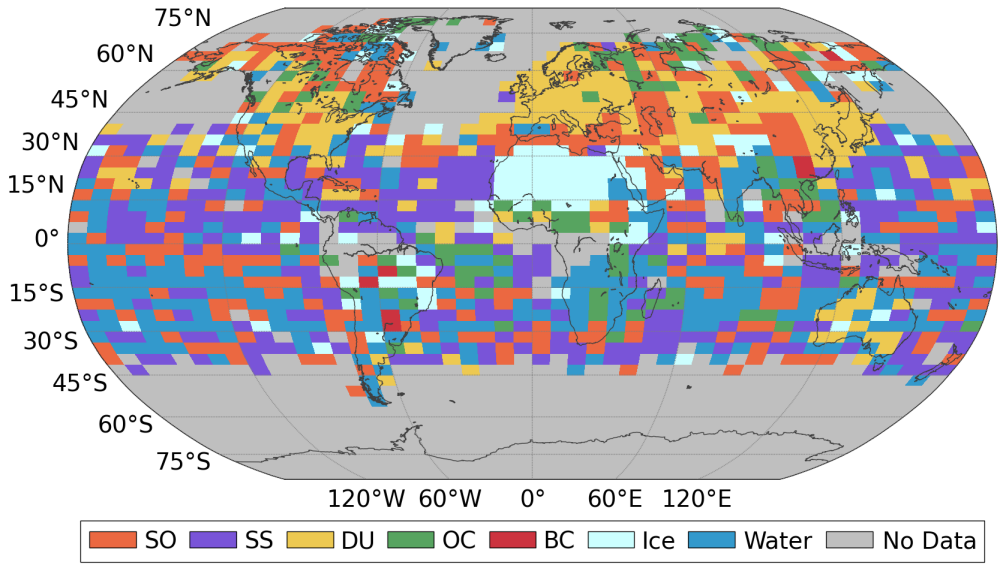

FIGURE 3.9. The secondary dominant aerosol type selected by ACOS B3.5 for GOSAT data. Sulfate (SO) is shown in orange, sea salt (SS) in purple, dust (DU) in yellow, organic carbon (OC) in green, black carbon (BC) in red, ice cloud (Ice) in light blue, and water cloud (Water) in blue. Grid cells containing no valid GOSAT retrievals are shown in grey.

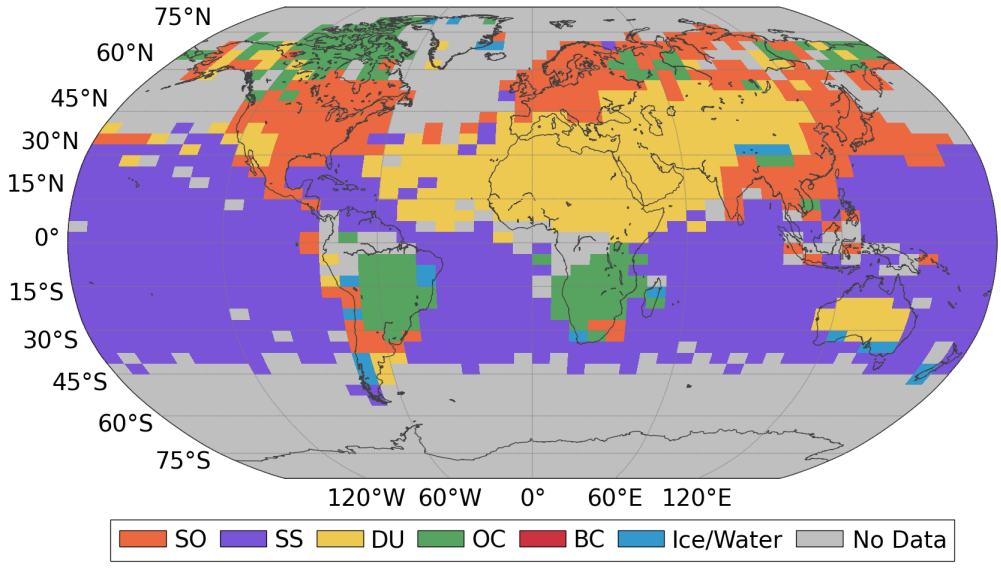

FIGURE 3.10. The *a priori* MERRA aerosol type used in the GOSAT retrievals. Sulfate (SO) is shown in orange, sea salt (SS) in purple, dust (DU) in yellow, organic carbon (OC) in green, black carbon (BC) in red, ice cloud and water cloud (Ice/Water) in blue. Grid cells containing no valid GOSAT retrievals are shown in grey.

3.3.3. OCO-2 Dominant Aerosol Type. Besides GOSAT retrievals, OCO-2 simulated retrievals were also examined to see if any regional trends were visible. The dominant aerosol type for ACOS B3.4 is shown in figure 3.11. Where as the GOSAT retrievals (figure 3.8) showed clear regional trends with logical placement of specific aerosol types, the pattern of dominant retrieved OCO-2 ACOS B3.4 aerosol type is less clear. As in GOSAT, Kahn 3b aerosols are often preferentially retrieved over land. Kahn 3b also seems to be favored over ice-covered land surfaces (Antarctica and Greenland). The ice cloud type is rarely retrieved over land (almost none in the Sahara) but rather scattered across the oceans along with water cloud and, to a lesser extent, the two Kahn aerosol types.

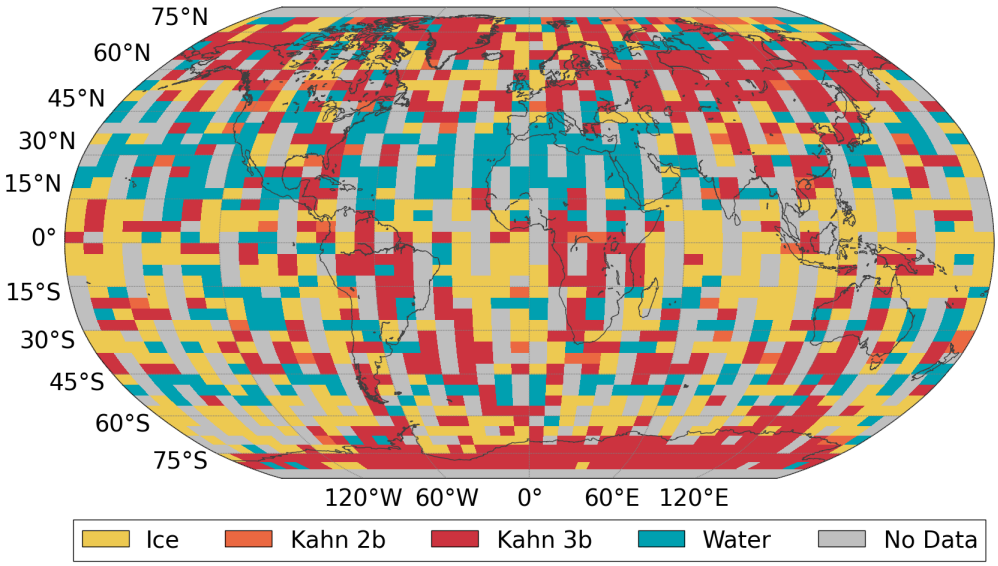

Figure 3.11. The dominant aerosol type selected by ACOS B3.4 for simulated OCO-2 data. Ice cloud is shown in yellow, Kahn 2b in orange, Kahn 3b in red, and water cloud in blue. Grid cells containing no valid OCO-2 retrievals are shown in grey.

To assess differences between the ACOS B3.4 and B3.5 aerosol parameterizations, B3.5 was run on the same four days of simulated OCO-2 data. The dominant aerosol is shown in figure 3.12. Compared to OCO-2 ACOS B3.4 aerosol patterns, B3.5 appears to be a significant improvement. Similarities to the real GOSAT retrievals exist including dust over

the Sahara and organic carbon over southern Africa, central South America, and northern North America. Differences include the algorithm retrieving more ice and less sulfate over the oceans. Interestingly, the OCO-2 simulations retrieve water cloud as the dominant type over the Antarctic but primarily dust over the Arctic. This appears to be an effect of land versus ocean surface parameterization. As previously stated, only having four days of simulated data prevented full global coverage, but general patterns are still resolved.

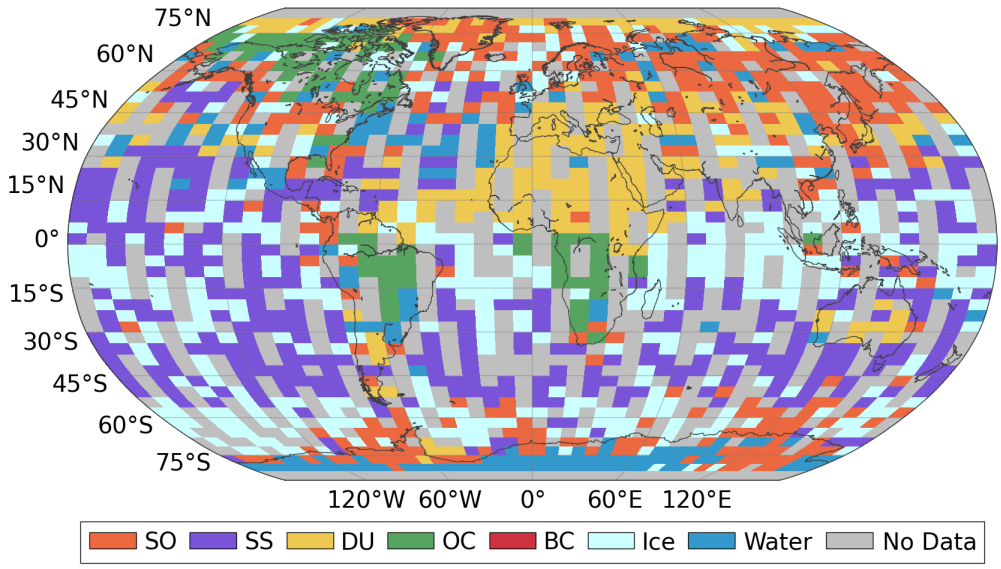

FIGURE 3.12. The dominant MERRA aerosol type selected by ACOS B3.5 for OCO-2 data. Sulfate (SO) is shown in orange, sea salt (SS) in purple, dust (DU) in yellow, organic carbon (OC) in green, black carbon (BC) in red, ice cloud (Ice) in light blue, and water cloud (Water) in blue. Grid cells containing no valid OCO-2 retrievals are shown in grey.

The GOSAT ACOS B3.5 aerosols were shown to not deviate much from the MERRA prior aerosol information so naturally this was checked in the OCO-2 ACOS B3.5 simulations. Because OCO-2 has a higher signal to noise ratio, it's hypothesized that more deviations from the prior may occur compared to GOSAT retrievals. Figure 3.13 shows the prior dominant aerosol type. As hypothesized, the dominant OCO-2 prior types mostly match the GOSAT prior types. This is expected because they both draw their prior information from the same

MERRA climatology dataset. Because OCO-2 has a larger latitudinal range than GOSAT, it is revealed that sea salt is used as the prior for the entire southern ocean while the ice/water cloud prior is larger than any of the MERRA aerosol priors over Antarctica. Comparing the prior OCO-2 aerosols to the retrieved aerosols reveals that the simulations tend to vary more from the prior than in real GOSAT retrievals. Ice is increased significantly over oceans and water cloud and sulfate are more prevalent across the globe than in the prior. Dust and organic carbon tend to stay dominant wherever they are placed in the prior, which suggests that the prior is perhaps too tightly constrained or simply that the prior type is properly chosen.

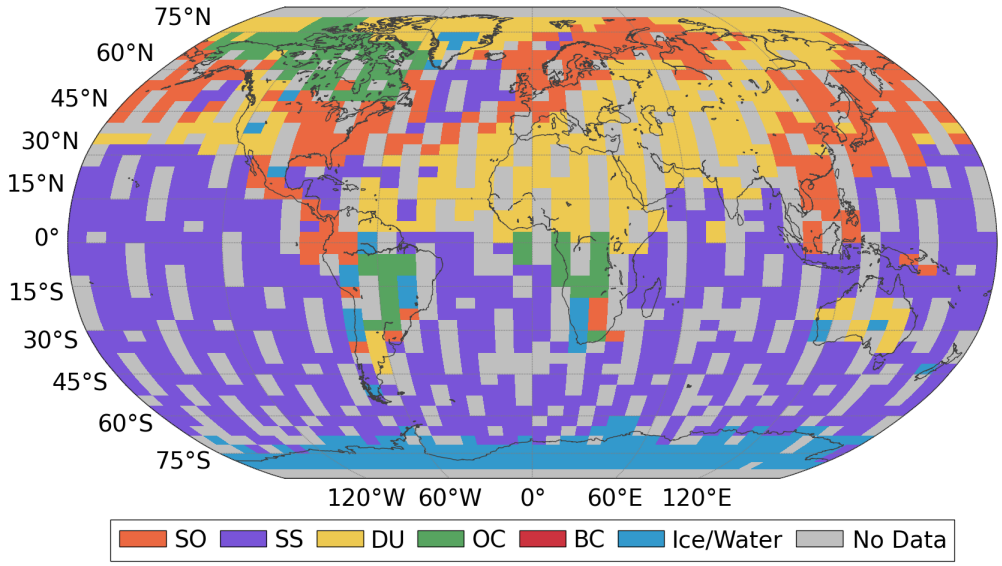

FIGURE 3.13. The *a priori* MERRA aerosol type used in the OCO-2 simulations. Sulfate (SO) is shown in orange, sea salt (SS) in purple, dust (DU) in yellow, organic carbon (OC) in green, black carbon (BC) in red, ice and water cloud (Ice/Water) in blue. Grid cells containing no valid OCO-2 retrievals are shown in grey.

With OCO-2 simulations, unlike real GOSAT data, the true aerosol type is known. The dominant CALIOP type used in the simulations is shown in figure 3.14. Water cloud tends to dominate much of the globe, only interrupted by some dusty land regions, clean marine ocean

regions, and some small patches of other types. Many of these water clouds are at low levels and thus managed to pass the O_2 A-band cloud screener (section 2.1.1). Comparing the true CALIOP aerosol type to the dominant retrieved type in OCO-2 ACOS B3.5 (figure 3.12) simulations reveals that, as is so often the case, the Saharan dust feature is correctly resolved. The retrieval algorithm tends to swap water cloud for various other types across much of the globe. Over ocean, for example, water cloud is primarily replaced by ice clouds and sea salt. The "smoke" region in southern Africa appears to have been replaced by organic carbon, which is logical because these types roughly correspond in terms of their properties.

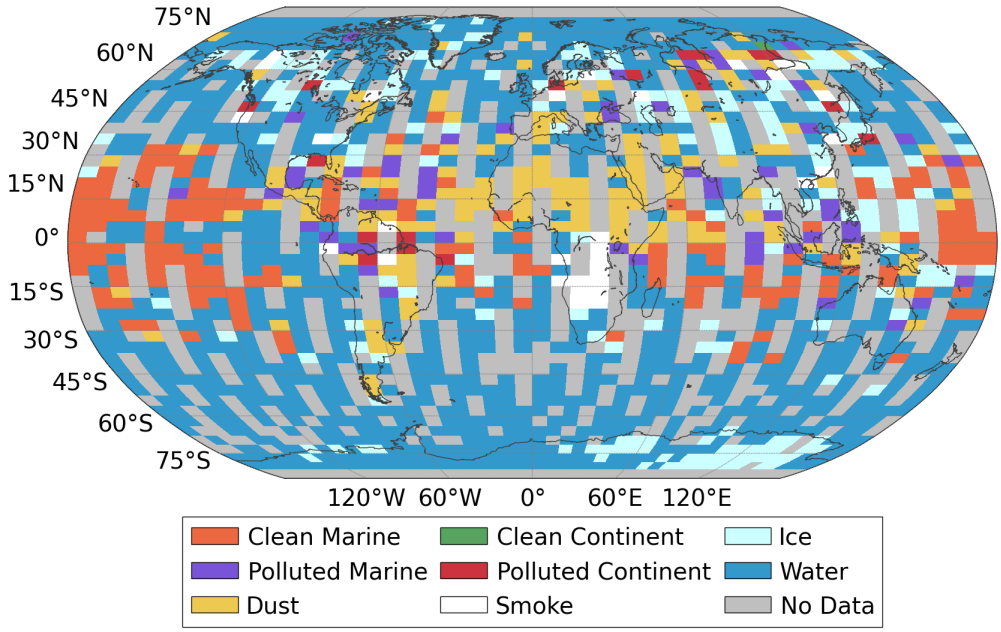

FIGURE 3.14. The dominant CALIOP aerosol type used in the OCO-2 simulations. Clean marine is shown in orange, polluted marine in purple, dust in yellow, clean continent in green, polluted continent in red, smoke in white, ice cloud in light blue, and water cloud in blue. Grid cells containing no valid OCO-2 retrievals are shown in grey.

Comparing the dominant CALIOP type to the dominant *a priori* MERRA type reveals little correlation except for a dusty northern Africa. While sea salt is the primary type

chosen over oceans for the *a priori*, water cloud is dominant for CALIOP. This comparison is difficult because of the different aerosol types used in the CALIOP and MERRA products.

These comparisons of dominant GOSAT and OCO-2 aerosols suggest that there is still room for improvement in terms of selecting appropriate prior aerosol information for ACOS retrievals.

3.3.4. OCO-2 Aerosol Optical Depth Error Spatial Analysis. To determine if the aerosol optical depth retrievals improved from ACOS B3.4 to B3.5, a spatial analysis of the difference between the two versions for OCO-2 simulations is shown in figure 3.15, where the total aerosol optical depth is the sum of the water cloud, ice cloud, and two aerosol type optical depths. The error calculated for each build is the retrieved total optical depth minus the true optical depth; the difference in the error is the absolute value of the ACOS B3.5 error minus the absolute value of the B3.4 error. Thus, a negative value means an improvement in the retrieved optical depth magnitude and a positive value means a worsening.

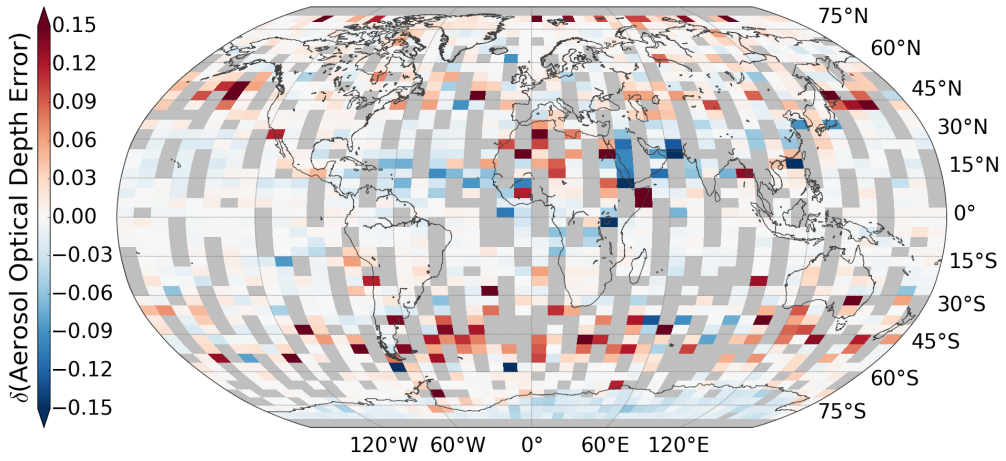

Figure 3.15. The difference in the magnitude of the retrieved optical depth errors between OCO-2 simulated retrievals using ACOS B3.4 and ACOS B3.5. Negative values (blue) indicate improvement while positive values (red) indicate worsening. Grid cells containing no valid OCO-2 retrievals are shown in grey.

Overall there appears to be a significant amount of scatter with some potential regional patterns. The optical depth retrievals appear to have worsened in Northern Africa, where the aerosol type was changed from water cloud in ACOS B3.4 to dust in B3.5. The Southern Ocean seems to also have worsened but there is no clearly dominant aerosol type in either B3.4 or B3.5 that is to blame. The most obvious area of improvement is the Middle East, where water cloud was changed to dust. This trend conflicts with the worsening over the Sahara and suggests that the dominant aerosol type alone is not responsible for increases or decreases in the retrieved optical depth error.

3.4. Aerosol Heights

Besides the optical depths of the aerosol types, the peak heights were also examined to see if the algorithm was accurately placing the aerosol layers and to assess the choice of prior height information. ACOS B3.5 was also examined to see if it was better at placing the aerosol layers than B3.4. This analysis was done because small changes in the location of the aerosol layers can have a significant impact on the light path length which impacts the retrieved X_{CO_2}. The Gaussian distribution of the aerosol layers was often centered near the surface, so roughly half of the Gaussian curve was actually above the surface. Thus, the "half height" of each retrieved aerosol layer was instead analyzed. This is the level at which half of the area under the Gaussian curve is below and half is above. The half height of the aerosol profiles that were ingested into the OCO-2 simulations were calculated and compared against the retrieved aerosol heights.

Figure 3.16 shows a comparison of the OCO-2 ACOS B3.4 retrieved ice height, aerosol height (height of the combination of the two Kahn types), water cloud height, and total height (height of the combination of all four types) compared to their true heights over

ocean surfaces. It's clear that the retrieval is placing both the aerosol and water cloud layers too high relative to their true heights. The algorithm tends to place all the aerosol layers at approximately the same pressure level which happens to be near the prior height of ∼880mb. The water cloud is initially placed at its prior of roughly 750mb and it is consistently pushed down by the retrieval algorithm. Often times the algorithm is able to place the water cloud layer near the surface, which is typically its true height. However, it is obvious that many times the algorithm is only able to move the layer part of the way and thus results in an over estimation of the water cloud layer's height. The ice height is relatively well placed over ocean, but occasionally too low in the atmosphere. This indicates that perhaps the prior Gaussian width is too large; a narrower aerosol layer would have more freedom to move vertically. These small changes in aerosol layer height can potentially have significant impacts on the light path and thus the final retrieved X_{CO_2}, therefore it's important to choose the prior and its uncertainty wisely.

The priori half height of the two aerosol layers was changed from ∼880mb in ACOS B3.4 to roughly 830mb in B3.5. The new B3.5 heights over ocean are shown in figure 3.17 compared to their true values. Interestingly, despite the prior being raised from B3.4 to B3.5, the retrieval is able to place the aerosol layers much closer to their true values near the surface. This is evidence that the ACOS B3.5 retrieval algorithm aerosol parameterization is an improvement on ACOS B3.4, at least in terms of its ability to move aerosol layers around. The likely cause of this is the reduced Gaussian width of the aerosol layers in ACOS B3.5 which increased the sensitivity of the retrieval to the layer's width. This allows the algorithm to more freely move the layer vertically up and down. The water cloud heights are also somewhat shifted down, but less significantly than the aerosol layers.

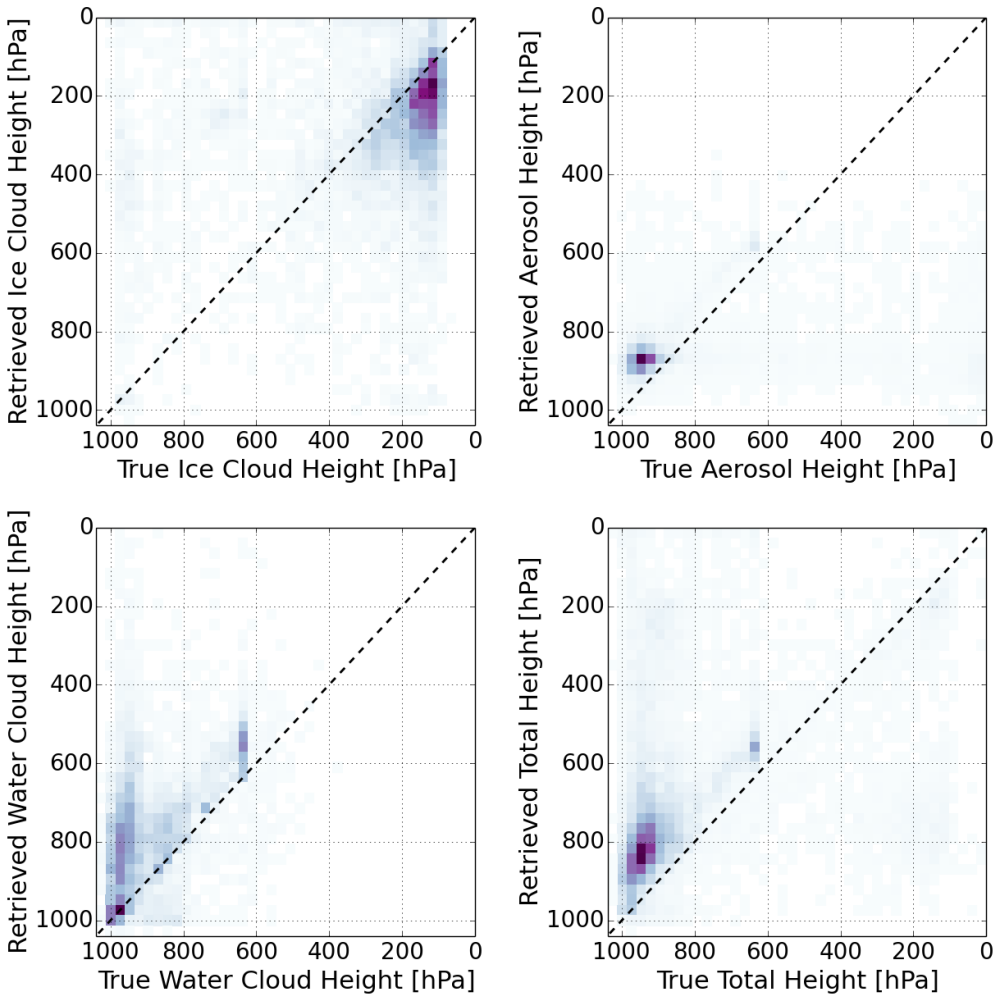

FIGURE 3.16. True aerosol heights compared to retrieved aerosol heights over ocean for OCO-2 ACOS B3.4 data. Layer heights are compared for the ice cloud, the combined Kahn 2b and Kahn 3b aerosol layer, the water cloud, and the total combined aerosol layer.

Over land, the changes from ACOS B3.4 to B3.5 were less significant. As over the ocean, the retrieved aerosol layer was improved by being placed lower in the atmosphere. An interesting feature over land, shown in figure 3.18, is the retrieval's inability to accurately place the ice cloud layer. Over ocean (figures 3.16 and 3.17), the ice cloud is relatively well placed but over land the retrieval consistently places the ice cloud far too high compared to its true location in the atmosphere. This ice cloud height problem overland is a feature of both ACOS B3.4 and B3.5 (only B3.5 is shown). Besides misplacing the ice cloud, there is

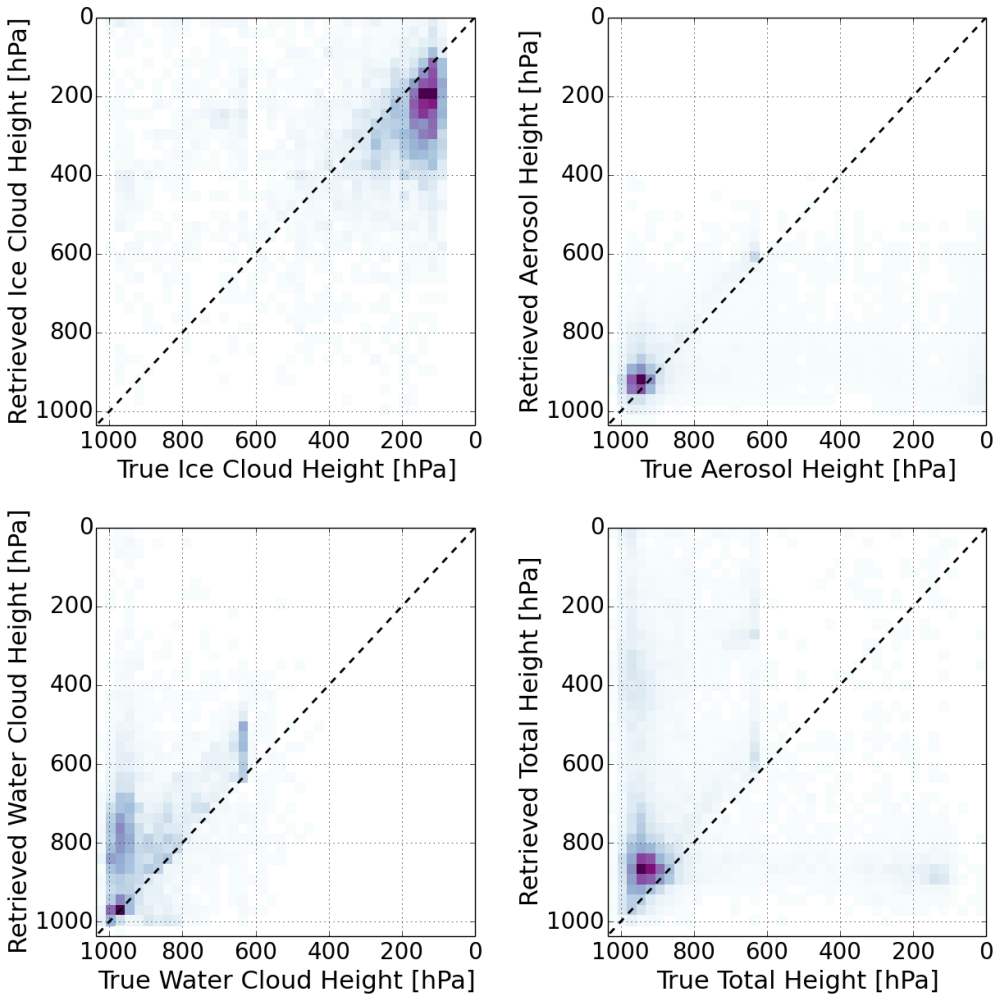

FIGURE 3.17. Heat map of true aerosol heights compared to retrieved aerosol heights over ocean for OCO-2 ACOS B3.5 data. Layer heights are compared for the ice cloud, the combined two MERRA aerosol layer, the water cloud, and the total combined aerosol layer.

a population of high, thin aerosols that the algorithm consistently puts too low. Overall, however, the total aerosol layer over land is usually near the 1-to-1 line. This is because the optical depth of the erroneously placed ice clouds doesn't contribute much to the total optical depth.

The retrieved OCO-2 simulation full physics heights were also compared against X_{CO_2} errors to determine if biases were present. Figure 3.19 shows retrievals over land. The retrievals were filtered by the genetic algorithm to keep the best 60% of the data (see section 2.3).

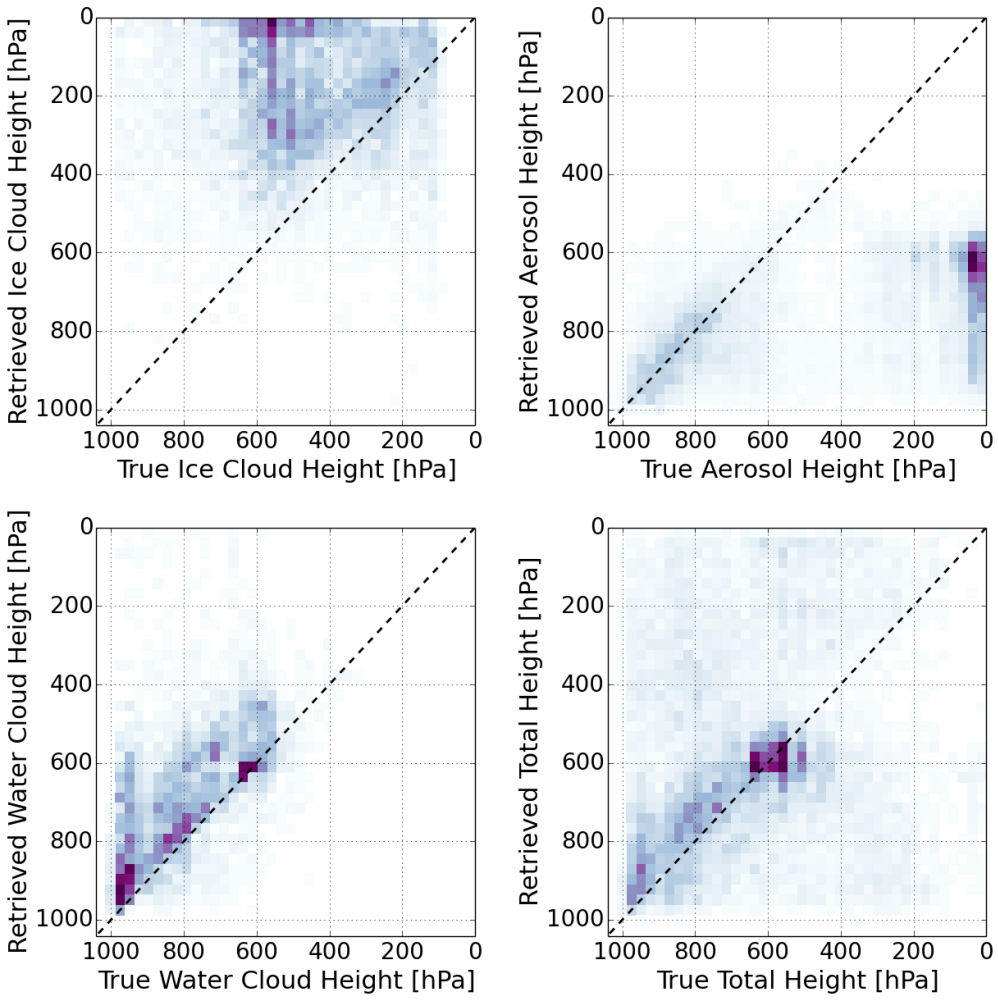

FIGURE 3.18. Heat map of true aerosol heights compared to retrieved aerosol heights over land for OCO-2 ACOS B3.5 data. Layer heights are compared for the ice cloud, the combined two MERRA aerosol layer, the water cloud, and the total combined aerosol layer.

It was found that there was no significant correlation with any of the aerosol heights and the X_{CO_2} error. This was seen in ocean data as well (not shown). This suggests that the placement of the aerosol layers does not directly result in a bias in the final X_{CO_2} values.

3.5. Aerosol Comparison Summary

In this chapter it was demonstrated that the ACOS X_{CO_2} full physics retrieval algorithm has difficultly when it comes to gaining information about clouds and aerosols. The correlation between the retrieved GOSAT aerosol optical depths and AERONET aerosol

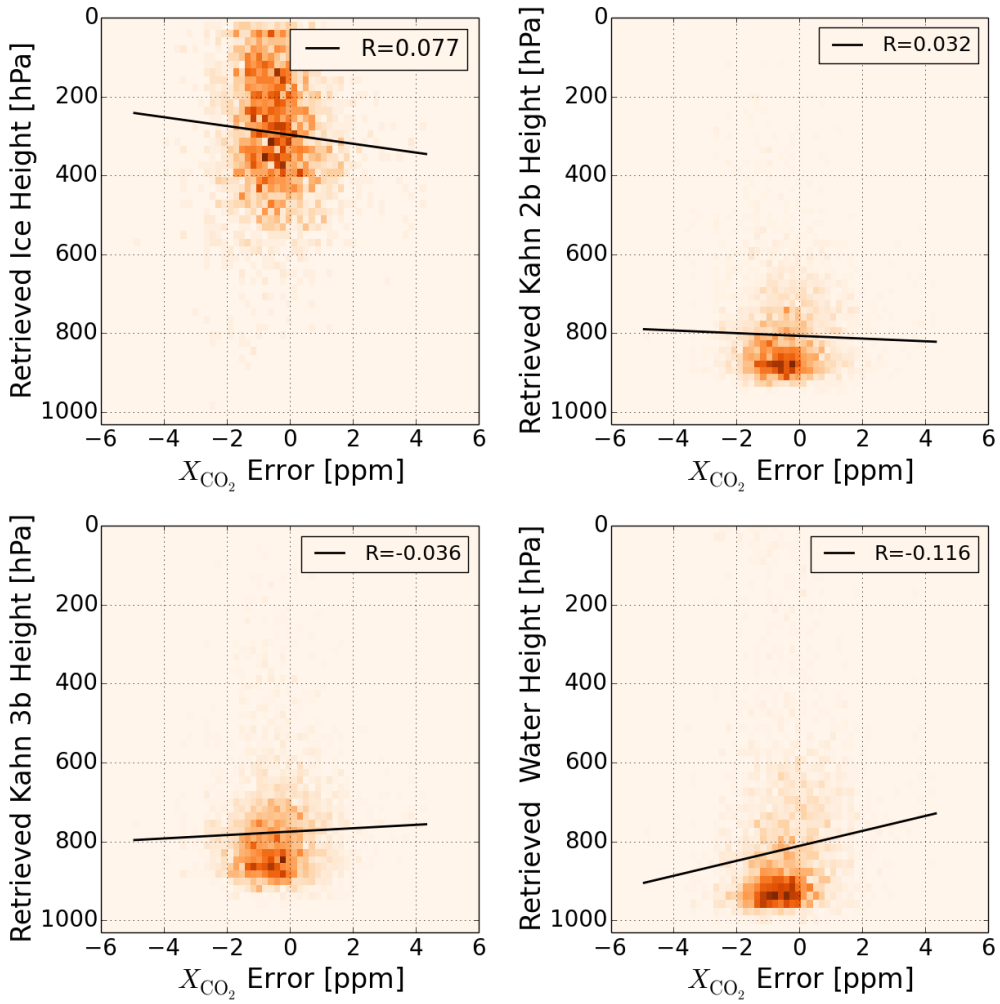

FIGURE 3.19. Heat map of X_{CO_2} error compared to aerosol heights over land for OCO-2 ACOS B3.4 data. The dataset was filtered to a throughput of 60% to remove outliers. From left to right, X_{CO_2} error is compared to the ice cloud height, Kahn 2b height, Kahn 3b height, and water cloud height.

optical depths was poor for older versions of ACOS and only improved slightly with the updated builds. There was moderate correlation between the retrieved OCO-2 simulation total optical depths and the scene's true total optical depths. However, the algorithm had difficulty retrieving information about individual aerosol types, such as water clouds located near the surface. Examining the dominant aerosol types for both GOSAT and OCO-2 retrievals revealed that the selected aerosol types seem realistic but don't vary much from the prior MERRA types. The retrieval algorithm, in general, does moderately well at placing

the sum of the aerosol layers at the correct height for OCO-2 simulations. For individual aerosol types, however, it again has difficulty properly retrieving the height of each aerosol layer. Overall, this chapter demonstrated that the ACOS X_{CO_2} retrieval algorithm is somewhat able to place aerosol layers but is unable to properly retrieve the amounts, especially for individual aerosol types. These results motivated the investigation of the algorithm's inability to accurately retrieve aerosol information and to see if it is negatively impacting the retrieved X_{CO_2} values.

CHAPTER 4

X_{CO_2} Retrieval First Guess Sensitivity

Thus far it has been shown that ignoring clouds and aerosols is not effective in reducing X_{CO_2} errors and that the ACOS X_{CO_2} retrieval algorithm generally has difficulty gaining information about clouds and aerosols. This provided motivation to further study the algorithm's aerosol parameterization. This chapter presents an examination of whether or not nonlinearity in the forward model could potentially cause significant errors in the retrieval of aerosols and X_{CO_2} values.

Optimal estimation, as described in section 1.2.1, uses a state vector of parameters to try and match measured radiances by inputing them through a forward model then trying to minimize χ^2. If the forward model is linear, the solution will always be the same if given enough iterations to find the χ^2 minimum. This is because for a linear problem the χ^2 minimum is a Gaussian in n-dimensional space, where n is the number of elements in the state vector, and thus there is a single minimum value of χ^2 and a single optimal solution for the state vector. If the forward model is nonlinear, however, there may exist multiple χ^2 minima or a very broad range of low χ^2 values. That is, the same state vector can result in multiple, equally valid solutions. This causes the final solution to be dependent on where one begins searching χ^2 space, i.e. the "first guess". Further, posterior error estimates may be significantly underestimated due to this dependency because the posterior error calculation assumes a linear model near the final retrieved solution (details on the posterior error calculation are given in Connor et al. (2008)). One method of testing a retrieval algorithm's sensitivity to the first guess is to modify the first guess while keeping

the *a priori* state vector the same. This ensures the cost function remains constant and therefore that the minimum (or minima) in χ^2 space is unchanged.

It has been shown that only about 1-5 pieces of aerosol information can be retrieved from GOSAT and OCO-2 measurements (Frankenberg et al., 2012). However, the ACOS X_{CO_2} retrieval algorithm attempts to retrieved eight aerosol parameters (the height and amount of four types). This suggests there may be multiple, equally valid solutions to those eight parameters which could significantly impact the final measured X_{CO_2}. Because ACOS B3.4 retrieval algorithm contains 45 parameters in the state vector, χ^2 cannot simply be calculated for all first guesses, plotted, and visually inspected to determine whether or not the algorithm is linear.

The sensitivity of the ACOS X_{CO_2} retrieval algorithm to the first guess of its aerosol parameters was tested using OCO-2 simulations. The eight aerosol parameters selected to be perturbed were the amount (optical depth in natural log-space) and peak height of the four types. This analysis was done on ACOS B3.4 to avoid the complexity of using variable MERRA aerosol optical depth priors. Thus, the four types were the water cloud, ice cloud, Kahn 2b aerosol, and Kahn 3b aerosol. It has been shown that the ACOS X_{CO_2} retrieval algorithm is not sensitive to changing the width of the aerosol layer so all four aerosol Gaussian widths were, as they are in the standard ACOS retrieval, kept approximately constant. The different first guesses were selected by perturbing each parameter by some random value chosen along a Gaussian in natural log-space described by a peak at the *a priori* value and a width corresponding to the parameter's prior uncertainty. 1,000 values were randomly selected for all eight aerosol parameters. An example of the distribution of new first guesses for an optical depth with a prior of 0.0125 is shown in figure 4.1.

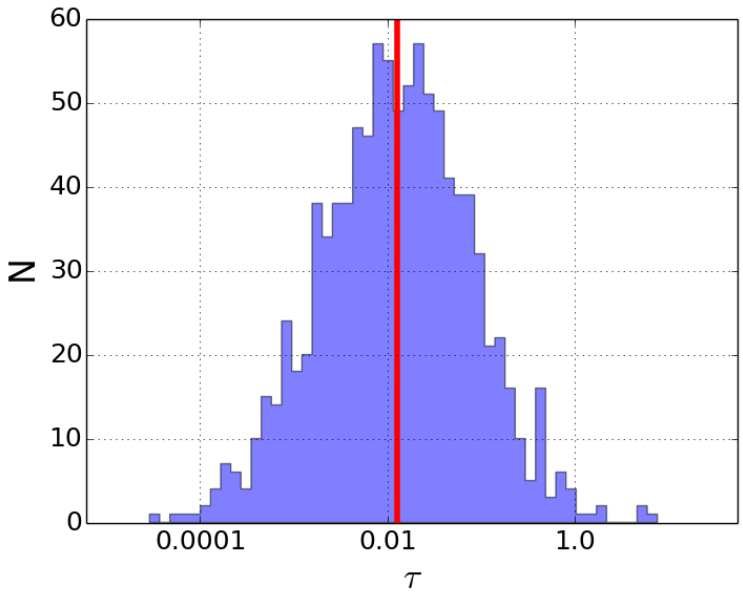

FIGURE 4.1. An example of the Gaussian distribution of first guesses around the prior aerosol optical depth (red line). 1,000 randomly selected values were used.

Twelve unique cases were analyzed, described in table 4.1. This was to examine the extremes of what OCO-2 can measure in terms of surface type, optical depth, solar zenith angle, albedo, and wind speed to try and deduce what type of scenes the retrieval algorithm is most sensitive to. These cases passed all pre-filtering tests including the O_2 A-band cloud screener so that no scenes with detectable thick cloud or aerosol layers were present.

To try and get a glimpse of the nonlinearity in χ^2 space, further tests were done where only two parameters' first guesses were perturbed. The perturbations were linearly distributed around the prior in order to try and map out χ^2 space. It was hypothesized that perhaps there would be obvious χ^2 maxima and minima, but because the cost function is of a 45-dimension state vector there may not be any logical pattern visible in 2-dimensional space. The sole test done was to perturb the first guess of X_{CO_2} and the Kahn 2b optical depth. For this single case the Kahn 2b type was selected because it contained a few outliers clustered near the true aerosol optical depth value so it was hypothesized that this feature would

TABLE 4.1. Twelve cases used for testing aerosol parameterization first guess sensitivity in OCO-2 ACOS B3.4 simulations and their corresponding scene descriptions. The scene characteristics varied include the solar zenith angle (SZA; low or high), surface albedo (low or high), surface type (land or ocean), wind speed (low or high), and optical depth (low or high).

Case	Surface	SZA	Reflectivity	Wind Speed	Optical Depth
1	Land	Low	High	-	Low
2	Land	Low	High	-	High
3	Land	Low	Low	-	Low
4	Land	Low	Low	-	High
5	Land	High	High	-	Low
6	Land	High	High	-	High
7	Land	High	Low	-	Low
8	Land	High	Low	-	High
9	Ocean	-	-	Low	Low
10	Ocean	-	-	High	Low
11	Ocean	-	-	Low	High
12	Ocean	-	-	High	High

be visible in χ^2 space. The Kahn 2b optical depth first guesses were perturbed linearly in natural log-space while the X_{CO_2} first guess values were perturbed linearly but with the CO_2 profiles in agreement with the CO_2 *a priori* covariance matrix (S). Eigenvalue decomposition is first used to decompose S into two matrices, P and D:

$$S = PDP^T \tag{4.1}$$

where P is an 20x20 matrix whose columns are the eigenvectors of S while D is a diagonal matrix containing the corresponding eigenvalues (λ). P can also be referred to as the rotation matrix. 20 independent Gaussian random numbers with a mean of zero and a standard deviation of one were then generated and multiplied by their respective $\sqrt{\lambda}$ to obtain the vector $\vec{r}$. The perturbed CO_2 profile, $\vec{c}$, was then found by changing the newly

created vector $\vec{r}$ back into regular coordinates and adding it to the *a priori* CO_2 profile ($\vec{c}_{prior}$).

$$\vec{c} = P^T \vec{r} + \vec{c}_{prior} \tag{4.2}$$

This procedure ensures that the random X_{CO_2} values were calculated from CO_2 profiles obeying their *a priori* covariance matrix, i.e. it generates CO_2 perturbations and their corresponding X_{CO_2} values that are consistent with the assumed *a priori* covariance. In order to obtain a linear distribution of X_{CO_2} values, many perturbed CO_2 profiles were generated and an approximately linear sample of X_{CO_2} values were chosen using binning and then implemented in first guess sensitivity testing.

4.1. Aerosol Parameter Perturbation

The twelve cases chosen to test first guess sensitivity are shown in figure 4.2. The results are highly variable, which would not occur if the model was perfectly linear and every case simply converged to a single global χ^2 minimum. The grey bars represent the distribution of retrieved X_{CO_2} values from all 1,000 aerosol first guess perturbations. The solid green line is the true X_{CO_2} used in each simulation. The solid purple line is the "standard" X_{CO_2} retrieved when the L2 code is run normally using the prior aerosol heights and amounts as the first guess. The retrieved uncertainty of the standard X_{CO_2} is shown by the dashed purple line.

In most of the cases the standard retrieved X_{CO_2} (solid purple line) is close to the peak in the distribution of 1,000 X_{CO_2} values retrieved using variable first guesses (grey bars). This was somewhat expected because the perturbations were distributed normally about the prior

so it's encouraging that the X_{CO_2} resulting from using the prior as the first guess lies in the middle of the distribution. However, certain cases have their peak distribution offset from the standard retrieved X_{CO_2}. Case 6, for example, has a standard X_{CO_2} of ∼393.9 ppm but the distribution has a distinct and thin peak approximately 0.2ppm higher at ∼394.1 ppm. Other cases with obvious offsets include cases 1, 3, and 12. Other times the distribution does not have an obvious peak in the retrieved X_{CO_2}. Case 7, for example, appears to contain multiple maxima and the standard X_{CO_2} lines up with the peak at ∼392.0 ppm.

Certain cases demonstrate the ability of the retrieval algorithm to continuously converge to nearly the same X_{CO_2} value, despite significant perturbations to the aerosol first guesses. This provides evidence that the retrieval's forward model can be at least somewhat linear in certain cases. In case 10, for example, almost all the first guess retrievals align closely with the standard X_{CO_2} value. Other cases, however, suggest nonlinearity in the algorithm because they fail to converge to a single solution and the range of X_{CO_2} values retrieved for the first guess runs is large and often surpasses the posterior error estimation. As seen in case 1, some retrievals have a spread of multiple ppm and often include outliers that vary even more significantly. Despite having a peak in the first guess distribution, the range of retrieved values can still be on the order of several ppm. Case 2 is another example of this problem, where the first guess runs are semi-evenly distributed over a range of 5 ppm from ∼390 to ∼395 ppm. Considering the goal of OCO-2 is to constrain X_{CO_2} precision to within roughly 2.0 ppm (Miller et al., 2007), these results suggest that the retrieval is too sensitive to the first guess of the aerosol parameters.

What is actually desired, of course, is that the true X_{CO_2} value be located well within the uncertainty bounds of the standard X_{CO_2}. Case 10 and case 4 are excellent examples of this occurring. Case 4's standard X_{CO_2} retrieval almost retrieves the true X_{CO_2}, and the first

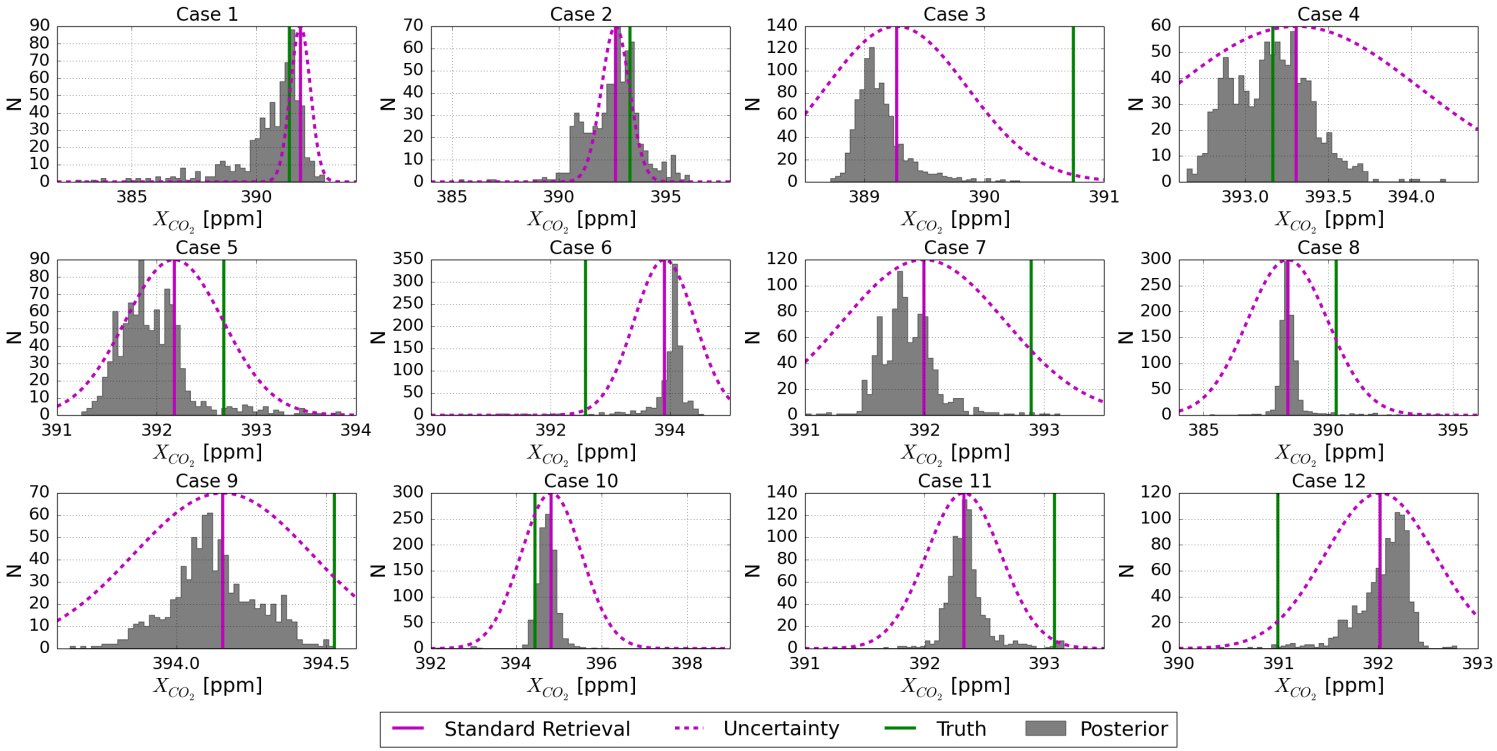

FIGURE 4.2. Twelve cases (described in table 4.1) of the retrieved X_{CO_2} distribution resulting from perturbing the first guess of the height and amount of the water cloud, ice cloud, Kahn 2b, and Kahn3b aerosol layers. The true X_{CO_2} is shown by the solid green line. The retrieved X_{CO_2} using the standard prior heights and amounts of all four aerosol types is shown by the solid purple line. The retrieved posterior uncertainty of the standard X_{CO_2} is shown by the dashed purple line. Note the variable x-axis range.

guess tests are roughly normally distributed around the true X_{CO_2} value with the maximum errors only being a few tenths of a part per million. Case 10's true X_{CO_2} is also well within the uncertainty of the standard X_{CO_2} retrieval and coincides nicely with the distribution of first guess runs. Other runs are less promising. Case 6's true X_{CO_2} value is at the far left fringe of the uncertainty of the standard X_{CO_2} as well as the likely uncertainty curves of the majority of the first guess X_{CO_2} values. This indicates that the uncertainty calculated for the standard X_{CO_2} is too small.

An interesting result is case 11. The majority of first guess X_{CO_2} values align with the standard X_{CO_2} at around 392.3 ppm and the true value is essentially outside the uncertainty bounds, which is obviously problematic. However, there is a small population of perturbed runs that manage to find the true X_{CO_2} of $\sim$393.1 ppm. This is highly suggestive of non-linearity in the retrieval algorithm in that there are multiple χ^2 minima that the algorithm can eventually converge upon: one primary minimum at $\sim$392.3 ppm and another minimum at $\sim$393.1 ppm. This confirms the hypothesis that the ACOS X_{CO_2} retrieval algorithm can behave in a nonlinear manner and that the final X_{CO_2} is often highly sensitive to the first guess of the aerosol parameters.

Case 6, as described above, is one where the majority of first guess runs end up close to the standard X_{CO_2} retrieval but far from the true X_{CO_2}. A few results, however, managed to retrieve a lower X_{CO_2} much closer to the true value. Case 6 contained a high true aerosol optical depth, which was not detected by the O_2 A-band cloud screener because it was very near the surface, and further investigation revealed that these few promising results were unique in that they managed to approximately retrieve the high aerosol optical depth. Figure 4.3 shows that the majority of the retrievals decided that there was essentially no aerosol present in the scene. However, a few retrievals, corresponding to the less erroneous

X_{CO_2} values, did manage to retrieve the thick aerosol layer. This suggests there are two somewhat distinct minima in χ^2 space: one with low aerosol optical depths and an erroneous X_{CO_2} and another with a much higher aerosol optical depth and a more accurate X_{CO_2}.

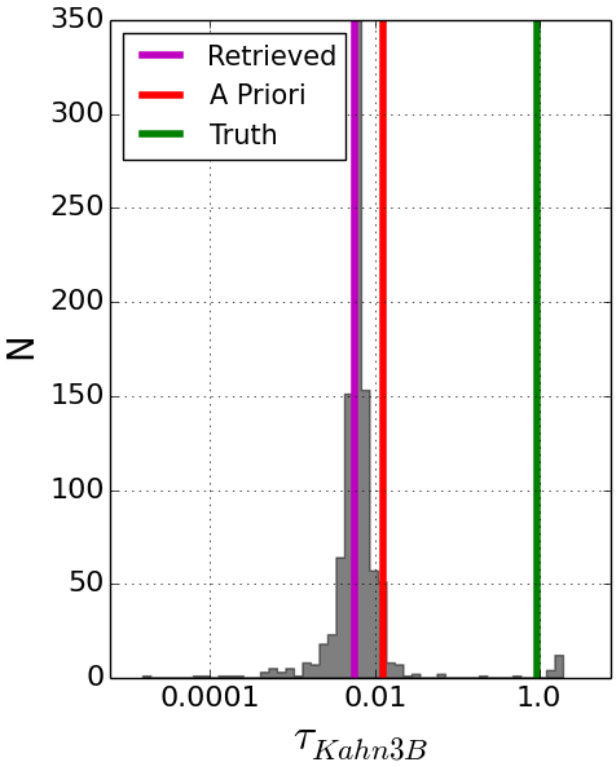

FIGURE 4.3. Case 6 Kahn 3b optical depths. The final retrieved Kahn 3b optical depths are shown in grey. The prior Kahn 3b optical depth is the red line, the true aerosol optical depth the green line, and the standard retrieved Kahn 3b optical depth the purple line.

Figure 4.4 demonstrates this in another way. A second, much smaller population of case 6 retrievals exists at high aerosol optical depths and ~392 ppm (with a few at slightly lower ppm values). This population is much closer to the true X_{CO_2} value (392.6 ppm) than the main population at around 394 ppm. Interestingly, there appear to be other locations at low X_{CO_2} and low optical depths where the algorithm was able to minimize the cost function. This further suggests complex nonlinearity and the potential for multiple solutions in the retrieval. The two main populations have the lowest χ^2 values, which suggests that the

retrieval algorithm thinks they're both equally valid solutions. The outliers tend to have larger χ^2 values which is indicative of a worse fit.

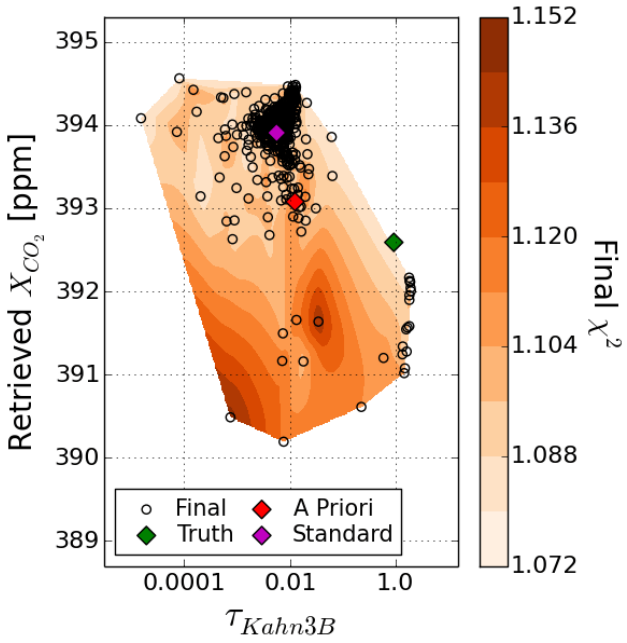

FIGURE 4.4. Case 6 Kahn 3b optical depths compared to the retrieved X_{CO_2} values. The χ^2 values of the final state of the forward model are shown in orange shading. The final values are shown in black. The prior Kahn 3b value and prior X_{CO_2} is shown by the red diamond. The true Kahn 3b optical depth and corresponding true X_{CO_2} is shown by the green diamond. The standard retrieved Kahn 3b optical depth and corresponding X_{CO_2} is shown by the purple diamond.

Other features discovered include bimodal distributions of the final retrieved aerosol parameters. Figure 4.5 shows case 12 where the algorithm retrieves two populations of Kahn 3b optical depth, one at ∼0.005 and another at ∼0.060. This is the difference between an extremely clear scene and a slightly contaminated scene. Interestingly, the standard retrieval lies in the middle of these two populations at ∼0.014, which is very close to the prior. This suggests that the standard retrieval is an anomaly and that the algorithm typically converges to either smaller or larger values of the Kahn 3b optical depth.

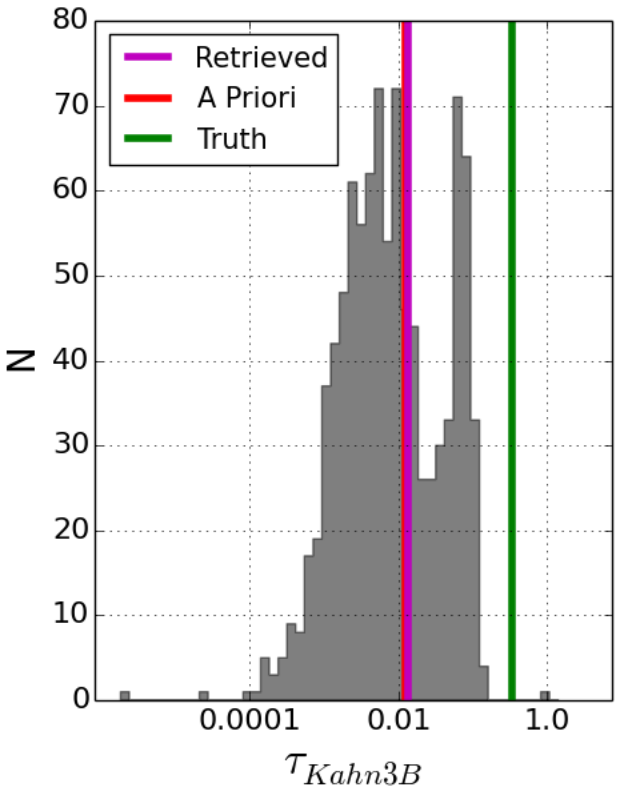

FIGURE 4.5. Case 12 Kahn 3b optical depths. The final retrieved Kahn 3b optical depths are shown in grey. The prior Kahn 3b optical depth is the red line, the true aerosol optical depth the green line, and the standard retrieved Kahn 3b optical depth the purple line.

The retrieved X_{CO_2} distribution for case 12, shown in figure 4.2, is, interestingly, not bi-modal but roughly normal with only a few outliers. Thus, the bi-modal distribution of Kahn 3b optical depths is likely compensated elsewhere to produce a semi-normal distribution of X_{CO_2} values. However, this distribution is still biased relative to the true X_{CO_2}.

4.2. Two Parameter Perturbation

Case 6 was selected to investigate further because of its interesting distribution of retrieved X_{CO_2} values, as seen in figure 4.4. To simplify the analysis, only two parameters' first guesses were perturbed instead of eight. Linearly perturbing the X_{CO_2} and Kahn 2b optical depth first guesses resulted in the final values shown in figure 4.6. The sparsity of

first guess and final X_{CO_2} values at high Kahn 2b optical depths is because many of those retrievals failed to converge. This was expected because the retrieval algorithm has difficulty with thick aerosol and cloud scenes.

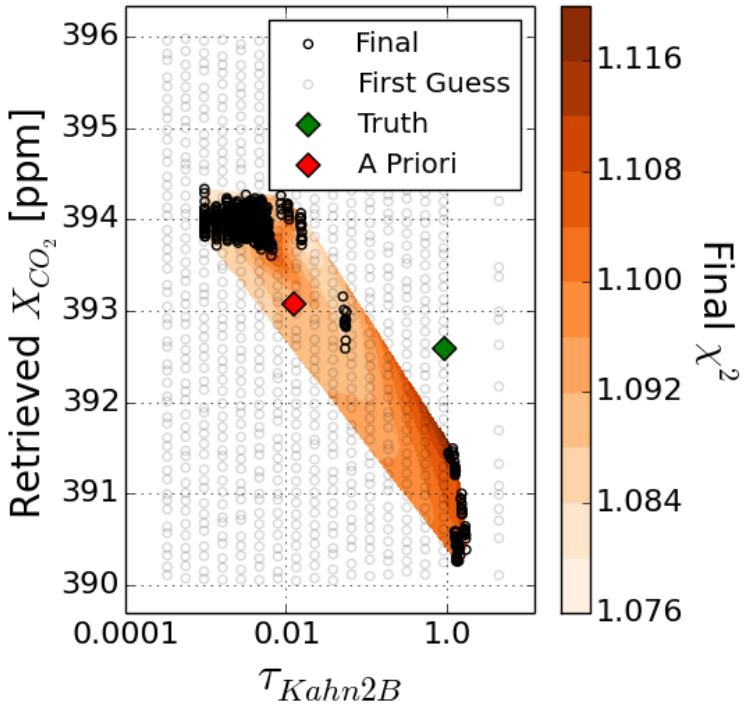

FIGURE 4.6. The χ^2 of the final state of the forward model are shown in orange shading. The final values of X_{CO_2} and Kahn 2b optical depth are shown in black and their corresponding first guesses are shown in light grey. The prior Kahn 2b value and prior X_{CO_2} is shown by the red diamond. The true Kahn 2b optical depth and corresponding true X_{CO_2} is shown by the green diamond.

As suggested by the eight aerosol parameter first guess perturbations of section 4.1, multiple minima and broad valleys of low χ^2 values appear to be present. Despite only perturbing the first guess of two parameters, multiple distinct solutions are present. Overlaying χ^2 reveals the final X_{CO_2} values and their corresponding Kahn 2b optical depths often, but not always, are located in regions of lower χ^2 values. However, because the retrieval state vectors contain 45 elements, it's difficult to attribute these features to local minima in a 2-dimensional χ^2 plot of just two of the state vector elements.

In this chapter I have shown that the OCO-2 ACOS X_{CO_2} retrieval algorithm is highly sensitive to the first guess of aerosol parameters. Perturbing the first guess of aerosol heights and amounts often resulted in unacceptably high variations in the retrieved X_{CO_2}. This implies that the algorithm's forward model contains nonlinearity and that more information is needed to constrain the solution. Additional measurements from other sensors in the Afternoon Train, or "A-Train", or more robust prior information may be useful in the future to help solve this problem. Further examination is needed to determine if a simpler aerosol parameterization would lead to improved results or if the decision to retrieve aerosol amounts in log-space has a non-trivial impact on the retrieved values.

CHAPTER 5

Discussion and Conclusions

This study investigated the impact of aerosols on retrievals of X_{CO_2}. Initially, non-scattering "clear sky" X_{CO_2} retrievals were compared to full physics X_{CO_2} retrievals which include scattering and absorption by clouds and aerosol. The analysis of simulated OCO-2 data and real GOSAT data over ocean and land surfaces led to somewhat contradictory results. With the use of the genetic algorithm and bias corrections when necessary, clear sky X_{CO_2} retrievals from simulated OCO-2 data are comparable to full physics retrievals over ocean but less so over land while clear sky X_{CO_2} retrievals from real GOSAT data are comparable to full physics retrievals over land but substantially less so over ocean. Because of this it can be concluded that the clear sky X_{CO_2} retrieval algorithm is generally inferior to the full physics X_{CO_2} retrieval algorithm, except for at high levels of filtering. This filtering removes low quality retrievals, which typically include scenes contaminated by clouds and aerosols.

The use of a genetic algorithm showed that certain filters independent of the full physics retrieval have the potential to be effectively used in pre-filtering the data. This could be useful for real OCO-2 data because the L2 code is computationally expensive and additional pre-filtering could allow for more "good" data to be fully processed. Additionally, the clear sky retrievals still typically have relatively low errors ($\lesssim 2$ ppm), even if the errors are larger than those of the full physics retrievals. Thus, the clear sky algorithm may be useful for applications requiring a large number of retrievals and with more relaxed error requirements.

The study of clear sky spectral residuals revealed that they are larger than full physics residuals and that they contain a specific pattern related to unmodeled scattering by clouds

and aerosols. However, reducing these residuals by allowing the algorithm to fit for a mean clear sky residual pattern did little to reduce the X_{CO_2} errors and biases. This suggests that the differences between the clear sky and full physics X_{CO_2} retrievals are not simply a function of the residual magnitudes. Very clear scenes were also investigated and it was found that even thin clouds and aerosol layers can cause small but detectable residual patterns in the clear sky retrievals.

Regarding measuring cloud and aerosol properties, it was found that the ACOS X_{CO_2} retrieval algorithm is generally unable to accurately retrieve information about the amount of cloud and aerosol present and only somewhat able to measure the height of cloud and aerosol layers. Retrieving information about individual aerosol types showed even less correlation with true values.

The first guess of various aerosol parameters was shown to significantly affect the retrieved values of the aerosol parameters and the X_{CO_2}. For OCO-2 simulations, the full physics retrieval algorithm often found multiple valid minimizations of the cost function, which indicates nonlinearity in the retrieval algorithm. This presents an opportunity to potentially reduce both the aerosol and X_{CO_2} errors by improving the *a priori* assumptions, modifying the aerosol scheme, or incorporating new data sources into the retrievals.

Overall, this work results in two final conclusions. The first, that clear sky X_{CO_2} retrievals are generally unable to perform as well as full physics X_{CO_2} retrievals, except for when low quality retrievals are removed by high levels of filtering. The second, that the aerosol parameterization in the full physics X_{CO_2} retrieval algorithm results in unacceptable levels of nonlinearity. Both of these conclusions motivate additional study of different methods to handle scattering and absorption by clouds and aerosols in the ACOS X_{CO_2} retrieval algorithm.

Future work includes looking at real data from the OCO-2 satellite, which was successfully launched in July of 2014. This will allow the comparison of simulated clear sky retrievals to real retrievals along with the ability to compare real OCO-2 data to real GOSAT data and hopefully resolve discrepancies relating to clear sky retrieval effectiveness over land compared to ocean surfaces. Regarding aerosol parameterization, the placement of OCO-2 in the A-train will allow the potentially incorporation of aerosol information from other instruments including CALIOP, the Moderate-resolution Imaging Spectroradiometer (MODIS), and CloudSat. Members of our research group, including myself, have recently submitted a proposal to create a retrieval algorithm that uses both OCO-2 and MODIS measurements to try and better constrain aerosols when retrieving X_{CO_2}. Investigating other aerosols schemes with varying levels of complexity or modifying the aerosol *a priori* assumptions could also lead to improvements in the ACOS X_{CO_2} retrieval algorithm.

References

Aben, I., Hasekamp, O., and Hartmann, W.: Uncertainties in the space-based measurements of CO_2 columns due to scattering in the Earth's atmosphere, Journal of Quantiterative Spectroscopy & Radiative Transfer, 104, 450–459, 2007.

Baker, D. F., Bösch, H., Doney, S. C., O'Brien, D., and Schimel, D. S.: Carbon source/sink information provided by column CO_2 measurements from the Orbiting Carbon Observatory, Atmospheric Chemistry and Physics, 10, 4145–4165, doi:10.5194/acp-10-4145-2010, 2010.

Basu, S., Guerlet, S., Butz, A., Houweling, S., Hasekamp, O., Aben, I., Krummel, P., Steele, P., Langenfelds, R., Torn, M., Biraud, S., Stephens, B., Andrews, A., and Worthy, D.: Global CO_2 fluxes estimated from GOSAT retrievals of total column CO_2, Atmospheric Chemistry and Physics, 13, 8695–8717, 2013.

Baum, B. A., Heymsfield, A. J., Yang, P., and Bedka, S. T.: Bulk scattering properties for the remote sensing of ice clouds, Part I: microphysical data and models, Journal of Applied Meteorology, 44, 1885–1895, 2005a.

Baum, B. A., Yang, P., Heymsfield, A. J., Platnick, S., King, M. D., Hu, Y.-X., and Bedka, S. T.: Bulk scattering properties for the remote sensing of ice clouds, Part II: narrowband models, Journal of Applied Meteorology, 44, 1896–1911, 2005b.

Butz, A., Hasekamp, O. P., Frankenberg, C., and Aben, I.: Retrievals of atmospheric CO_2 from simulated space-borne measurements of backscattered near-infrared sunlight: accounting for aerosol effects, Applied Optics, 48, 3322–3336, doi:10.1364/AO.48.003322, 2009.

Butz, A., Guerlet, S., Hasekamp, O. P., Kuze, A., and Suto, H.: Using ocean-glint scattered sunlight as a diagnostic tool for satellite remote sensing of greenhouse gases, Atmospheric Measurement Techniques, 6, 2509–2520, doi:10.5194/amt-6-2509-2013, 2013.

Chevallier, F., Bréon, F.-M., and Rayner, P. J.: Contribution of the Orbiting Carbon Observatory to the estimation of CO_2 sources and sinks: Theoretical study in a variational data assimilation framework, Journal of Geophysical Research, 112, D09 307, doi: 10.1029/2006JD007375, 2007.

Chevallier, F., Maksyutov, S., Bousquet, P., Bréon, F.-M., Saito, R., Toshida, Y., and Yokota, T.: On the accuracy of the CO_2 surface fluxes to be estimated from the GOSAT observations, Geophysical Research Letters, 36, L19 807, doi:10.1029/2009GL040108, 2009.

Chin, M., Ginoux, P., Kinne, S., Torres, O., Holben, B. N., Duncan, B. N., Martin, R. V., Logan, J. A., Higurashi, A., and Nakajima, T.: Tropospheric aerosol optical thickness from the GOCART model and comparisons with satellite and Sun photometer measurements. Journal of the atmospheric sciences, Journal of the Atmospheric Sciences, 59, 461–483, 2002.

Colarco, P., Silva, A., Chin, M., and Diehl, T.: Online simulations of global aerosol distributions in the NASA GEOS-4 model and comparisons to satellite and ground-based aerosol optical depth, Journal of Geophysical Research, 115, D14 207, doi:10.1029/2009JD012820, 2010.

Connor, B. J., Bösch, H., Toon, G., Sen, B., Miller, C., D., and Crisp: Orbiting Carbon Observatory: Inverse method and prospective error analysis, Journal of Geophysical Research, 113, D05 305, doi:10.1029/2006JD008336, 2008.

Crisp, D., Atlas, R. M., Bréon, F.-M., Brown, L. R., Burrows, J. P., Ciais, P., Connor, B. J., Doney, S. C., Fung, I. Y., Jacob, D. J., Miller, C. E., O'Brien, D., Pawson, S.,

Randerson, J. T., Rayner, P., Salawitch, R. J., Sander, S. P., Sen, B., Stephens, G. L., Tans, P. P., Toon, G. C., Wennberg, P. O., Wofsy, S. C., Yung, Y. L., Kuang, Z., Chudasama, B., Sprague, G., Weiss, B., Pollock, R., Kenyon, D., and Schroll, S.: The Orbiting Carbon Observatory (OCO) mission, Advances in Space Research, 34, 700–709, doi:10.1016/j.asr.2003.08.062, 2004.

Crisp, D., Bösch, H., Brown, L., Castano, R., Christi, M., Connor, B., Frankenberg, C., McDuffie, J., Miller, C. E., Natraj, V., O'Dell, C., O'Brien, D., Polonsky, I., Oyafuso, F., Thompson, D., Toon, G., and Spurr, R.: OCO (Orbiting Carbon Observatory)-2 Level 2 Full Physics Retrieval Algorithm Theoretical Basis, Tech. Rep. OCO D-65488, Tech. rep., NASA Jet Propulsion Laboratory, California Institute of Technology, Pasadena, CA, version 1.0 Rev 4, http://disc.sci.gsfc.nasa.gov/acdisc/ documentation/OCO-2 L2 FP ATBD v1 rev4 Nov10.pdf, (last access: January 2012), 2010.

Frankenberg, C., Platt, U., and Wagner, T.: Iterative maximum a posteriori (IMAP)-DOAS for retrieval of strongly absorbing trace gases: Model studies for CH_4 and CO_2 retrieval from near infrared spectra of SCIAMACHY onboard ENVISAT, Atmospheric Chemistry and Physics, 5, 9–22, 2005.

Frankenberg, C., Hasekamp, O., O'Dell, C., Sanghavi, S., Butz, A., and Worden, J.: Aerosol information content analysis of multi-angle high spectral resolution measurements and its benefit for high accuracy greenhouse gas retrievals, Atmospheric Measurement Techniques, 5, 1809–1821, doi:10.5194/amt-5-1809-2012, 2012.

Frankenberg, C., , O'Dell, C., Berry, J., Guanter, L., Joiner, J., Köhler, P., Pollock, R., and Taylor, T. E.: Prospects for chlorophyll fluorescence remote sensing from the Orbiting Carbon Observatory-2, Remote Sensing of Enviornment, 147, 1–12, doi: 10.1016/j.rse.2014.02.007, 2013.

Hansen, J. E. and Travis, L. D.: Light scattering in planetary atmospheres, Space Science Review, 16, 527–610, doi:10.1007/BF00168069, 1974.

Holben, B. N., Eck, T. F., Slutsker, I., Tanré, D., Buis, J., Setzer, A., Vermote, E., Reagan, J. A., Kaufman, Y. J., Nakajima, T., Lavenu, F., Jankowiak, I., and Smirnov, A.: AERONET - A Federated Instrument Network and Data Archive for Aerosol Characterization, Remote Sensing of Environment, 66, 1–16, doi:10.1016/S0034-4257(98)00031-5, 1998.

Kahn, R., Banerjee, P., and McDonald, D.: Sensitivity of multiangle imaging to natural mixtures of aerosols over ocean, Journal of Geophysical Research, 106, 18 219–18 238, 2001.

Le Quéré, C., Raupach, M. R., Canadell, J. G., and Marland, G.: Trends in the sources and sinks of carbon dioxide, Nature Geoscience, 2, 831–836, doi:10.1038/ngeo689, 2009.

Mandrake, L., Frankenberg, C., O'Dell, C. W., Osterman, G., Wennberg, P., and Wunch, D.: Semi-autonomous sounding selection for OCO-2, Atmospheric Measurement Techniques, 6, 2851–2864, doi:10.5194/amt-6-2851-2013, 2013.

Miller, C. E., Crisp, D., DeCola, P. L., Olsen, S. C., Randerson, J. T., Michalak, A. M., Alkhaled, A., Rayner, P., Jacob, D. J., Suntharalingam, P., Jones, D. B. A., Denning, A. S., Nicholls, M. E., Doney, S. C., Pawson, S., Böosch, H., Connor, B. J., Fung, I. Y., O'Brien, D., Salawitch, R. J., Sander, S. P., Sen, B., Tans, P., Toon, G. C., Wennberg, P. O., Wofsy, S. C., Yung, Y. L., and Law, R. M.: Precision requirements for space-based X_{CO_2} data, Journal of Geophysical Research, 112, D10 314, doi:10.1029/2006JD007659, 2007.

O'Brien, D. M. and Rayner, P. J.: Global observations of the carbon budget 2. CO_2 column from differential absorption of reflected sunlight in the 1.61 μm band of CO_2, Journal of Geophysical Research, 107, ACH 6–1, 2002.

O'Brien, D. M., Polonsky, I., O'Dell, C., and Carheden, A.: Orbiting Carbon Observatory (OCO), algorithm theoretical basis doc- ument: The OCO simulator ISSN 0737-5352-85, Tech. rep., Cooperative Institute for Research in the Atmosphere, Colorado State University, 2009.

O'Dell, C. W.: Acceleration of multiple-scattering, hyperspectral radiative transfer calculations via low-streams interpolation, Journal of Geophysical Research, 115, D10 206, doi: 10.1029/2009JD012803, 2010.

O'Dell, C. W., Conner, B., Boösch, H., O'Brien, D., Frankenberg, C., Castano, R., Christi, M., Eldering, D., Fisher, B., Gunson, M., McDuffie, J., Miller, C. E., Natraj, V., Oyafuso, F., Polonsky, I., Smyth, M., Taylor, T., Toon, G. C., Wennberg, P. O., and Wunch, D.: The ACOS CO_2 retrieval algorithm - Part 1: Description and validation against synthetic observations, Atmospheric Measurement Techniques, 5, 99–121, 2012.

Periaux, J. and Galan, M.: Genetic Algorithms in Engineering and Computer Science, John Wiley & Son Ltd, 1995.

Rayner, P. J. and O'Brien, D. M.: The utility of remotely sensed CO_2 concentration data in surface source inversions, Geophysical Research Letters, 28, 175–178, doi: 10.1029/2000GL011912, 2001.

Rodgers, C. D.: Inverse Methods for Atmospheric Sounding: Theory and Practice, World Scientific, Singapore, 2000.

Taylor, T. E., O'Dell, C. W., O'Brien, D. M., Kikuchi, N., Nakajima, T. Y. T. Y., Ishida, H., Crisp, D., T., and Nakajima: Comparison of Cloud-Screening Methods Applied to

GOSAT Near-Infrared Spectra, IEEE Transactions on Geoscience and Remote Sensing, 50, 295–309, doi:10.1109/TGRS.2011.2160270, 2012.

Wunch, D., Toon, G. C., Blavier, J. F., Washenfelder, R. A., Notholt, J., Connor, B. J., Griffith, D. W. T., Sherlock, V., and Wennberg, P. O.: The Total Carbon Column Observing Network, Philosophical Transactions of the Royal Society A, 369, 2087–2112, doi:10.1098/rsta.2010.0240, 2011a.

Wunch, D., Wennberg, P. O., Toon, G. C., Connor, B. J., Fisher, B., Osterman, G. B., Frankenberg, C., Mandrake, L., O'Dell, C., Ahonen, P., Biraud, S. C., Castano, R., Cressie, N., Crisp, D., Deutscher, N. M., Eldering, A., Fisher, M. L., Griffith, D. W. T., Gunson, M., Heikkinen, P., Keppel-Aleks, G., Kyrö, E., Lindenmaier, R., Macatangay, R., Mendonca, J., Messerschmidt, J., Miller, C. E., Morino, I., Notholt, J., Oyafuso, F. A., Rettinger, M., Robinson, J., Roehl, C. M., Salawitch, R. J., Sherlock, V., Strong, K., Sussmann, R., Tanaka, T., Thompson, D. R., Uchino, O., Warneke, T., and Wofsy, S. C.: A method for evaluating bias in global measurements of CO_2 total columns from space, Atmospheric Chemistry and Physics, 11, 12 317–12 337, doi:10.5194/acp-11-12317-2011, 2011b.

Yokota, T., Yoshida, Y., Eguchi, N., Ota, Y., Tanaka, T., Watanabe, H., and Maksyutov, S.: Global Concentrations of CO_2 and CH_4 Retrieved from GOSAT: First Preliminary Results, Scientific Online Letters on the Atmosphere, 5, 160–163, doi:10.2151/sola.2009-041, 2009.